Dissertation

Universität Bremen
Fachbereich für Physik und Elektrotechnik
Institut für Umweltphysik

Ground-based remote sensing of carbon dioxide and methane in the Arctic using Fourier-transform infrared spectrometry

---

Zur Erlangung des akademischen Grades
Doktor der Naturwissenschaften (Dr. rer. nat.)

vorgelegt von

Dipl. Phys. Matthias Buschmann

1. Gutachter: Prof. Dr. Justus Notholt
2. Gutachter: Prof. Dr. John P. Burrows

Datum des Kolloquiums: 18.12.2017

Abstract

The research on the global carbon cycle is of great importance in the context of a changing climate. The abundances of the atmospheric greenhouse gases carbon dioxide (CO_2) and methane (CH_4) are monitored across the globe by a network of ground-based solar absorption Fourier-transform infrared spectrometers, the Total Carbon Column Observing Network (TCCON). The goal of this dissertation is to extend the existing measurement time series of both CO_2 and CH_4 taken at the TCCON site in Ny-Ålesund, Spitsbergen. Two possible augmentations have been implemented: the extension to include measurements during the polar night and the usage of middle-infrared (MIR) spectra.

In addition to the near-infrared TCCON measurements, spectra in the middle-infrared are routinely taken in Ny-Ålesund. A series of spectral microwindows were targeted and used for the retrieval of the dry-air mole fractions of CO_2 and CH_4. The obtained data are compared to the standard TCCON retrieval. The different altitude sensitivity of the MIR retrieval reveals a strong influence of the a priori information chosen for the retrieval process. As a result the newly created CO_2 and CH_4 products provide only a limited amount of additional information.

In the high Arctic, measurements of solar absorption spectra are not possible in winter, because the Sun is permanently below the horizon. A new thermo-electrically cooled InGaAs detector for measurements in the near-infrared is introduced. Its higher sensitivity under low light conditions allows to use moonlight as a light source for atmospheric absorption measurements. The new detector was installed in Ny-Ålesund after first proof-of-concept measurements in Bremen. The measurement parameters have been optimized and spectra were recorded between 2012 and 2016 to retrieve the column averaged dry-air mole fractions of CO_2 and CH_4. The lunar measurements were validated by solar absorption retrievals and compared to results from various reanalysis model simulations as well as in-situ measurements.

Publications and conference contributions

Peer-reviewed articles

Buschmann et al. [2015]: **M. Buschmann**, N.M. Deutscher, M. Palm, T. Warneke, C. Weinzierl, and J. Notholt; *The arctic seasonal cycle of total column CO_2 and CH_4 from ground-based solar and lunar FTIR absorption spectrometry*; Springer Earth System Sciences, pages 85–90. Springer International Publishing, 2015. ISBN 978-3-319-13864-0. doi:10.1007/978-3-319-13865-7_10.

Buschmann et al. [2016]: **M. Buschmann**, N. M. Deutscher, V. Sherlock, M. Palm, T. Warneke, and J. Notholt.; *Retrieval of xCO_2 from ground-based mid-infrared (NDACC) solar absorption spectra and comparison to TCCON*; Atmospheric Measurement Techniques, 9(2):577–585, 2016. doi:10.5194/amt-9-577-2016.

Buschmann et al. [2017a]: **M. Buschmann**, N. M. Deutscher, M. Palm, T. Warneke, C. Weinzierl, and J. Notholt; *The arctic seasonal cycle of total column CO_2 and CH_4 from ground-based solar and lunar FTIR absorption spectrometry*; Atmospheric Measurement Techniques, 10(7):2397–2411, 2017. doi: 10.5194/amt-10-2397-2017.

Meggers et al. [2015]: H. Meggers, **M. Buschmann**, K. Grosfeld, and S. Klebe; *The Educational Program of the Earth System Science Research School (ESSReS)*; Springer Earth System Sciences, pages 9–17. Springer International Publishing, 2015. ISBN 978-3-319-13864-0. doi: 10.1007/978-3-319-13865-7_2

Thorne et al. [2017]: P. W. Thorne, F. Madonna, J. Schulz, T. Oakley, B. Ingleby, M. Rosoldi, E. Tramutola, A. Arola, **M. Buschmann**, A. C. Mikalsen, R. Davy, C. Voces, K. Kreher, M. De Maziere, and G. Pappalardo; Making better sense of the mosaic of environmental measurement networks: a system-of-systems approach and quantitative assessment. Geoscientific Instrumentation, Methods and Data Systems, 6(2):453–472, 2017. doi: 10.5194/gi-6-453-2017.

Data publications

Buschmann et al. [2017b]: **M. Buschmann**, N.M. Deutscher, M. Palm, T. Warneke, C. Weinzierl, and J. Notholt; *Column averaged dry-air mole fractions of CO_2 and CH_4 at Ny-Ålesund from 2012 to 2016*; Pangaea Database; 2017; `https://doi.org/10.1594/PANGAEA.872007`

Notholt et al. [2017a]: J. Notholt, C. Petri, T. Warneke, N. Deutscher, **M. Buschmann**, C. Weinzierl, R. Macatangay, P. Grupe; *TCCON data from Bremen, Germany, Release GGG2014R0*; TCCON data archive; 2017; `https://doi.org/10.14291/tccon.ggg2014.bremen01.R0/1149275`

Notholt et al. [2017b]: J. Notholt, O. Schrems, T. Warneke, N. Deutscher, C. Weinzierl, M. Palm, **M. Buschmann**, AWIPEV Station Engineers; *TCCON data from Ny-Ålesund, Spitzbergen, Norway, Release GGG2014R0*; TCCON data archive; 2017; `https://doi.org/10.14291/tccon.ggg2014.nyalesund01.R0/1149278`

Talks

M.Buschmann, S.Dohe, E.Mahieu, N.M.Deutscher, T.Warneke, J.Notholt; *Advances in CO2 total column retrieval by mid-IR Fourier-Transform Spectroscopy*; 2012-03-29; DPG Frühjahrstagung 2012, Berlin (D)

M.Buschmann, N.M.Deutscher, M.Palm, T.Warneke, T.Weinzierl, J.Notholt; *First results from NIR lunar total column xCO2 FTIR spectroscopy*; 2013-02-27; DPG Frühjahrstagung 2013, Jena (D)

M.Buschmann, N.M.Deutscher, M.Palm, T.Warneke, C.Weinzierl, J.Notholt; *The seasonal cycle of total column CO2 and CH4 in the high arctic*; 2014-03-19; DPG Frühjahrstagung 2014, Berlin (D)

M.Buschmann, N.M.Deutscher, M.Palm, T.Warneke, C.Weinzierl, J.Notholt; *FTIR retrieval of the arctic total column full seasonal cycle of CO2 and CH4*; 2014-05-02; EGU 2014 Vienna (A)

M.Buschmann, N.M.Deutscher, M.Palm, T.Warneke, C.Weinzierl, J.Notholt; *Seasonal cycles of xCO2 and xCH4 from Ny-Ålesund*; 2014-05-15; TCCON/NDACC-IRWG 2014 Meeting, Bad Sulza (D)

Posters

M.Buschmann, S.Dohe, E.Mahieu, N.Deutscher, T.Warneke, J.Notholt; *CO2 total column retrieval by mid-IR FT Spectroscopy*; 2012-04-24; EGU 2012 Vienna (A)

M.Buschmann, S.Dohe, E.Mahieu, N.Deutscher, T.Warneke, J.Notholt; *Mid-IR retrieval of xCO2 from NDACC/TCCON station Ny Ålesund*; 2012-06; NDACC IRWG / TCCON meeting 2012, Wengen (CH)

M.Buschmann, N.Deutscher, S.Dohe, V.Sherlock, D.Griffith, and J.Notholt; *Comparison of middle and near infrared total column xCO2 retrieval*; 2013-02-26; DPG Frühjahrstagung 2013, Jena (D)

M.Buschmann, N.Deutscher, M. Palm, T. Warneke, C.Weinzierl, J.Notholt *Extending Arctic CO2 column measurements to cover the complete seasonal cycle using lunar FTIR spectroscopy during Polar Night*; 2013-06-04; 9th International Carbon Dioxide Conference, Beijing (CN)

M.Buschmann, N.Deutscher, V.Sherlock, S.Dohe, J.Robinson, D.Smale, M.Schneider, F.Hase, N.Jones, D.Griffith, J.Notholt; *Comparison of MIR and NIR xCO2 Retrievals for Validation of Greenhouse Gas Satellite Measurements*; ESA Living Planet Symposium 2013, Edinburgh (UK)

M.Buschmann, N.M.Deutscher, M.Palm, T.Warneke, C.Weinzierl, J.Notholt; *Towards a full seasonal cycle of total column CO2 and CH4 in the high Arctic*; 2014-07-15; CANDAC Summerschool 2014, Toronto (CA)

M.Buschmann, N.M.Deutscher, M.Palm, T.Warneke, C.Weinzierl, J.Notholt; *The total carbon column seasonal cycle in high latitudes*; 2014-11-21; Earth System Science Research School Annual Retreat, Bremen (D)

Table of contents

Titlepage i
Abstract iii
Publications v
Table of contents ix
List of Figures xi
List of Tables xiii

1 Introduction & Motivation **1**
1.1 Motivation 2
1.1.1 Climate and greenhouse effect 2
1.1.2 Atmospheric Carbon Dioxide 3
1.1.3 Atmospheric Methane 5
1.1.4 Measurement of atmospheric CO_2 and CH_4 8
1.1.5 Ground-based remote sensing measurements in the Arctic 9
1.2 The Ny-Ålesund site 9

2 Fundamentals **13**
2.1 Spectroscopy in the infrared 13
2.1.1 Molecular Transitions 13
2.1.2 Spectral Line Shape 15
2.1.3 Atmospheric Absorption 18
2.2 Fourier Transform Infrared Spectrometry 18
2.2.1 Spectrometry 18
2.2.2 Michelson Interferometry 19
2.2.3 Fourier Transform 19
2.3 Trace gas retrieval 21
2.3.1 Retrieval Principle 21
2.3.2 Spectroscopic Linelist 22
2.3.3 Atmospheric Model 22
2.3.4 A Priori Profiles 22
2.3.5 Averaging Kernels 23
2.3.6 Comparing Datasets 23
2.3.7 Calculation Of Dry-Air Mole Fractions 24
2.3.8 Postprocessing 24

3 Middle-infrared trace gas retrieval **25**
3.1 Micro window selection . . . 27
3.2 MIR xCO_2 retrieval . . . 28
3.3 A priori influence . . . 30
3.4 Averaging kernel influence . . . 37
3.5 Lunar MIR xCH_4 retrieval . . . 38
3.6 Conclusion . . . 40

4 Extension of the CO_2 and CH_4 time series to the polar night **43**
4.1 Lunar irradiance . . . 44
4.2 The thermo-electrically cooled InGaAs detector . . . 46
4.3 Proof of concept and first light of the new detector in Bremen . . . 49
4.4 Optimisation of measurement parameters and retrieval method . . . 51
4.4.1 The effect of spectral resolution and noise on the retrieval . . . 51
4.4.2 Airmass factor . . . 56
4.4.3 The influence of backscattered sunlight . . . 58
4.4.4 Adjustment of the atmospheric model . . . 60
4.4.5 Solar lines . . . 61
4.4.6 Filter conditions for lunar spectra . . . 63
4.5 Validation by solar absorption retrieval . . . 66
4.6 Comparison of the new time series to model simulations . . . 69
4.6.1 Averaging kernel smoothing . . . 69
4.6.2 Lunar Averaging Kernels . . . 71
4.6.3 Model comparison – time series . . . 73
4.6.4 Model comparison – seasonal cycle . . . 74
4.7 Comparison to ground-based in-situ measurements . . . 76
4.8 Conclusion . . . 78

5 Summary & Outlook **81**

Acknowledgements **85**

A Appendix **87**
A.1 Estimation of lunar irradiance . . . 87
A.2 Clear sky determination for automated measurements . . . 88
A.3 FTS footprint . . . 89
A.4 Ny-Ålesund surface pressure calibration . . . 92
A.5 Stability of the Ny-Ålesund FTS . . . 93
A.6 Horizon line calculation from Svalbard DEM . . . 94

Bibliography **97**

Glossary **109**

List of Figures

1.1 Components of the global carbon budget . . . 3
1.2 Global carbon dioxide budget . . . 4
1.3 CO_2 cycle from in-situ measurements . . . 5
1.4 CH_4 cycle from in-situ measurements . . . 6
1.5 Arctic carbon pools . . . 7
1.6 Ny-Ålesund site setup . . . 10
1.7 TCCON and NDACC-IRWG stations in the Arctic . . . 10

2.1 Vibrational/rotational molecular transitions . . . 15
2.2 NIR spectral line positions and intensities . . . 16
2.3 FTIR spectrometer measurement diagram . . . 20

3.1 MIR CO_2 microwindow fit results . . . 28
3.2 TCCON CO_2 a priori profiles . . . 30
3.3 Comparison of TCCON xCO_2 retrievals with different a priori profiles . . . 33
3.4 MIR–NIR averaging kernel comparison . . . 34
3.5 Comparison of MIR xCO_2 retrievals with different a priori profiles . . . 35
3.6 Fit of the seasonal cycle to different MIR xCO_2 retrieval runs . . . 36
3.7 Tropospheric and stratospheric contribution to MIR and NIR averaging kernels . . . 36
3.8 Estimation of the averaging kernel smoothing correction . . . 38
3.9 Comparison of Lunar MIR to NIR xCH_4 retrieval . . . 40

4.1 Lunar irradiance estimation . . . 45
4.2 Full moon pictures . . . 46
4.3 Diode comparison . . . 47
4.4 Example spectra from lunar and lamp measurements . . . 48
4.5 Proof-of-concept measurements in Bremen . . . 50
4.6 Impact of reduced spectral resolution on the retrieval . . . 52
4.7 Improvement of the signal-to-noise ratio at lower resolutions . . . 53
4.8 Differences in retrieved CO_2 and CH_4 at lower spectral resolutions . . . 54
4.9 Comparison of measurements with different spectral resolutions . . . 55
4.10 Impact of changing airmass during one measurement . . . 57
4.11 Sun – Moon – observer geometry . . . 58
4.12 Effect of backscattered sunlight on lunar retrieval – Time series . . . 59
4.13 Effect of backscattered sunlight on lunar retrieval – LZA dependence . . . 60

4.14 Atmospheric model adjustment for lunar xCO_2 and xCH_4 retrievals 61
4.15 Atmospheric model adjustment for solar xCO_2 and xCH_4 retrievals 62
4.16 Example retrieved lunar spectrum and fit 63
4.17 Lunar NIR data filter application 64
4.18 Comparison of the solar and lunar measurements of xCO_2 and xCH_4 68
4.19 Comparison of the solar and lunar measurements of xO_2 69
4.20 Averaging kernels of the lunar retrievals 72
4.21 FTS – Model comparison: time series CH_4 73
4.22 FTS – Model comparison: time series CO_2 74
4.23 FTS – Model comparison: seasonal cycle CO_2 75
4.24 FTS – Model comparison: seasonal cycle CH_4 76
4.25 Comparison of solar and lunar absorption measurements to surface flasks . 77

A.1 Determination of polar night clear sky conditions 89
A.2 Ny-Ålesund footprint 91
A.3 Ny-Ålesund surface pressure calibration 93
A.4 Ny-Ålesund instrument stability 94
A.5 Ny-Ålesund terrain and observation capability 95

List of Tables

3.1 Microwindow selection for MIR xCO_2 retrieval 27
3.2 Error estimates for different MIR xCO_2 microwindow retrievals 29
3.3 xCO_2 time series fit parameters 32
3.4 Microwindows used in the lunar MIR xCH_4 retrieval. 39

4.1 InGaAs diode parameters 46
4.2 Bias introduced by lower resolution 53
4.3 Increase in DMF due to solar backscatter 58
4.4 Comparison campaign results for FTS retrievals and model output 67

1. Introduction & Motivation

Earth's atmosphere consists mainly of nitrogen and oxygen. Trace amounts of other gases are also present. Some of these gases are infrared active, meaning they can absorb infrared radiation. Due to their influence on the Earth's radiation budget, these gases are called greenhouse gases. The most prominent ones are water vapour (H_2O), carbon dioxide (CO_2) and methane (CH_4).

Anthropogenic activities have led to an enormous increase in the atmospheric abundance of both CO_2 and CH_4 since the pre-industrial era, predominantly by burning fossil fuels. Both gases are part of turn-over processes in the Earth system. The carbon cycle describes the pathways of carbon between the atmosphere, hydrosphere, biosphere, pedosphere and lithosphere.

The understanding of the carbon cycle and its reaction to anthropogenic influences is the basis for the international efforts to limit carbon emissions to the atmosphere and by doing so, trying to limit the rise of the global mean temperature to well below 2°C compared to pre-industrial levels. This was agreed to in the Paris agreement by the United Nations and entered into force in November 2016 [1]. Leading up to the agreement a series of scientific reports by the Intergovernmental Panel on Climate Change (e.g. Ciais et al. [2013]) repeatedly and increasingly highlighted the need for a reduction of anthropogenic carbon emissions.

Although the main drivers of the carbon cycle are understood, there are still large uncertainties associated with specific sources and sinks of both, CO_2 and CH_4. This is especially true for the Arctic, which is more strongly affected by rise of the global mean temperature due to various feedback mechanisms [McGuire et al., 2009].

In this dissertation ground-based remote sensing measurements are used to retrieve information on the abundances of CO_2 and CH_4 in the Arctic atmosphere. This study aims to extend the already established measurements of the column averaged abundances of these gases taken at Ny-Ålesund, Spitsbergen. The current measurements are performed within the framework of two global observation networks, the Network for the Detection of Atmospheric Composition Change (NDACC) and the Total Carbon Column Observing Network (TCCON) [Wunch et al., 2011a].

[1] http://unfccc.int, accessed 2017-08-28

After a brief motivation and review of the current state on carbon cycle research in this chapter, the physical basics of the measurement process will be discussed in chapter 2. Chapter 3 investigates the possibility to use measurements in the middle-infrared spectral region for the retrieval of information on CO_2 and CH_4. Afterwards in chapter 4, the extension of the Ny-Ålesund time series to include the previously not covered polar night is presented.

1.1. Motivation

1.1.1. Climate and greenhouse effect

Earth's atmosphere is composed of about 78 % nitrogen (N_2), 21 % oxygen (O_2), 1 % argon (Ar) and trace amounts of several other species [Roedel and Wagner, 2011]. The solar radiation differentially deposits energy onto Earths surface and thereby creates global circulation patterns that determine the weather on short time scales. Patterns on longer time scales are referred to as climate.

Among the trace gases in the atmosphere are some that are infrared active, i.e. they absorb and emit radiation in the infrared. Most notably these are water vapour (H_2O), carbon dioxide (CO_2) and methane (CH_4). If no infrared active gases were present in the atmosphere, the solar radiation would heat up Earth's surface and the heated surface would emit radiation according to its temperature. An equilibrium between absorbed and emitted radiation would be established. This equilibrium would lead to a surface temperature of about -15° C. In the presence of greenhouse gases (like H_2O, CO_2 and CH_4) however, solar light with a maximum in the visible spectral region is being transmitted through the atmosphere, again heating up the surface, but the re-emitted radiation with a maximum intensity in the infrared is absorbed in the atmosphere. In part this radiation is then re-emitted towards the surface. This insulating effect is called the greenhouse effect and it leads to the increase of the global mean surface temperature by about 30° C [Roedel and Wagner, 2011] until a new equilibrium between incoming and outgoing radiation is reached.

A change in the atmospheric composition that increases the amount of greenhouse gases therefore generally leads to an increase in surface temperature. Due to the extensive anthropogenic impact on the Earth system, the amounts of CO_2 and CH_4 in the atmosphere are increasing, especially since the beginning of the industrial revolution and the advent of fossil fuel technologies in the 18^{th} century.

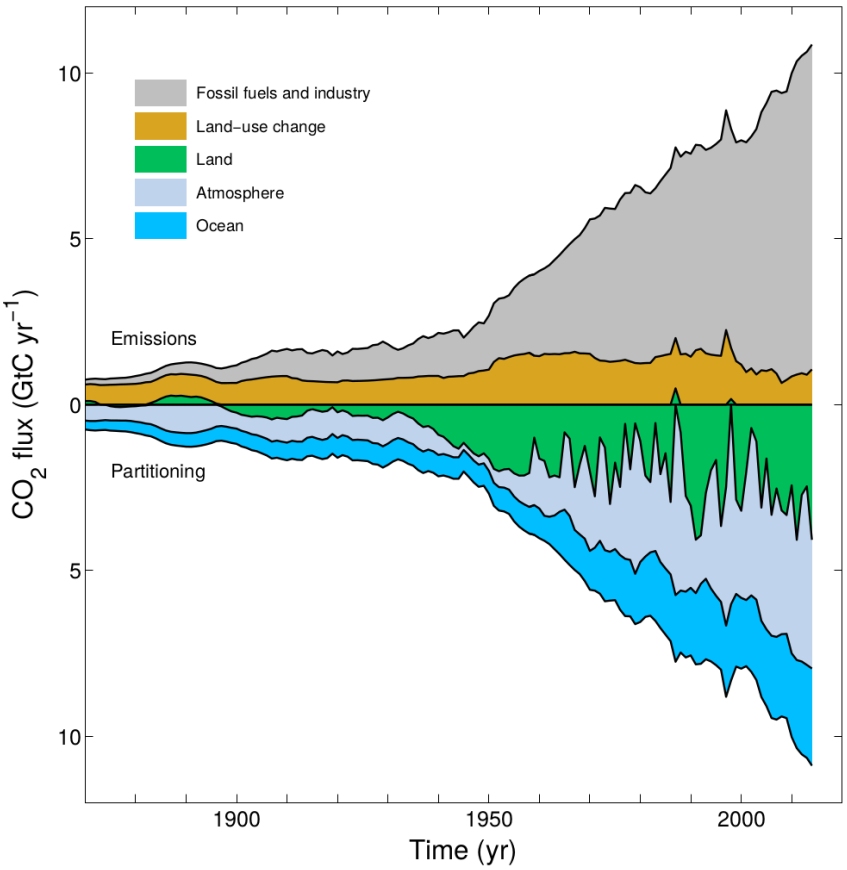

Figure 1.1.: The development of the different components of the global carbon budget from 1870 to 2015. Figure from Le Quéré et al. [2015]

1.1.2. Atmospheric Carbon Dioxide

Extensive reviews of the current state of carbon cycle research are available in the Fifth Assessment Report of the Intergovernmental Panel on Climate Change (IPCC-AR5) [Ciais et al., 2013] and more recently from the Global Carbon Project [Le Quéré et al., 2015]. A review on the importance of the Arctic carbon cycle in face of an accelerated temperature rise in high latitudes compared to the global mean is presented by McGuire et al. [2009]. In the following a brief overview on the global carbon cycle is presented.

The Earth system tends to establish an equilibrium between the emission of CO_2 to the atmosphere and the uptake of CO_2 in the biosphere, lithosphere, pedosphere and hydrosphere. If that equilibrium is disturbed, the system reacts on different time scales to the introduced change, eventually establishing a new equilibrium. For example, exchange processes act on time scales from days (terrestrial biosphere) to hundreds of years for oceanic processes to geological processes that sequester carbon on even longer time scales [Ciais et al., 2013; Le Quéré et al., 2015].

The introduction of massive anthropogenic sources of CO_2 changes this balance compared to pre-industrial times. A time series of sources and sinks of CO_2 reconstructed to the

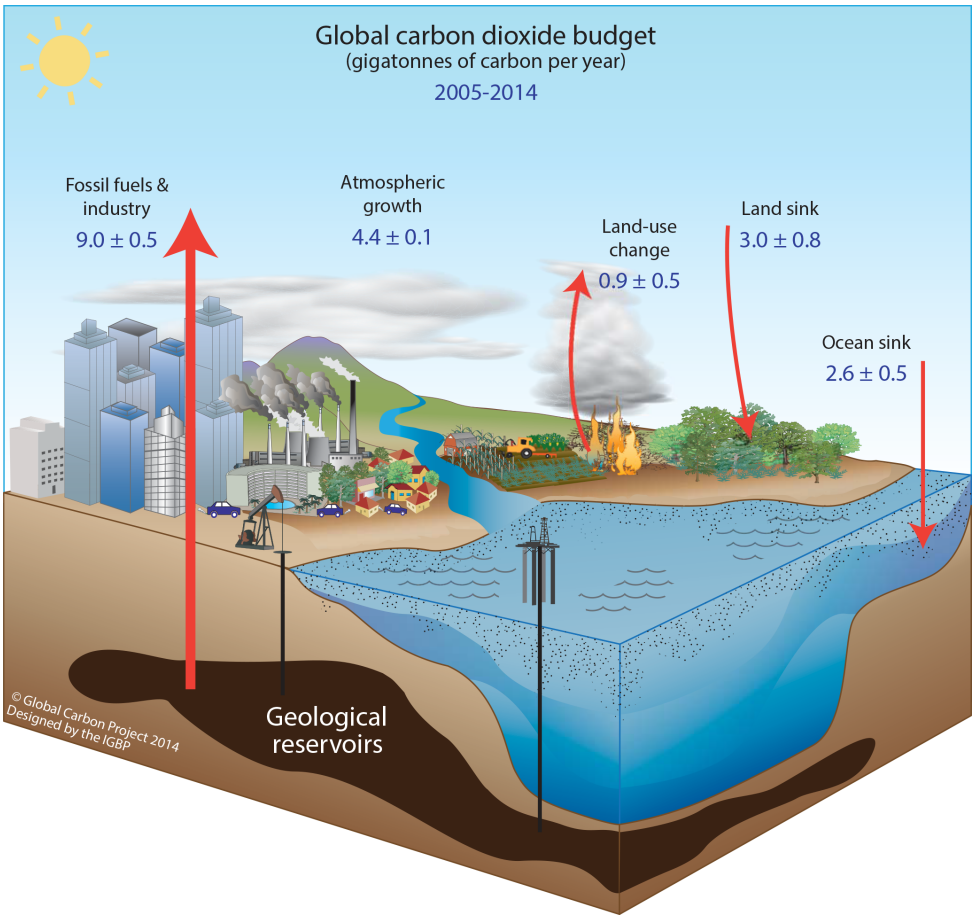

Figure 1.2.: An overview of the components of the global CO_2 budget for 2005–2014. Figure copied from Le Quéré et al. [2015]

1870's is provided by the Global Carbon Project [Le Quéré et al., 2015] and shown in Fig. 1.1. Five different components of the global carbon cycle budget are illustrated. The increase in emissions from fossil fuel burning and industrial emissions, together with the emissions from the change of land-use (e.g. due to agriculture) are labeled 'Emissions'. The current emissions from these two sources alone show an CO_2 flux of more than 10 $GtCyr^{-1}$ [Le Quéré et al., 2015]. To balance the budget, these emissions are partitioned into three components, uptake of CO_2 by the land, the oceans and the atmosphere. The latter is of course of interest in the context of this study. As can be seen in Figures 1.1 and 1.2, currently, in the period 2005–2014, almost half of the emissions of CO_2 remain in the atmosphere.

The left plot in Fig. 1.3 shows the latitudinal distribution of CO_2 as a function of time from 2007–2016. Here zonal averages of ground-based in-situ measurements are averaged over the respective longitudes and interpolated to form a continues surface. The differences between northern and southern hemisphere can clearly be recognized. They originate in the larger land surface on the northern temperate to high latitudes. The strong seasonal amplitude of the CO_2 cycle is produced mainly by the biospheric sea-

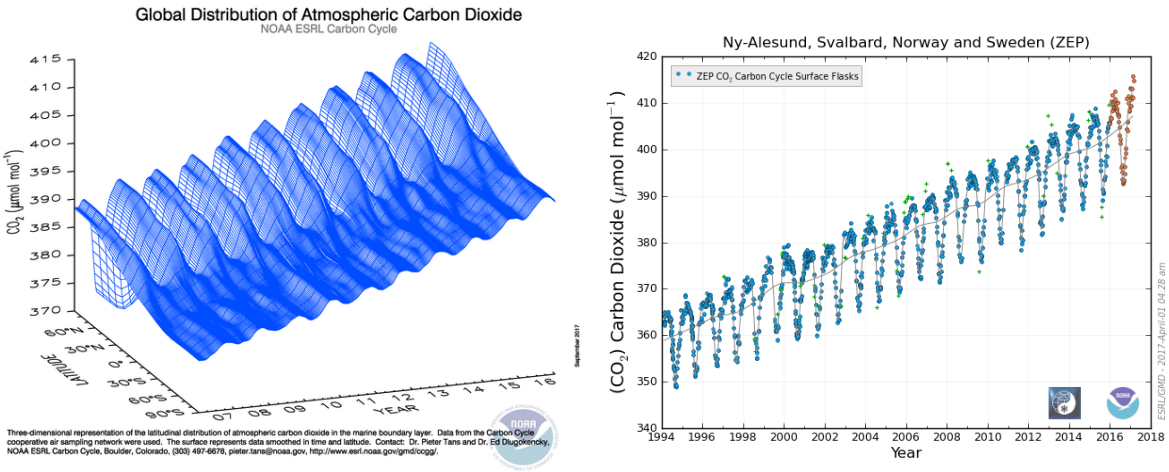

Figure 1.3.: In-situ measurements of CO_2 from the Carbon Cycle cooperative air sampling network. Left: Zonal means as a function of latitude and time. Right: CO_2 measurements from the Zeppelin mountain air sampling station. Both plots from the NOAA webpage[2] [Dlugokencky et al., 2014].

sonal rhythm. In summer plant productivity increases and more CO_2 is taken up by the plants via photosynthesis, while in winter respiration leads to an increase in atmospheric CO_2. In the southern hemisphere the phase shifted, weaker seasonal cycle amplitude is caused by the smaller land mass and consequently lower photosynthetic productivity. In the tropics, signals from both, northern and southern hemisphere can be seen depending on the seasonal shift of the inner tropical convection zone that creates a barrier for inter-hemispheric transport.

The Arctic seasonal cycle of CO_2 in the boundary layer or lower tropospheric is measured at Zeppelin station, which is located on a mountaintop close to Ny-Ålesund. The plot on the left in Fig. 1.3 shows a time series of the Zeppelin mountain in-situ measurements measurements. The seasonal signal with a magnitude of about 20 ppm is expected to be diluted, when measuring the column average with the FTS.

1.1.3. Atmospheric Methane

Similar to the carbon dioxide cycle, several reviews of the current research status on the methane cycle are available. In addition to the extensive review in the latest IPCC Assessment Report [Ciais et al., 2013], Saunois et al. [2016] and Saunois et al. [2017] provide an updated, detailed overview of the global methane cycle from 2000–2012. A comprehensive review on methane with a focus on the Arctic was published recently by

[2] `https://www.esrl.noaa.gov/gmd/ccgg/gallery/figures/co2_surface.png` and `https://www.esrl.noaa.gov/gmd/dv/iadv/`, last accessed 2017-09-21

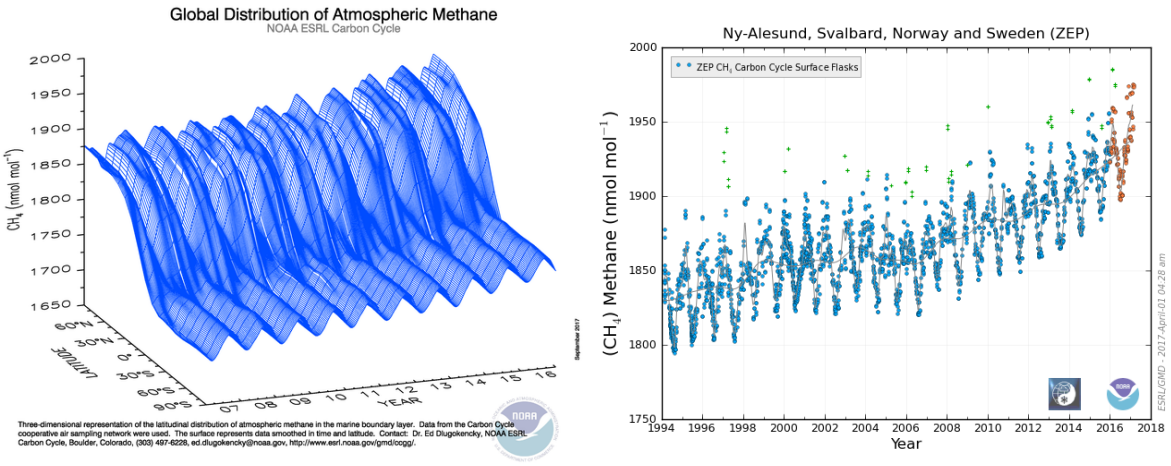

Figure 1.4.: In-situ measurements of CH_4 from the Carbon Cycle cooperative air sampling network. Left: Zonal means as a function of latitude and time. Right: CH_4 measurements from the Zeppelin mountain air sampling station. Both plots from the NOAA webpage[3] [Dlugokencky et al., 2014].

the Arctic Monitoring and Assessment Programme [AMAP, 2015]. Similar to the previous section a brief overview on atmospheric methane is discussed and some specific issues in the Arctic are highlighted.

CH_4 is an chemically active component in the atmosphere unlike CO_2, which can be considered chemically inert. Consequently, methane emitted into the atmosphere has a shorter lifetime than carbon dioxide (up to about 9 years). However, the oxidation of CH_4 creates CO_2 and thus contributes as a source to the CO_2 budget and is a source for stratospheric water vapour and tropospheric ozone [Dlugokencky et al., 2011]. Additionally, CO_2 is relatively well mixed vertically, where as CH_4 shows strong gradients depending on the availability of reaction partners.

The sources of methane are mainly of biogenic, thermogenic or pyrogenic origin. Biogenic production occurs by anaerobic degradation of organic matter. Thermogenic production yields fossil fuels from the transformation of organic matter to geological reservoirs, which can eventually be released to the atmosphere. Combustion of organic matter under low-oxygen conditions leads to pyrogenic emissions, e.g. from biomass burning [Ciais et al., 2013]. Anthropogenic activities are estimated to currently account for 60 % of the global emissions of methane [Saunois et al., 2016].

The most important mechanism of CH_4 destruction is the reaction with atmospheric OH, which removes about 90 % of the emitted CH_4 [Ciais et al., 2013; Saunois et al., 2016]. The stratospheric abundances of OH and chlorine species lead to a methane depletion in the upper atmosphere.

[3] `https://www.esrl.noaa.gov/gmd/ccgg/gallery/figures/ch4_surface.png` and `https://www.esrl.noaa.gov/gmd/dv/iadv/`, last accessed 2017-09-21

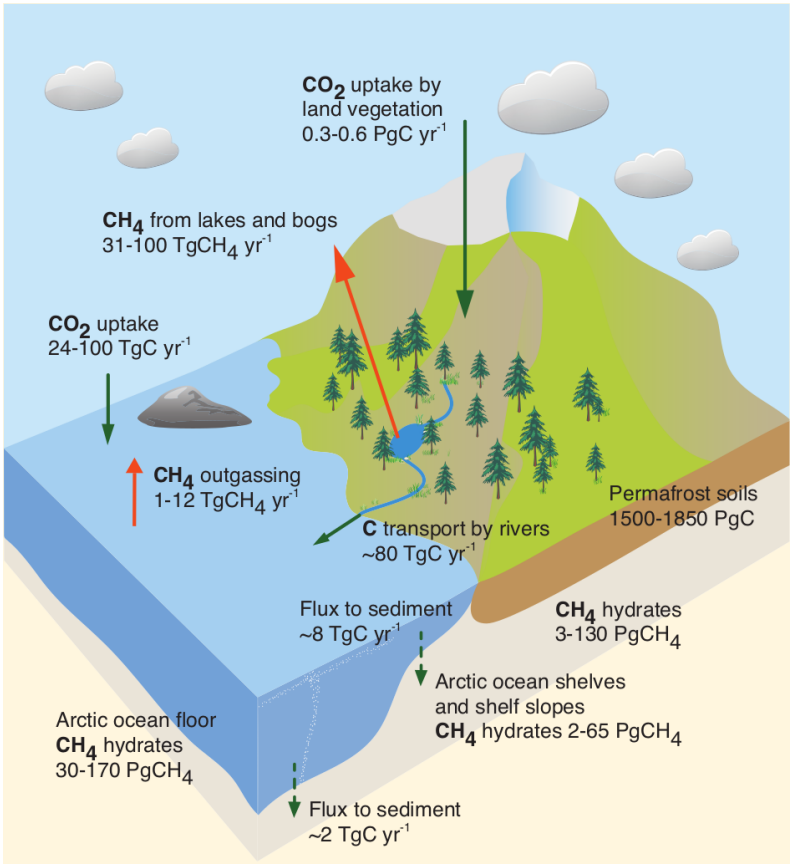

Figure 1.5.: Overview of the carbon pools in the Arctic. Figure copied from Ciais et al. [2013]

Similar to CO_2 the surface in-situ observations of CH_4 are shown in Fig. 1.4. Again, the latitudinal dependence of the zonal mean is shown from 2007–2016, based on a surface air sampling network [Dlugokencky et al., 2014]. The in-situ time series from the Zeppelin observatory in Ny-Ålesund highlights the large seasonal variability at high latitudes. In general, the CH_4 time series shows larger variability in the mid-term range. The causes are still investigated, e.g. the 2007/08 anomaly is assumed to be caused in part by larger than average temperatures in the Arctic [Dlugokencky et al., 2009].

The situation for the Arctic is fundamentally different compared to other regions. Circumpolar permafrost stores large amounts of organic matter. The increased mean surface temperature due to climate change has an impact on the stability of these reservoirs. The magnitude and sources of the potentially massive CH_4 emissions from thawing permafrost soils are still under investigation (see e.g. most recently Kohnert et al. [2017]). The second process unique to the Arctic is sea ice and its impact on ocean – atmosphere gas exchange. A decreasing sea ice cover of the Arctic ocean can change surface ocean circulation patterns leading to increased oceanic emissions (see e.g. Damm et al. [2015]). The third potential additional source in the Arctic refers to emission from de-stabilized methane hydrates that are located in the sea floor of the Arctic continental shelves. Sea floor methane seepages have been observed, but the transport through the water column

to the atmosphere is not yet observed (see e.g. Sahling et al. [2014]). A diagram of the current estimates of the carbon pools in the Arctic, i.e. CO_2 and CH_4, is provided by Ciais et al. [2013] and shown in Fig. 1.5.

1.1.4. Measurement of atmospheric CO_2 and CH_4

In general there are two methods to infer sources and sinks of atmospheric trace gases. The bottom-up approach infers an atmospheric composition from flux estimates and the top-down approach uses atmospheric measurements to infer fluxes. The carbon cycle can be further constrained by their comparison. The measurements can be classified into three categories. In-situ measurements offer high precision, accuracy and continuity, but their spatial distribution is highly limited. An example is the air sampling network used for Fig. 1.3 [Dlugokencky et al., 2014]. Satellites offer high spatial coverage, but poorer precision and limited temporal coverage. Additionally, their measurements need to be validated, which is challenging using in-situ measurements due to different sensitivities of in-situ and remote sensing measurements. Ground-based methods that sample the entire atmosphere, like TCCON measurements, can be comfortably used to validate satellite measurements, as they sample similar quantities. Nonetheless, each method can be used independently to study the carbon cycle.

To ensure traceability to recognized standards, the TCCON measurements have been validated against aircraft profiles that measure the column in-situ to WMO standards [Deutscher et al., 2010; Geibel et al., 2012; Messerschmidt et al., 2011; Wunch et al., 2010]. Then, the TCCON measurements themselves can be used to validate CO_2 and CH_4 retrievals from a number of satellite missions currently or previously in orbit. Extensive research has been performed with measurements from SCIAMACHY on Envisat by ESA [Bovensmann et al., 1999; Burrows et al., 1995], the TANSO-FTS on GOSat by JAXA [Kuze et al., 2009] and the Orbiting Carbon Observatory-2 (OCO-2) by NASA [Crisp et al., 2004]. Measurements from all of these satellites have been validated with TCCON measurements.

There are several reanalysis models available, that assimilate measurements to provide global CO_2 and CH_4 products, e.g. CarbonTracker [Peters et al., 2007], the Jena CO_2 inversion [Rödenbeck, 2005] or the MACC[4] models. Often, a combination of different measurement techniques is used for intercomparison, for example GOSat to TCCON [Wunch et al., 2017b; Yoshida et al., 2013], surface in-situ measurements to TCCON [Chevallier et al., 2011], SCIAMACHY to in-situ surface measurements [Bergamaschi et al., 2013] or combined satellite products to model runs [Kulawik et al., 2016]. Large

[4]Monitoring Atmospheric Composition and Climate (MACC) of the European Copernicus Atmosphere Service `http://www.gmes-atmosphere.eu`, accessed 2017-09-21

intercomparison campaigns like ESA's Greenhouse Gas Climate Change Initiative (GHG-CCI) [Buchwitz et al., 2013] use model, satellite and ground-based input to consolidate the current state of carbon cycle research [Dils et al., 2014].

1.1.5. Ground-based remote sensing measurements in the Arctic

Continuous measurements of total column amounts of various trace gases have been performed at the Ny-Ålesund site since 1992 employing solar absorption spectroscopy [Notholt and Schrems, 1994] within the Network for the Detection of Atmospheric Composition Change (NDACC, formerly NDSC). Of particular interest are the two species carbon dioxide and methane. Both of which have been measured within the scope of the Total Carbon Column Observing Network (TCCON) measurements in the near-infrared in Ny-Ålesund since 2004 [Warneke et al., 2005]. But due to its high latitude solar absorption measurements are not possible during the polar night between October and March, as the Sun is permanently below the horizon. Using the Moon as a substitute light source above the atmosphere, absorption spectroscopy has been performed for various species measured in the NDACC in the mid-infrared spectral region [Notholt et al., 1993].

In order to extend the xCO_2 and xCH_4 time series there are two options available. The first option is to utilise the absorption lines in the mid-infrared using current and historic spectra. This would potentially extend the time series to the start of the mid-infrared measurements in 1992. The second option is to employ the lunar absorption spectroscopy approach to near-infrared TCCON spectral windows. This requires a change in the measurement setup and installation of a new detector to compensate for the loss of signal when using moonlight (compared to sunlight).

1.2. The Ny-Ålesund site

The Ny-Ålesund FTS is hosted by AWIPEV, a joint research station of the Alfred-Wegener-Institut and the Institut Polaire Français Paul-Emile Victor and operated by the Institute of Environmental Physics (IUP), University of Bremen. Ny-Ålesund is a small research village on the island of Spitsbergen, which is part of the Svalbard archipelago. The station is located at 78.92°N, 11.92°E (see Fig. 1.7) at an altitude of 21 m (altitude of the solar tracker) above sea level. Ny-Ålesund is located on the south-west coast of a fjord (Kongsfjorden) on a peninsula (Brøggerhalvøya). The surrounding landscape is characterized by high mountains and glaciers. Just south of the observatory Zeppelin mountain obstructs the view at high solar or lunar zenith angles. An overview of the terrain and the determination of a horizon line is shown in appendix A.6. Logistics in Ny-Ålesund are provided by a dedicated company (Kingsbay AS) and the AWIPEV staff.

Figure 1.6.: Aerial photograph of Ny-Ålesund and interior shot of the FTIR lab in the AWIPEV observatory. The location of the Lab and the entrance of the tracked light are marked with arrows. The old (top) and new (bottom) solar tracker on the roof of the observatory tracking the Moon can be seen on the right.

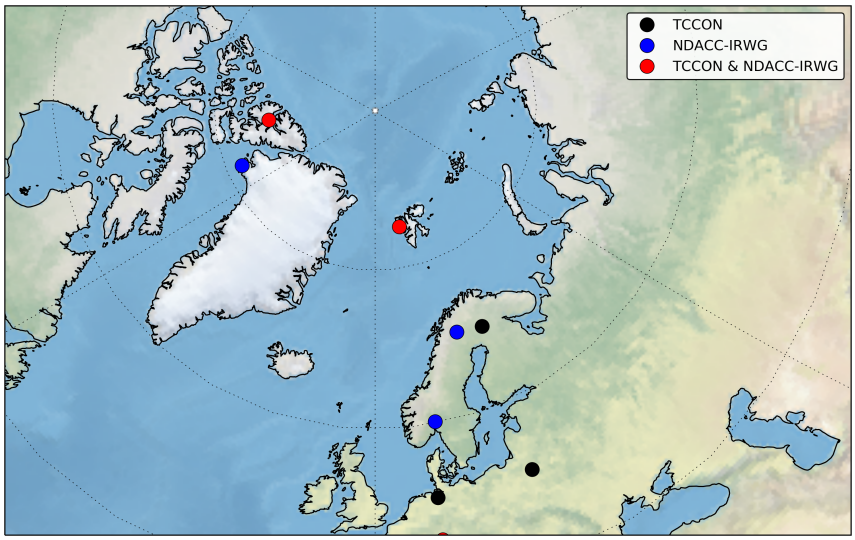

Figure 1.7.: Locations of the NDACC-IRWG and TCCON stations in the North.

The high latitude of Ny-Ålesund leads to polar night conditions in the winter, where the Sun does not rise above the horizon from October 24 to February 18. In contrast, the sun does not set from April 18 to August 24 during polar day[5]. Solar absorption measurements are therefore possible from March to September.

The Ny-Ålesund FTS is a Bruker 120HR that received an electronics and optical components upgrade in 2012. The basic principle of the FTS system is explained in Sec. 2.2. Since 2012 it is designated a Bruker 120-5HR, as it has the same properties as a 125HR instrument. The solar tracker system also received an upgrade recently in 2014. The new tracker system allows for semi-automated measurements and thus increases the amount of measured spectra significantly from 2014 onwards. The measurement schedule is set to take alternating NDACC and TCCON measurements under cloud free conditions in summer and lunar absorption measurements in the MIR and emission measurements in the NIR during Polar Night. Even after the solar tracker update, which allows for software defined automation of different measurements, some manual intervention is required. For some setups, the beamsplitter needs to be changed manually and the detectors for the MIR measurements need to be cooled with liquid nitrogen, that has to be refilled manually. On a routine basis, the on-site AWIPEV engineer operates the instrument, unless the instrument is operated on site by IUP members during maintenance or measurement campaign visits. Changes to the instruments software setup, e.g. changing the instrument parameters, can be performed remotely without on-site support.

[5]Information on the duration of the polar night and the midnight sun can be found on `http://om.yr.no/about/midnight-sun/`, last access 2017-05-15.

2. Fundamentals

In this chapter, the fundamental physics required to understand the trace gas retrieval process are discussed. First the origin of the spectral absorption features are presented. Then, after a quick overview of mechanisms of spectral line broadening, Fourier Transformation and the FTS are discussed. Finally the retrieval approach is presented that retrieves information of the abundances of atmospheric trace gases from the recorded spectra.

2.1. Spectroscopy in the infrared

2.1.1. Molecular Transitions

Molecules can be described as a quantum system. In the ground state, the molecule has the lowest possible energy and when the molecule absorbs energy it transitions into an excited state with higher energy. From the higher energy state the molecule can relax back to its ground state or a state with less energy. For a single molecule, the transitions have a discrete amount of energy associated with them and the exchange, in the case of absorption and emission, is facilitated by the quantum of the electromagnetic field: the photon. The frequency of the absorbed or emitted photon is proportional to the energy difference between the excited and relaxed state.

The possible transitions for a given molecular species are defined by the properties of that molecule. This leads to different energy landscapes of different species (also isotopes) and therefore to a specific pattern, that can be used to identify the molecule (or isotope).

Here, we are interested in molecular transitions whose energy difference is associated with a wavelength in the infrared spectral range. In the infrared the typical process is a combination of vibrational and rotational transitions of the molecule, where the shape of the molecule oscillates.

In a semi-classical picture, the different atoms in a molecule change their relative distances and in some cases this introduces a dipole moment in the molecule due to a non-symmetric

electron distribution. An oscillating electric dipole emits electromagnetic radiation at its resonance frequency. In this sense the absorption of a resonant photon leads to an excitation of a vibrational mode of the molecule. Additionally, higher order electromagnetic moments (e.g. quadrupoles) can also induce photon absorption/emmission.

Similarly, if the rotation of the molecule leads to an oscillating dipole, a transition between levels of different rotational quanta is possible. Typically, the energy associated with the rotation of a molecule is smaller than the one for vibration, i.e. it requires less force to rotate a molecule and more force to bend or stretch it. Purely rotational transitions therefore occur in the less energetic micro-wave region of the electromagnetic spectrum. In the typical case, however, if the molecule shows a dipole when vibrationally excited an additional rotation will lead to additional rotational transitions. This means for every vibrational transition there will be a set of rotational transitions that slightly extend or decrease the difference between the energy levels of the molecule. These are then called vibrational/rotational transitions. Figure 2.1 shows a schematic energy level distribution for a single vibrational transition. Here, depending on the added angular momentum $\Delta J = \pm 1, 0$, the transitions, and therefore the resulting lines in the spectrum, are separated into three regions called the P-, Q- and R-branches. Note that due to the conservation of angular momentum, a transition with $\Delta J = 0$ is dipole forbidden, i.e. a boson (here the photon) has to carry an integer angular momentum or spin other than zero. For this reason, no lines contributed to the Q-branch occur in the CO_2 spectrum shown in Fig. 2.2. However, in cases where the specific molecular transition is possible via a combination of two independent transitions, the total angular momentum change can still be $\Delta J = 1 + (-1) = 0$.

CO_2 is a linear triatomic molecule with the oxygen atom in the center. This system can be described by a set of three fundamental vibrational modes: the symmetric stretching mode (ν_1), the bending mode (ν_2) and the antisymmetric stretching mode ν_3, and a rotational mode described by the angular momentum l (e.g. Rothman and Young [1981]). Any vibrational/rotational transition can be described as a linear combination of these fundamental modes. In the near infrared region two absorption bands of CO_2 around 6300 cm^{-1} are used, specifically the (1401) $\rightarrow$ (0000) and the (2102) $\rightarrow$ (0000) transitions [Yang et al., 2002].

CH_4 contains 4 hydrogen atoms centered in a tetrahedal structure around a centre carbon atom, the situation is similar to CO_2 but the set of fundamental modes has to be extended to include a total of 4 eigenfrequencies. The absorption band used in the NIR around 6000 cm^{-1} originates in the (0020) $\rightarrow$ (0000) transition of CH_4 [Wallace and Livingston, 1990].

At higher energies transitions of the (outer) electrons become more prominent and dominate the spectral composition in the ultra-violet and visible spectral region. Molecular oxygen (O_2), which is also investigated in the frame of this study, shows a electronic

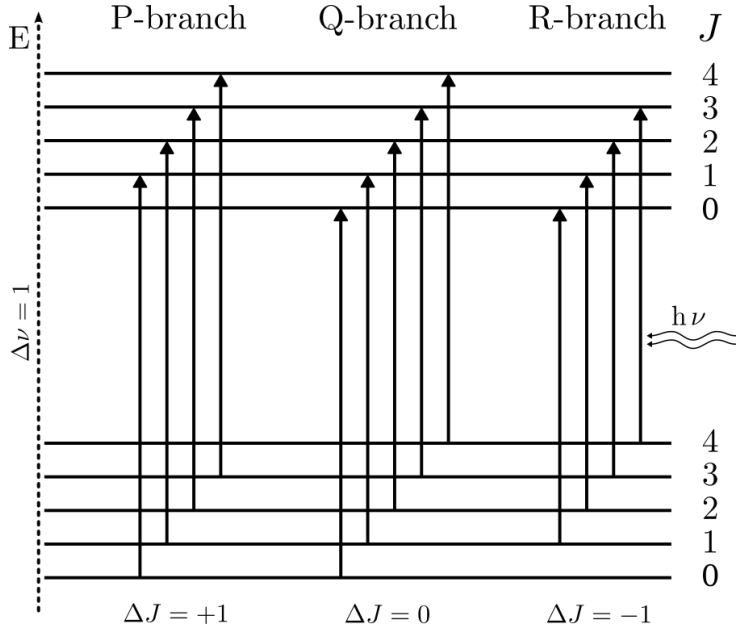

Figure 2.1.: Schematic overview of the possible molecular transitions between energy levels of a vibrational/rotational molecule. With a change in the angular momentum quantum number $\Delta J = \pm 1, 0$ induced by photon absorption, for every vibrational transition several rotational transitions are possible.

transition that is active in the near-infrared. The NIR O_2 transition 0-0 $^1\Delta - ^3\Sigma$ around 7880 cm^{-1} is used [Yang et al., 2002]. In the high-energy spectral regime, transitions of inner electrons or atomic nuclei become relevant (X- and γ-rays). On the low-energy end of the electromagnetic spectrum excitations of nuclear or electronic spin states like nuclear magnetic resonsance (NMR) or electronic spin resonance (ESR) are dominant, but these are not of interest in the context of this thesis.

The positions of the spectral lines for the possible molecular transitions can be calculated and/or measured and are tabulated in the high-resolution transmission molecular absorption database (HITRAN, Rothman et al. [2005]). Figure 2.2 shows a subset of the HITRAN 2004 lines in the near-infrared spectral region used in part of this study for the three target species O_2, CO_2 and CH_4.

2.1.2. Spectral Line Shape

In the previous subsection the absorption or emission process was described for a single molecule. In spectroscopy there is usually an ensemble of molecules present at the same time and the single contributions of the molecules add up. Since some of the ensemble molecules are in a different state, the transitions described earlier happen simultaneously

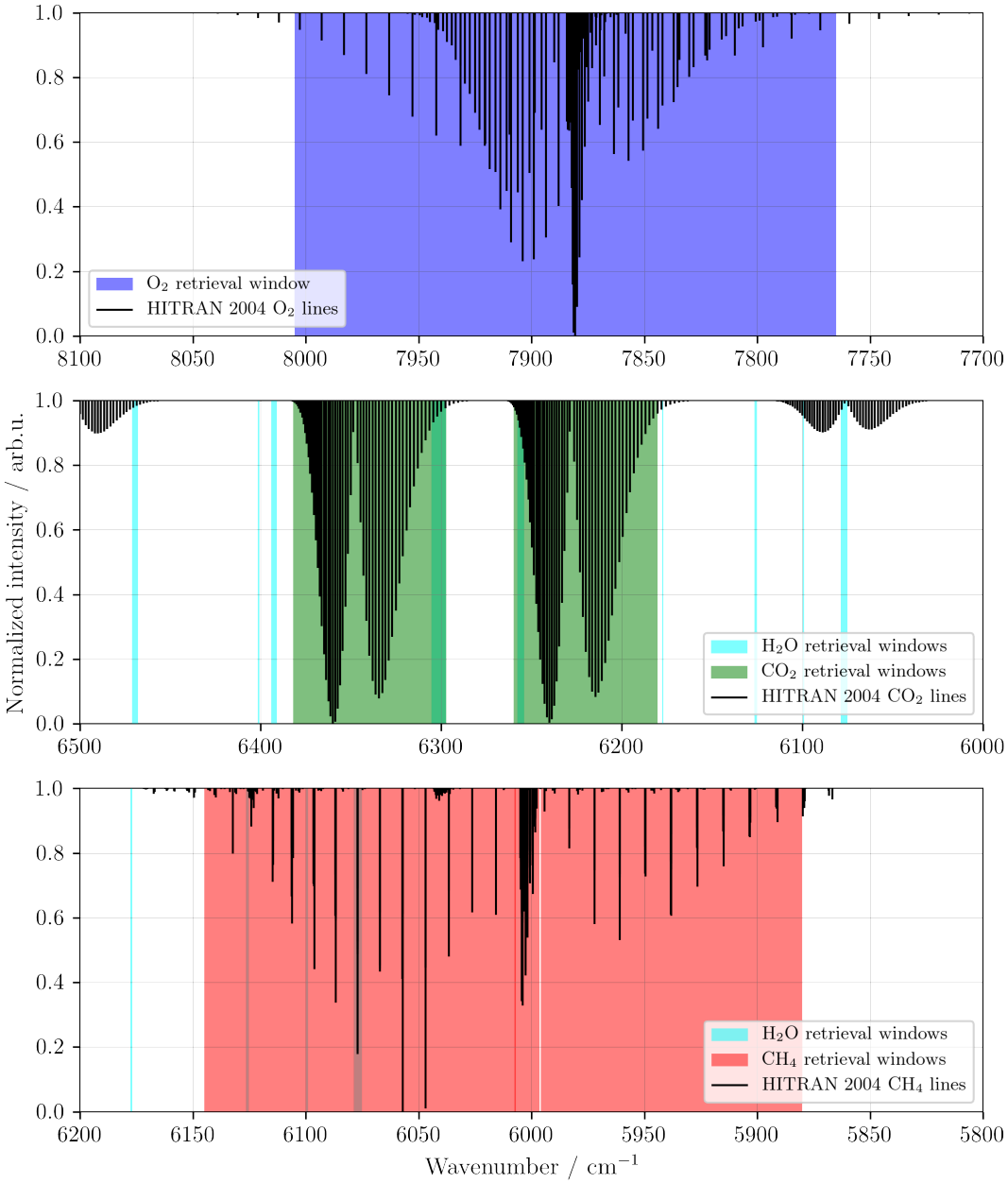

Figure 2.2.: Spectral line positions (black lines) from the HITRAN 2004 database [Rothman et al., 2005] and retrieval windows (shaded regions) of CO_2, CH_4, O_2 and H_2O used in the TCCON.

for different molecules in the same measurement. This leads to statistical effects on the spectral line intensities and shapes.

The intensity of an observed spectral line is determined by the energy state population density of the molecular ensemble. In thermodynamic equilibrium this is described by the Boltzmann-distribution as a function of temperature. In lower energy states, however, the population density is further limited by the number of available states for a given level, i.e. the degeneracy of the state.

Concerning the shape of the spectral lines, several mechanisms are responsible for broadening the line. A broadening of a spectral line corresponds to a change of the energy gap between different levels of the molecule.

The most fundamental mechanism is referred to as natural line width. It implies, that even under ideal conditions, the line has a finite width. The natural line width originates in Heisenberg's uncertainty principle. Traditionally, it defines the limit for accurately determining either momentum or position. A variation of the principle can be transferred to the energy–time domain (see Demtröder [2011]) to yield $\Delta E_k \tau_k = \hbar$, where for a given excited state k, the determination of the energy ΔE_k is limited to $\frac{\hbar}{\tau_k}$. Thus, the lifetime τ_k of the excitation determines the lowest possible line width. The naturally broadened line has a Lorentzian shape.

In the molecular ensemble, additional mechanisms contribute to the line broadening. The most important ones in the context of this thesis are pressure and Doppler broadening. Pressure broadening occurs, when the molecules are colliding with other molecules. The collision can shorten the lifetime of the excited state and the reduced lifetime increases the associated energy gap, as discussed before. The magnitude of the broadening effect is dependent on the collision probability and this in turn on the mean free path of the molecule in an ensemble, which is determined by density and temperature of the gas and like the natural line width has a Lorentzian shape.

The temperature of the gas has an additional effect via molecular translation. Some of the molecules move along the line-of-sight between source and observer. As a result the associated observed frequency will be shifted to a slightly lesser or higher frequency. This Doppler effect occurs for all molecules in the gas with a velocity vector contribution parallel to the light path to the instrument. In thermodynamic equilibrium, the velocity distribution of the ensemble is symmetric and induces Doppler-broadening of the spectral lines, dependent on the average velocity of the molecules determined by the gas temperature. For gases with a Maxwell velocity distribution, the Doppler-broadening has a Gaussian shape.

The effects of various broadening mechanisms combine to a single line shape for each transition. The convolution of Lorentzian and Gaussian distributions is generally referred

to as a Voigtian line shape, which is also the standard approach to calculate theoretical lines in the retrieval process used in this study. There are current efforts to include further mechanisms, e.g. line mixing or speed dependency, into the theoretical line shape calculation to improve the spectroscopic assumptions used in the retrieval process [Mendonca et al., 2016].

2.1.3. Atmospheric Absorption

The primary goal of atmospheric absorption spectroscopy is to infer the amount of a target species in the atmosphere. In this real-world application several additional complications have to be considered. The observed spectrum of a target gas shows contributions from samples at different altitudes (pressures), temperatures and concentrations. As an example, a solar spectrum measured with a ground-based instrument will show a combination of features from various atmospheric layers, each with their own set of properties. The mole fraction of the gas might be different in different altitudes and additionally show different amounts of broadening, depending on pressure and temperature. Ground-based spectra will show contributions of all atmospheric layers to the spectral line shape.

Additionally, atmospheric refraction, dependent on the viewing geometry, has to be taken into account. In principle the observed ground-based spectrum highly depends on the light path through the atmosphere. In order to infer the amount of gas that caused the spectral absorption line, accurate knowledge of the light path is necessary, such that the theoretically expected line shape can be compared with the measured one. The details of this retrieval process are discussed in chapter 2.3. Typically, ground-based absorption measurements are performed under clear sky conditions, such that scattering processes in the light path can be neglected, especially when the source intensity is large.

2.2. Fourier Transform Infrared Spectrometry

2.2.1. Spectrometry

As discussed in Section 2.1, remote sensing of atmospheric gases can be performed using their absorption spectra. In order to measure an absorption spectrum, a light source above the atmosphere is needed, as well as a defined light path trough the atmosphere containing the target species. The transmitted light is then analysed with a spectrometer.

There are several methods available to measure an absorption spectrum. Spectrometers using dispersive elements, e.g. prisms or gratings, are typically used in the ultraviolet/visible (UV/VIS) spectral region and are therefore mainly limited to recording electronic

transitions of the target molecules. Microwave spectrometers can observe e.g. rotational transitions in molecules that have much lower energies and typically operate in the GHz spectral domain. In the infrared, the best option is to use a FTS. As this is the method of choice in this work, a more detailed description of the working principle is given below.

2.2.2. Michelson Interferometry

In optical spectrometers a dispersive element, e.g. a grating, is used to map the spectral information contained in the incident light spatially differentiated onto a plane, which is then recorded by a detector array. A different method, without a dispersive element is given by two beam interferometry. The traditional setup is called a Michelson Interferometer. The incident light beam is split into two parts and later recombined. One arm has a fixed length and the length of the second arm is varied (see Fig. 2.3). During recombination, the two light beams of a certain wavelength interfere with each other, depending on the path difference of the arms. The intensity of the recombined light beam is recorded by a single detector element as a function of path difference, i.e. the interferogram. The spectral information is contained in the recorded interferogram and can be obtained via Fourier-transformation of the interferogram.

2.2.3. Fourier Transform

The mathematical relation between the spatial (i.e. path difference) and the spectral (wavenumber) domain is performed by a Fourier-transform. The main conclusion of the original Fourier series is that any periodic signal $f(t)$ can be reproduced by a sum of various sine and cosine functions of different frequencies and with different (Fourier-) coefficients A_k and B_k [Butz, 2012]:

$$f(t) = \sum_{k=-\infty}^{+\infty} (A_k \cos \omega_k t + B_k \sin \omega_k t) \tag{2.1}$$

with the angular frequency $\omega_k = \frac{2\pi k}{T}$. Using trigonometric identities, i.e. Euler's formula $e^{i\alpha t} = \cos \alpha t + i \sin \alpha t$, this can be simplified by substituting the sin and cos by an exponential function with a complex argument, yielding a shortened variant of the Fourier series:

$$f(t) = \sum_{k=-\infty}^{+\infty} \left(C_k e^{i\omega_k t}\right) \tag{2.2}$$

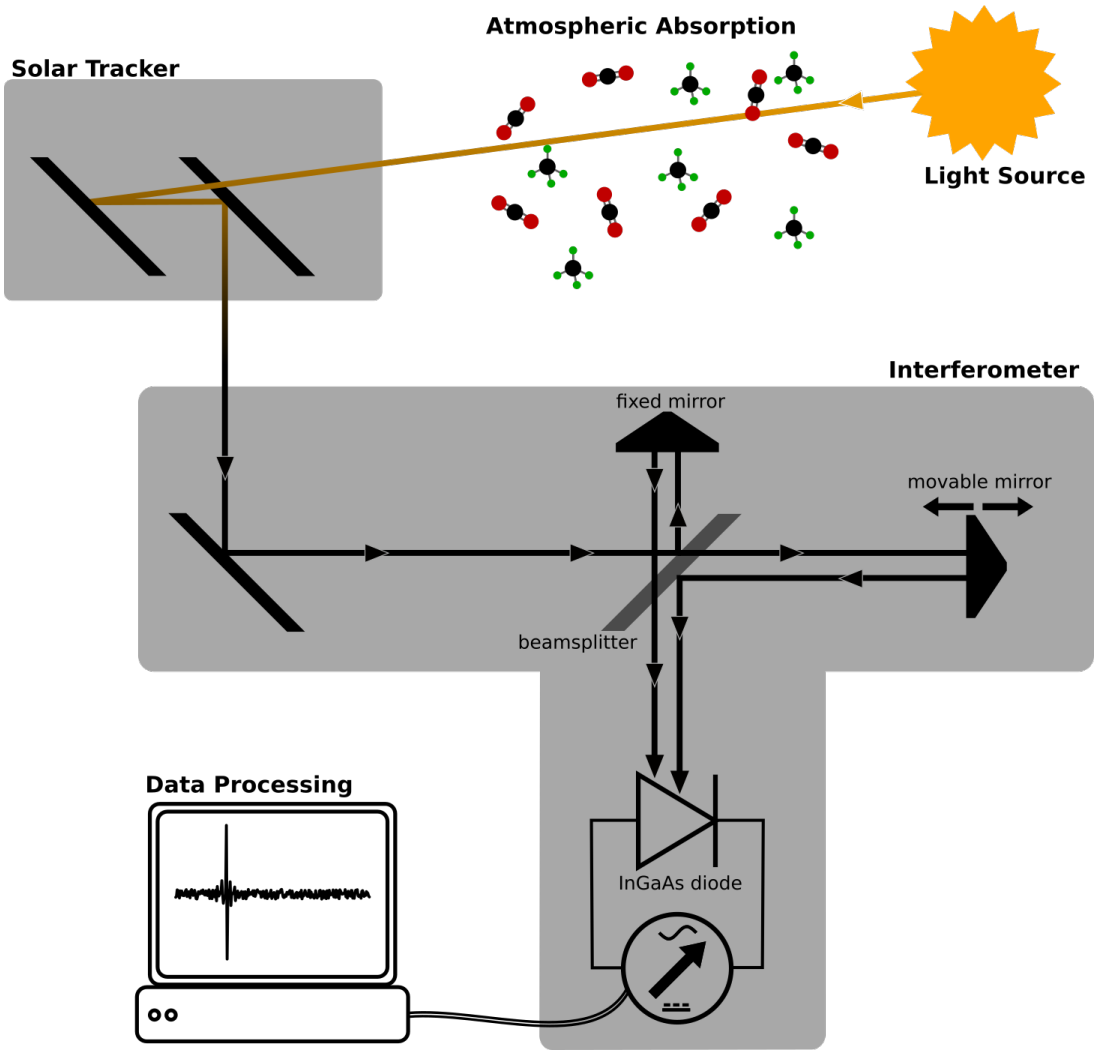

Figure 2.3.: A diagram showing the measurement principle of FTIR spectrometry. Light from the (solar) light source is absorbed by atmospheric trace gases and the residual light is measured by an Michelson-Interferometer setup: By moving one mirror, the (InGaAs-) detector registers signal variations corresponding to the interference of the short and long light path. The resulting interferogram typically shows a characteristic peak at ZPD.

The identification of the Fourier coefficients C_k can then be performed by:

$$C_k = \frac{1}{T} \int_{-\infty}^{+\infty} f(t) e^{-i\omega_k t} \mathrm{d}t \tag{2.3}$$

This yields via translation into the spatial domain (x), the Fourier decomposition of an interferogram $I(x)$ as a function of the wavenumber $B(\sigma)$ (see Davis et al. [2001]):

$$B(\sigma) = \int_{-\infty}^{+\infty} I(x) e^{-i2\pi\sigma x} \mathrm{d}x \tag{2.4}$$

The resulting spectrum contains the absorption lines of the atmospheric target species as discussed in Sec. 2.1. The approach to retrieve the dry-air mole fractions of the target gases from the measured spectra is discussed in the next section.

2.3. Trace gas retrieval

2.3.1. Retrieval Principle

The retrieval of information on the dry-air-mole fractions (DMFs) poses an *Inverse Problem*. Because there is not enough information to directly calculate the DMF from the spectrum, e.g. by integrating the area under the absorption line, the problem is ill-posed and ill-conditioned. The typical approach to solve this class of inverse problems is to employ *Optimal Estimation* techniques. The standard literature to highlight the application of the optimal estimation technique to the inverse problem of atmospheric remote sensing is given by Rodgers [2000].

In the optimal estimation approach, the lack of information necessary to solve the problem is compensated by the introduction of additional a priori information. This information is *a priori*, meaning it is independent of the measurement itself. In an iterative process the a priori information is adjusted by a forward model resulting in a better estimate for the target quantity.

The full optimal estimation process is especially necessary if in addition to the DMF, a vertical distribution of the DMF is to be retrieved. If only the column-averaged DMF of a target gas is wanted, the retrieval process can be simplified. Within the TCCON, the standard retrieval approach involves the calculation of a theoretical spectrum from a priori information and then iteratively adjusting the target DMF profile until the difference

between the measured and calculated spectra are minimal using a least-square fitting algorithm. The atmospheric a priori profile is thereby scaled by a factor and the resulting column average calculated. The standard retrieval code within TCCON is GFIT within the GGG software suite. In the following the single parts of the retrieval are presented. The following and additional information can be obtained from Wunch et al. [2011a] and Wunch et al. [2015].

2.3.2. Spectroscopic Linelist

The calculation of the theoretical spectrum used in the retrieval of the DMFs requires accurate knowledge of the spectral line parameters. GGG contains a list of line parameters for the retrieval windows that is based on the HITRAN database (see Sec. 2.1.1 and Fig. 2.2). Some of these line parameters are adjusted to perform better in a real-world atmospheric scenario by comparison to lab spectra and balloon-borne FTS measurements. The TCCON GGG linelist is distributed within the GGG software suite [Wunch et al., 2015].

2.3.3. Atmospheric Model

The atmospheric model describes the altitude/pressure dependent temperature and relative humidity profile that is used in the calculation of the theoretical spectrum. In the standard TCCON setting one atmospheric model is used per day. The data are taken from the NCEP/NCAR reanalysis data [NCEPNCAR, 2016] and interpolated to the measurement site specific coordinates, to local noon and to the altitude levels of the retrieval. The stratospheric part is replaced by the US standard atmosphere scaled by a surface pressure offset.

2.3.4. A Priori Profiles

The TCCON retrieval uses a priori profiles for the retrieval gases that are based on balloon-bourne and satellite profile measurements in mid-latitudes. In case of H_2O, the same NCEP/NCAR reanalysis data as in the atmospheric model are used. For CO_2 an empirical model was developed from values from the GLOBALVIEW-CO2 product. This model has a latitudinal and seasonal dependency, and a long-term increase, and is evaluated for each measurement day in the retrieval to ensure an optimal a priori. The a priori profiles of the other gases measured within TCCON (CH_4, CO and N_2O) are based on a simple empirical model which are themselves based on in situ measurements [Wunch et al., 2015].

2.3.5. Averaging Kernels

The averaging kernels associated with a remote sensing measurement weight the contribution of the different atmospheric layers according to their potential to change the total column amount. They are therefore a measure of the altitude sensitivity of the measurement. The retrieved profile can be expressed as the change to the a priori profile $\mathbf{x_a}$ by adding the difference of the true atmospheric profile $\mathbf{x_t}$ and the a priori and weighting them by their altitude sensitivity, i.e. the averaging kernel $\mathbf{A}$ [Rodgers, 2000]:

$$\mathbf{x_r} = \mathbf{x_a} + \mathbf{A}(\mathbf{x_t} - \mathbf{x_a}) \tag{2.5}$$

In a full profile retrieval the averaging kernels will have a matrix shape of size $\mathsf{N} \times \mathsf{N}$, at N altitude levels. In the theoretical, ideal measurement a change of the DMF in a single level does not change the contribution of other levels. In this case the averaging kernel would be an identity matrix. As TCCON uses a profile scaling retrieval the situation is slightly different. A change in one level will result in a change in all levels, which results in the rows of the averaging kernel matrix being repetitions of one vector, reflecting the sensitivity contribution of the retrieval levels. In GGG this vector of length N can be calculated in the retrieval process and is typically referred to as the averaging kernel.

2.3.6. Comparing Datasets

When comparing the retrieved DMFs of an FTS with other datasets, the retrieval process has to be considered. As previously discussed, the averaging kernels of the FTS product reflect the sensitivity of the measurement at a certain altitude. In-situ measurements or model results typically have a uniform sensitivity throughout the column. This results in the need to adjust, or smooth, the in-situ or model profile in order to make it comparable with the FTS measurement.

For example, if the FTS measurement shows a low sensitivity in the stratosphere, the stratospheric contribution has a small impact on the total column. A stratospheric feature that is pronounced in the in-situ measurements would result in an offset when comparing the two datasets. For a proper comparison, the in-situ measurement has to be adjusted to simulate the same sensitivity as the FTS.

Similarly, different FTS measurements might have different averaging kernels and therefore need to be smoothed as well to make them comparable, the difference being that now both measurements have a non uniform sensitivity. A description of the appropriate averaging kernel smoothing method for a given comparison will be in chapter 3 for the FTS-to-FTS comparison and in chapter 4 for a FTS-to-model comparison.

2.3.7. Calculation Of Dry-Air Mole Fractions

The output of the GFIT algorithm provides vertical columns (VC_{gas}), of the target gas, which have to be converted to dry-air mole fractions. There are two methods to do this. The standard TCCON processing method uses the vertical column of O_2 retrieved from the same spectrum to scale the target gas' vertical column:

$$\mathrm{xGas} = \frac{\mathrm{VC_{gas}}}{\mathrm{VC_{O_2}}} 0.2095 \tag{2.6}$$

The O_2 DMF of 20.95 % is well known and assumed constant. The main advantage of this approach is that systematic errors, like solar tracking pointing errors, common to both vertical column retrievals cancel out [Yang et al., 2002]. The second option to calculate the target gas DMFs uses the atmospheric surface pressure and a water correction:

$$\mathrm{xGas} = \frac{\mathrm{VC_{gas}}}{\frac{p_0 \mathrm{N_A}}{m_{dry}^{air}\bar{g}} - \mathrm{VC_{H_2O}} \frac{m_{\mathrm{H_2O}}}{m_{\mathrm{dry}}^{\mathrm{air}}}} \tag{2.7}$$

Here, xGas denotes the DMF of the target species, VC_{gas} the vertical column and p_0 the surface pressure. N_A is Avogadro's number and the molecular masses of water, $m_{H_2O} = 18.01534\ \mathrm{g\,mol^{-1}}$, and dry air, $m_{\mathrm{dry}}^{\mathrm{air}} = 28.9644\ \mathrm{g\,mol^{-1}}$, are given. $\bar{g}$ denotes the column averaged gravitational acceleration at the measurement site. For this approach no additional retrieval of O_2 is necessary, however the surface pressure needs to be accurately measured in-situ. Additionally systematic errors, e.g. pointing errors, can affect the retrieval, as they are not canceled out via ratio with O_2. The surface pressure in Ny-Ålesund, necessary for the retrieval in this study, is performed by the Baseline Surface Radiation Network (BSRN), located adjacent to the AWIPEV observatory and thus the FTS.

2.3.8. Postprocessing

Within the TCCON several post processing steps are performed after the total column DMFs are retrieved. These follow a network wide standard. For several TCCON sites vertically resolved aircraft measurements have been performed [Deutscher et al., 2010; Geibel et al., 2012; Messerschmidt et al., 2011; Wunch et al., 2011b]. In an extensive comparison, a calibration factor common to all TCCON sites has been found and the retrieved DMFs are corrected by this factor. Additionally, TCCON measurements show a residual airmass dependency at large zenith angles. An empirical correction is being applied to separate a symmetric from the expected asymmetric daily variation of the column averaged DMF [Wunch et al., 2011a].

3. Middle-infrared trace gas retrieval

The TCCON retrieves the dry-air mole fractions of CO_2 and CH_4 in the near-infrared (NIR) spectral region above 4000 cm^{-1}. The spectral features in this region are strong and have little interfering gases. The spatial coverage of the network has grown since its inception in 2004 to include currently more than 20 sites around the globe.

The NDACC on the other hand measures spectra in the mid-infrared (MIR) spectral region. The earliest atmospheric MIR spectra date back to the 1950's at Jungfraujoch (Switzerland) and the 1970's at Kitt Peak (USA). MIR spectra are recorded in Ny-Ålesund since 1992 and have been successfully used in research, e.g. to study the ozone chemistry in the upper atmosphere [Notholt et al., 1995]. The usage of MIR spectra to retrieve xCO_2 can extend the time series by 10 years, back to 1992 (earliest MIR spectra in Ny-Ålesund). In addition, the Moon has been used as a light source to record MIR atmospheric spectra [Notholt and Lehmann, 2003; Notholt and Schrems, 1994; Notholt et al., 1997]. And the successful retrieval of solar absorption trace gas measurements from MIR spectra would enable the usage of the available lunar MIR spectra as well, therefore closing the polar night gap (see chapter 4).

In this chapter the retrieval of the column-averaged dry-air mole fraction of CO_2 from NDACC MIR spectra is investigated, which would significantly increase both, the spatial and temporal availability of total column measurements. The investigation of a potential retrieval of xCH_4 from MIR spectra was done by Sussmann et al. [2013] and its application to the extension of the Ny-Ålesund time series is discussed in Sec. 3.5. The main focus in this chapter, however, lies on the previously not investigated xCO_2 MIR retrieval.

As discussed previously in section 2.3.7 the TCCON uses the co-retrieved O_2 column to calculate the dry-air mole fraction of CO_2 and CH_4 from NIR spectra. Compared to the TCCON NIR spectra, two main issues have to be overcome when using MIR spectra for the retrieval. The lack of spectral absorption lines of an atmospheric absorber with sufficiently well known abundance (like O_2 in the TCCON retrieval) and the presence of multiple interfering gases in the spectral region of interest. To address the first issue some N_2 absorption lines have been used to substitute the O_2 retrieval in the NIR approach (see Sec. 3.2). However, the observable multi-polar transitions are weak and their usage introduces more uncertainty than would be gained from a surface pressure retrieval approach (see Sec. 2.3.7). Concerning the second issue of strongly interfering gases, a selection of spectral

microwindows is introduced, that excludes most of the interfering gases and ensures a stable retrieval, see Sec. 3.1.

After initial tests with NDACC spectra from the Bremen and Ny-Ålesund sites, the study was extended to include 5 different stations, that record both NDACC and TCCON spectra: Ny-Ålesund and Bremen, operated by IUP Bremen, Izaña operated by KIT[1], Wollongong operated by UOW[2] and Lauder operated by NIWA[3]. The results from the NDACC retrievals and their comparison to TCCON were promising. However, a more detailed analysis reveals the strong impact of the chosen a priori on the retrieval. Therefore, the continued investigation focused solely on the Ny-Ålesund time series with its large seasonal variability and long time series, see Sec. 1.2.

Parallel to this study, Barthlott et al. [2015] developed a method to use microwindows in the MIR to retrieve xCO_2 as a tracer for instrument stability by comparing the retrieved DMFs to an empirical xCO_2 model. It can be concluded from their work, that a closer look at the impact of the measurements averaging kernel in conjunction with the chosen a priori is necessary. In their approach a pressure profile derived dampening factor is applied to correct for the averaging kernel smoothing effects which will be discussed in detail in this chapter.

The results of this work are published in Buschmann et al. [2016] and part of this chapter is taken from this paper. First, the method of retrieving xCO_2 from MIR spectral windows is discussed in section 3.1. This includes the selection of the spectral micro windows. The methodology of the averaging kernel smoothing used to make the MIR and NIR data sets comparable is discussed in section 3.3. The method for retrieving the xCO_2 from the MIR micro windows briefly discussed; a more detailed description is given in section 2.3.7. Afterwards, the influence of the a priori information on the retrieval is investigated. The differences found between the MIR and NIR retrievals might be explained by a differently shaped averaging kernel and therefore different sensitivities to different atmospheric layers. It will be investigated if taking the averaging kernel smoothing effects into account resolves the differences in the retrievals. This is investigated in section 3.4. The chapter concludes with a brief summary of the results.

[1]Institut für Meteorologie und Klimaforschung (IMK) - Atmosphärische Spurengase und Fernerkundung (ASF) at the Karlsruhe Institute of Technology, Karslruhe, Germany, `http://www.imk-asf.kit.edu/`

[2]Centre for Atmospheric Chemistry, University of Wollongong, Wollongong, Australia, `http://smah.uow.edu.au/cac/trace-gas/index.html`

[3]Lauder Atmospheric Research Station of the National Institute of Water and Atmospheric Research, Lauder, New Zealand, `https://www.niwa.co.nz/atmosphere/facilities/lauder-atmospheric-research-station`

Molecule	Center [cm^{-1}]	Width [cm^{-1}]	Quantum transition	Line intensity [$cm\,(molecule^{-1})$]	Lower state energy [cm^{-1}]
$^{16}O^{12}C^{18}O$	2620.83	0.55	$20002 \rightarrow 00001$	3.270×10^{-25}	26.5087
$^{16}O^{12}C^{18}O$	2626.63	0.45	$20002 \rightarrow 00001$	4.309×10^{-25}	100.1374
$^{16}O^{12}C^{18}O$	2627.35	0.50	$20002 \rightarrow 00001$	4.291×10^{-25}	112.6533
$^{16}O^{12}C^{18}O$	2629.61	0.67	$20002 \rightarrow 00001$	4.076×10^{-25}	154.6166
$^{16}O^{12}C^{16}O$	3160.22	0.16	$21103 \rightarrow 00001$	3.140×10^{-25}	316.7698
$^{16}O^{12}C^{16}O$	3161.70	0.20	$21103 \rightarrow 00001$	3.030×10^{-25}	273.868
$^{16}O^{12}C^{16}O$	3315.78	0.55	$21102 \rightarrow 00001$	1.726×10^{-24}	362.7882
$^{16}O^{12}C^{16}O$	3344.81	0.26	$21102 \rightarrow 00001$	7.747×10^{-25}	16.389

Table 3.1.: The mid-IR microwindows used in this study. Each window is characterized by the center wavenumber and its width. Additionally, the corresponding molecular transition is given. Data taken from Rothman et al. [2005, 2009]. Example spectral microwindows are shown in Fig. 3.1. *Published as Tab. 1 in Buschmann et al. [2016].*

3.1. Micro window selection

This section was published as section 2.2 in Buschmann et al. [2016]. References and citations have been updated.

In the mid-infrared region between 2000 and 4000 cm^{-1} in addition to CO_2, other, interfering gases have strong absorption lines. Some spectral regions are dominated by the interference gases, while in others CO_2 is the most prominent feature. This makes it impractical to select whole absorption bands for the retrieval, such as is done in the NIR by the TCCON. The high-resolution NDACC spectra allow the selection of microwindows that contain only single lines. The contribution of interfering gases to the single line shapes varies for different microwindows.

Multiple microwindows are fitted in three spectral regions: four microwindows at around 2624 cm^{-1}, two microwindows at 3160 cm^{-1} and two around 3330 cm^{-1}. The corresponding line parameters are taken from the GGG line list, which is based on the HITRAN (high-resolution transmission molecular absorption) database [Rothman et al., 2005, 2009]. These are shown in Table 3.1. Each of the spectral regions referred to above corresponds to a different optical filter or detector setting, and they are measured sequentially at acquisition. The retrieval is performed separately for each spectral interval and microwindow. Following this approach, we obtain eight different retrievals of xCO_2, one for each microwindow.

Retrievals from microwindows within the same spectral interval were averaged and used to derive daily averages to correlate with the daily-averaged TCCON retrievals. This approach circumvents the temporal coincidence problem that arises due to the different acquisition procedures described in Sect. 1.2.

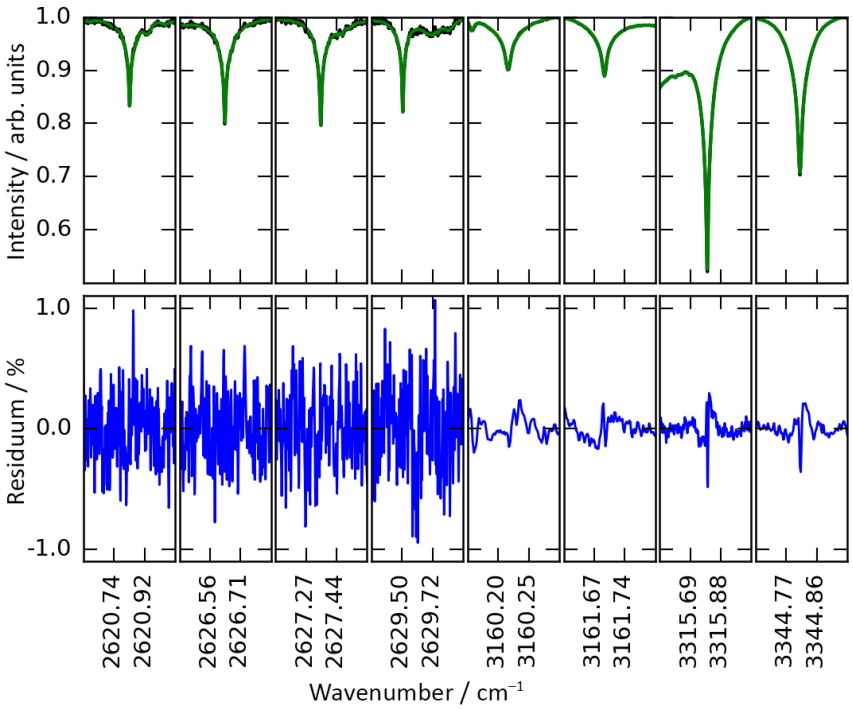

Figure 3.1.: An example fit of the measured (black) with the calculated (green) spectrum and their residuals (blue) for the various microwindows used. Note the different signal-to-noise ratio due to different instrument setup (see Sect. 3.1). *Published as Fig. 1 in Buschmann et al. [2016].*

3.2. MIR xCO_2 retrieval

This section was published as section 2.3 in Buschmann et al. [2016]. References and citations have been updated.

The MIR xCO_2 retrieval has been performed with the profile scaling algorithm GFIT (version 4.8.6 in GGG2012), which is also used for the TCCON xCO_2 retrievals. In GFIT a priori profiles of the target gas; gases of interest; and pressure, temperature and H_2O are convolved with an instrument lineshape model to simulate a spectrum. The gas profiles are scaled and other spectral parameters adjusted to provide the best fit to the measured spectrum by minimizing the residual. From these scaled profiles, the amount of the target gas is retrieved. An example fit is shown in Fig. 3.1.

The standard TCCON retrieval uses O_2 retrieved from the same spectra as the target gases in the band at 7885 cm^{-1} to estimate the total dry-air column. The retrieved CO_2 column is then divided by this retrieved O_2 column to derive the column average dry-air mole fraction. The method is explained in further detail in Wunch et al. [2011a].

The same software version was used to analyze the MIR spectra. To benefit from the abovementioned ratio approach, a MIR active species with a well-known atmospheric

	TCCON	2600 cm^{-1}	3100 cm^{-1}	3300 cm^{-1}
σ	1.13	2.06	3.21	1.16
$\sigma/\sqrt{N}$	0.23	0.96	1.67	0.60

Table 3.2.: Overview over the estimated errors from the different retrievals. Given are both the mean standard deviation of the daily mean and the mean standard error for N measurements, in ppm. *Published as Tab. 2 in Buschmann et al. [2016].*

abundance would be needed. Only N_2 has some weak absorption lines in the target region: its multipolar $1 \rightarrow 0$ transition. The suitability of these lines for atmospheric retrieval was previously investigated by Goldman et al. [2007]. Due to the very low intensity, the retrieved N_2 mole fractions introduced more noise than was compensated by use of the ratio, meaning that N_2 was not able to be used as an internal standard.

Instead, mole fractions from the MIR spectra are calculated by normalization by the dry-air column abundance inferred from an independent measurement of surface pressure. The vertical column of H_2O was also retrieved from a dedicated H_2O microwindow in the vicinity of the respective CO_2 microwindow. Total column CO_2 was then calculated as described in Appendix A in Wunch et al. [2011b] by applying

$$\mathrm{xCO_2} = \frac{\mathrm{VC_{CO_2}}}{\frac{P_\mathrm{s}}{\langle g_\mathrm{air}\rangle\, m_\mathrm{air}^\mathrm{dry}} - \frac{\mathrm{VC_{H_2O}} \cdot m_{\mathrm{H_2O}}}{m_\mathrm{air}}} \tag{3.1}$$

Here, $m_\mathrm{air}^\mathrm{dry}$ and $m_{\mathrm{H_2O}}$ denote the molecular masses of dry air and water, respectively; P_s the surface pressure; and $\langle g_\mathrm{air}\rangle$ the column-averaged gravitational acceleration. $\mathrm{VC_{CO_2}}$ and $\mathrm{VC_{H_2O}}$ are the retrieved vertical column amounts from the GFIT output.

The retrieved dry-air mole fractions are then quality-controlled by removing data points with high solar zenith angles ($> 80°$) and/or with a high relative retrieval error ($> 20\,\%$). Table 3.2 shows uncertainty estimates for the resulting time series, based on the standard deviation of the daily means. The mean of the standard deviations for the three microwindow regions is compared to the standard TCCON results. Additionally the standard error is shown in order to better reflect the uncertainty in the daily mean, which is also influenced by the number of measurements on each day. Only days with two or more measurements have been used. This approach results in an error estimate (1σ) of 1.13 ppm for the Ny-Ålesund TCCON standard product (≈ 0.3 %) and 2.06 ppm (0.5 %) for the 2600 cm^{-1} microwindow (see Table 3.2).

As a basis for the analysis, daily means of in total 335 days (TCCON) and 223 days (NDACC) between March 2005 and May 2013 were used. The average number of measurements per day was about 30 for TCCON and 5 for the NDACC 2000 cm^{-1} region.

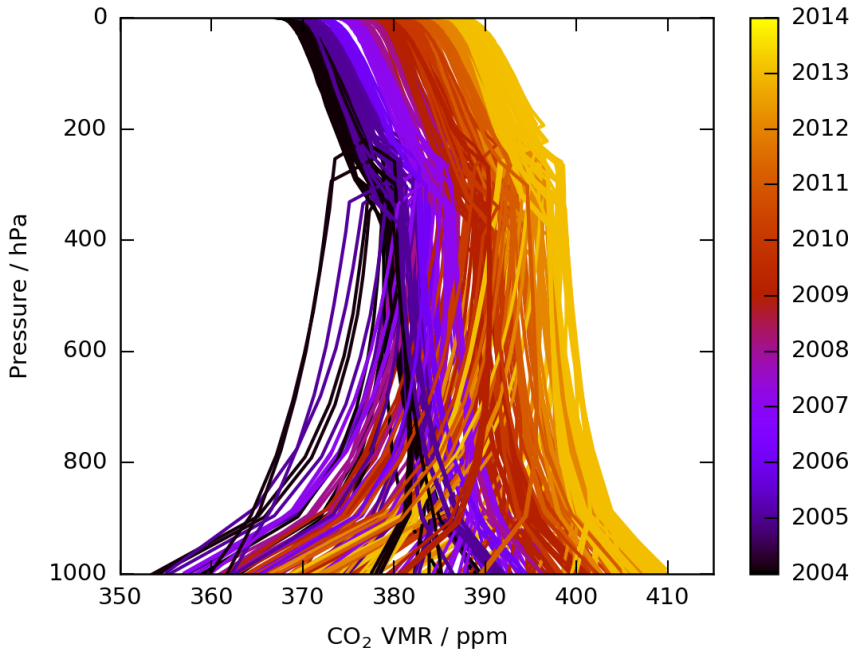

Figure 3.2.: The TCCON a priori profiles calculated for Ny-Ålesund and the time frame of this analysis. *Published as Fig. 2 in Buschmann et al. [2016].*

3.3. A priori influence

This section was published as section 3 in Buschmann et al. [2016]. References and citations have been updated.

Following Rodgers [2000] and Rodgers and Connor [2003], the retrieval of the total column abundance $\hat{\mathbf{x}}$ (for a true quantity $\mathbf{x}$) as described in Sect. 3.2 depends on both the choice of the a priori profile $\mathbf{x}_\mathrm{a}$ and the measurements averaging kernel $\mathbf{A}$.

Thus, Eq. (3) in Rodgers and Connor [2003] gives

$$\hat{\mathbf{x}} - \mathbf{x}_\mathrm{a} = \mathbf{A}(\mathbf{x} - \mathbf{x}_\mathrm{a}) + \epsilon_x, \tag{3.2}$$

where ϵ_x is the random and systematic error term. If the measurement information content does not fully constrain the retrieval, the result will be influenced by the a priori. Within TCCON a latitude- and time-dependent empirical model is used to simulate an xCO_2 profile that is already quite close to the true atmospheric profile. There is one TCCON a priori profile per day calculated for local noon. These are shown in Fig. 3.2.

Usage of this modeled a priori profile in the MIR retrieval can give an overly favorable impression of the information content of the MIR retrieval. Even if there is no additional information to be retrieved from the spectra, a reasonably good agreement between the NIR and MIR retrievals is still to be expected, because the smoothing error term tends to

zero when the prior is approximately equal to the true atmospheric state (for a detailed explanation see Sect. 3.4).

To investigate this, xCO_2 has been retrieved from both MIR and NIR spectra, once using the standard, time-dependent TCCON a priori, and once using a fixed, constant a priori profile of 379 ppm throughout the atmosphere. Apart from the different a priori, the same retrieval and post-processing parameters have been used as in the original retrievals with the TCCON a priori.

The comparison of the NIR (TCCON) time series with modeled and fixed a prioris shows a clear pattern. This corresponds to an overestimation of the seasonal cycle amplitude by the retrieval using a fixed a priori compared to the standard a priori. At seasonal maximum the difference is negative, and at the seasonal minimum positive. The same pattern can be deduced from the slope in the correlation plot in Fig. 3.3. This can be attributed to the usage of a fixed a priori in conjunction with the solar-zenith-angle-dependent averaging kernel (see Fig. 3.4). The solar zenith angles are generally larger in spring and autumn than in summer. The TCCON averaging kernels show an increased sensitivity in the troposphere. This coincides with the seasonal maximum of xCO_2 in spring and with the seasonal minimum in autumn. In these cases the TCCON averaging kernel diverges from being close to 1, and subsequently the smoothing error contributions increase if the prior differs from the true atmospheric state. Thus the residual pattern in Fig. 3.3 originates from the shape of the averaging kernels.

In the case of the MIR NDACC spectra, the results of the retrieval with the TCCON a priori in comparison to that with a fixed a priori can be seen in Fig. 3.5. Both time series (the NDACC retrieval with the TCCON a priori and that with the fixed a priori) capture the secular trend, and no residual trend is visible. The seasonal cycle amplitude, however, is damped in the NDACC retrieval (shown here are the results of the 2600 cm^{-1} microwindow; other regions show comparable results). A clear seasonal structure can be seen in the residual.

In order to quantify the effect that the different a priori information has on the retrievals, a simple function (see Eq. 3.3) has been fitted to each time series (see Fig. 3.6):

$$xCO_2(t) = a + b \cdot t + A \cdot \sin(2\pi \cdot t), \tag{3.3}$$

where a is an offset at the beginning of the partial time series (1 January 2009), b is the linear trend per year and A is the amplitude of the seasonal cycle. The fit parameters are presented in Table 3.3. The comparison of the fitted amplitudes for the different retrievals allows for an estimate of the magnitude of the dampened seasonal cycle amplitude.

The results show a slight increase from the case of the standard TCCON retrieval to the TCCON retrieval with a fixed a priori by a factor of 1.14 (as was discussed earlier and can be seen in the correlation plot in Fig. 3.3). However, the fixed a priori NDACC retrieval

Retrieval	a [ppm]	b [ppm yr^{-1}]	A [ppm]
TCCON	383.27 ± 0.20	2.23 ± 0.09	5.73 ± 0.14
TCCON fixed	383.55 ± 0.19	2.21 ± 0.08	6.55 ± 0.14
NDACC	381.93 ± 0.64	2.41 ± 0.24	5.60 ± 0.49
NDACC fixed	381.08 ± 0.67	2.44 ± 0.28	2.64 ± 0.50

Table 3.3.: Fit parameters corresponding to the fits of the time series in Fig. 3.6 and in Eq. (3.3). Units are xCO_2 in ppm as a function of time in decimal years starting 1 January 2009. Uncertainty estimates are 1σ fitting errors. *Published as Tab. 3 in Buschmann et al. [2016].*

shows a decrease in the seasonal cycle amplitude. The amplitude of the NDACC retrieval with modeled a priori is found to be 2.12 times larger than the amplitude of the fixed a priori NDACC retrieval.

Similar to the approach used above for the TCCON case, we now investigate whether this is due to the differences in the averaging kernel, i.e., the sensitivity of the retrievals to different height levels. The tropospheric (or stratospheric) contribution of a retrieval can be estimated by integrating the averaging kernels for a retrieval (normalized on a pressure grid) over the contributing pressure column. Thus, the averaging kernels have been integrated in two parts, separated at the tropopause height at 300 hPa (see Fig. 3.7).

As can be seen in Fig. 3.4, in contrast to the NDACC xCO_2 kernels the TCCON averaging kernels strongly vary with the solar zenith angle. This leads to a zenith-angle-dependent ratio between the stratospheric and tropospheric contribution of the averaging kernels.

For the presented time series of NDACC xCO_2 from the 2600 cm^{-1} microwindow the average solar zenith angle is 69°. For this angle, a ratio of 2.05 of the tropospheric averaging kernel contribution of TCCON to NDACC xCO_2 can be calculated. Values of 1.80 and 2.18 are calculated for solar zenith angles of 40 and 80°, respectively. Assuming that variability in CO_2 occurs solely in the troposphere (i.e., that the seasonal variation in the stratosphere is negligible), a change in tropospheric CO_2 would result in a signal that is retrieved as being 2 times smaller than that retrieved from TCCON. This is in good agreement with the tropospheric contribution calculated from the time series' fits with a fixed a priori described above (2.12).

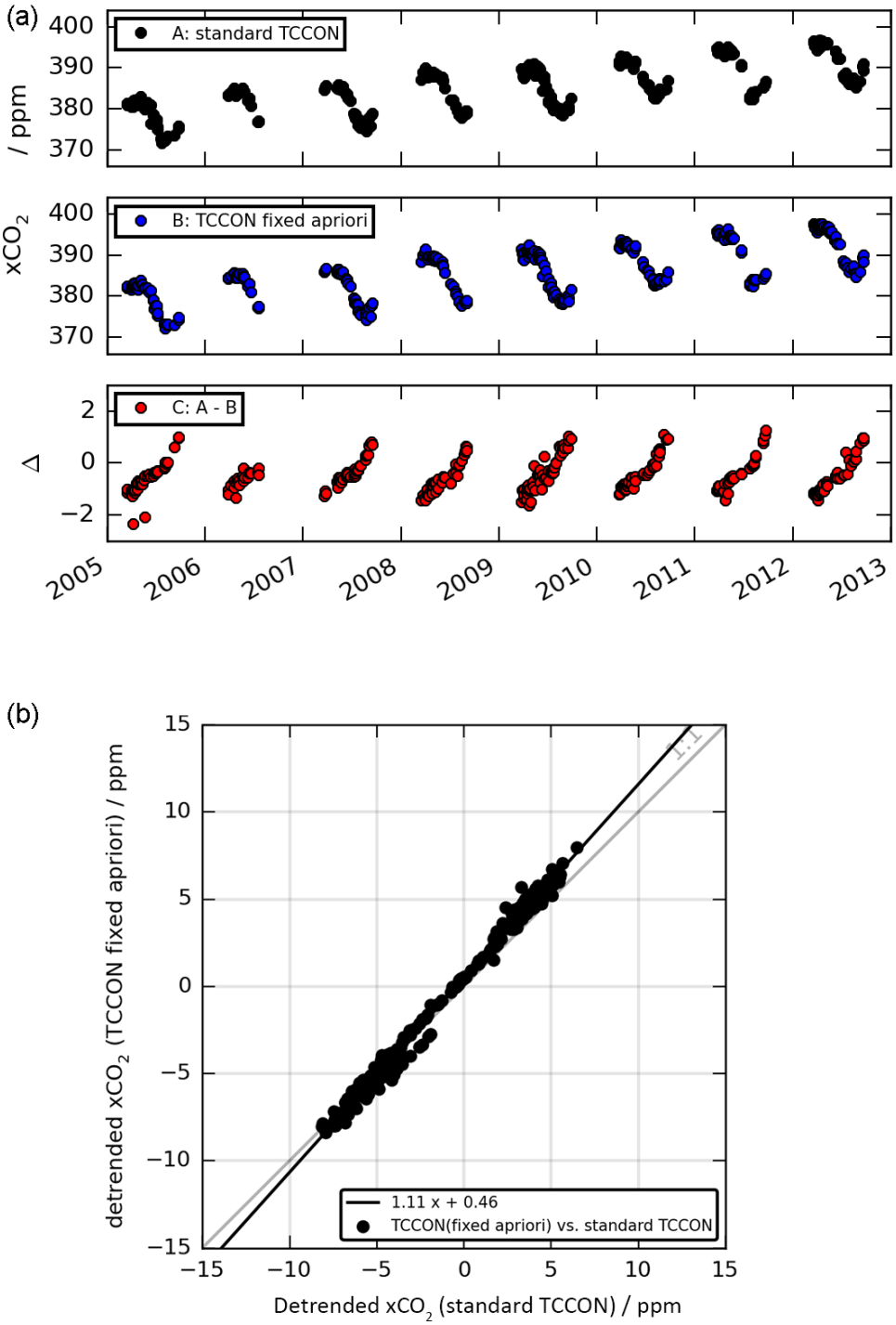

Figure 3.3.: **(a)** xCO_2 from the TCCON standard window for retrievals using the TCCON (upper panel) and fixed (center panel) a priori and their difference (lower panel). **(b)** The corresponding correlation plot of the detrended xCO_2 time series of the TCCON standard window, with modeled and fixed a priori. *Published as Fig. 3 in Buschmann et al. [2016].*

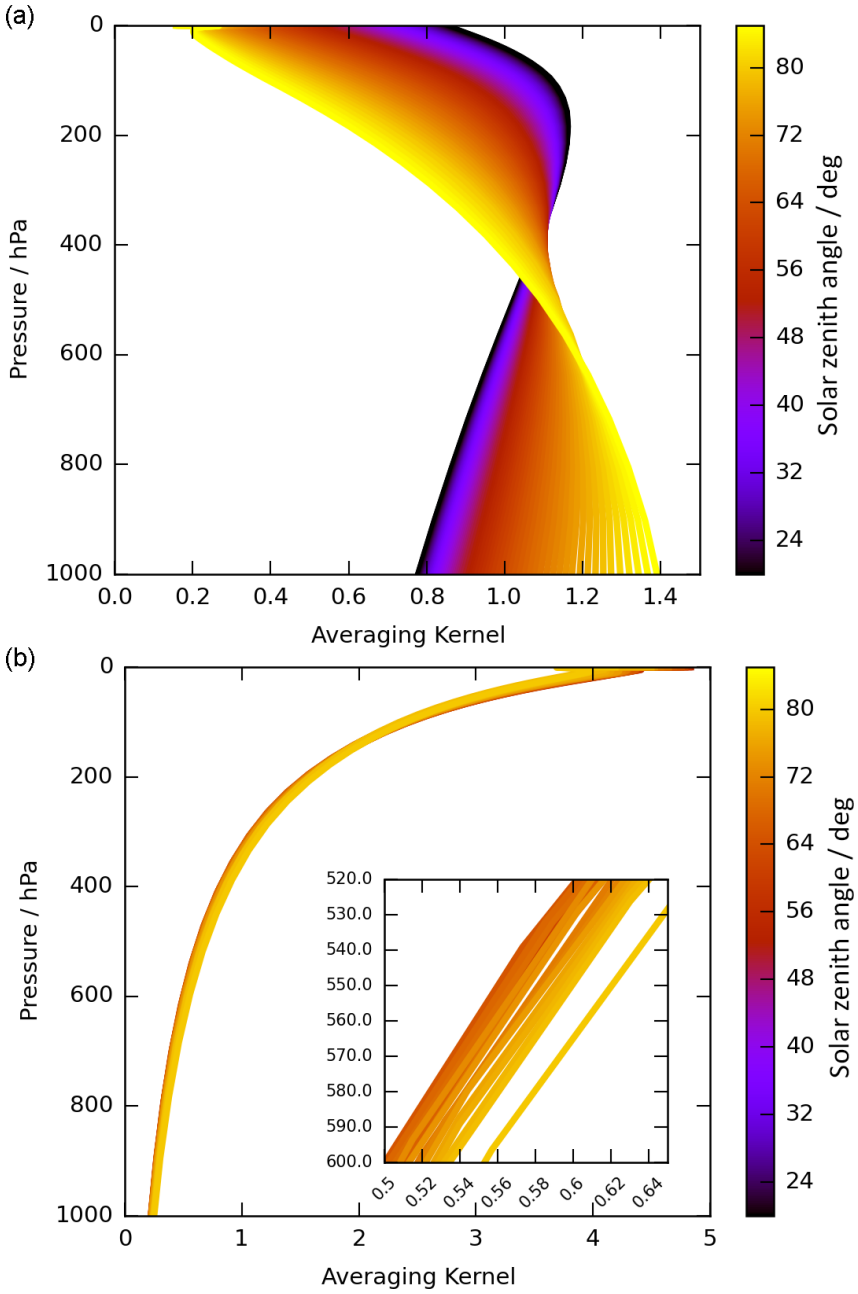

Figure 3.4.: Left: the total column averaging kernels from the TCCON retrievals. The official averaging kernels from the Lamont site, linearly interpolated to obtain intermediate profiles. Note the minimal possible solar zenith angle in Ny-Ålesund is 55°. Right: the total column averaging kernels from the 2626 cm^{-1} microwindow as an example NDACC averaging kernel. Note the high sensitivity in the stratosphere and low sensitivity in the troposphere in comparison to TCCON. *Published as Fig. 4 in Buschmann et al. [2016].*

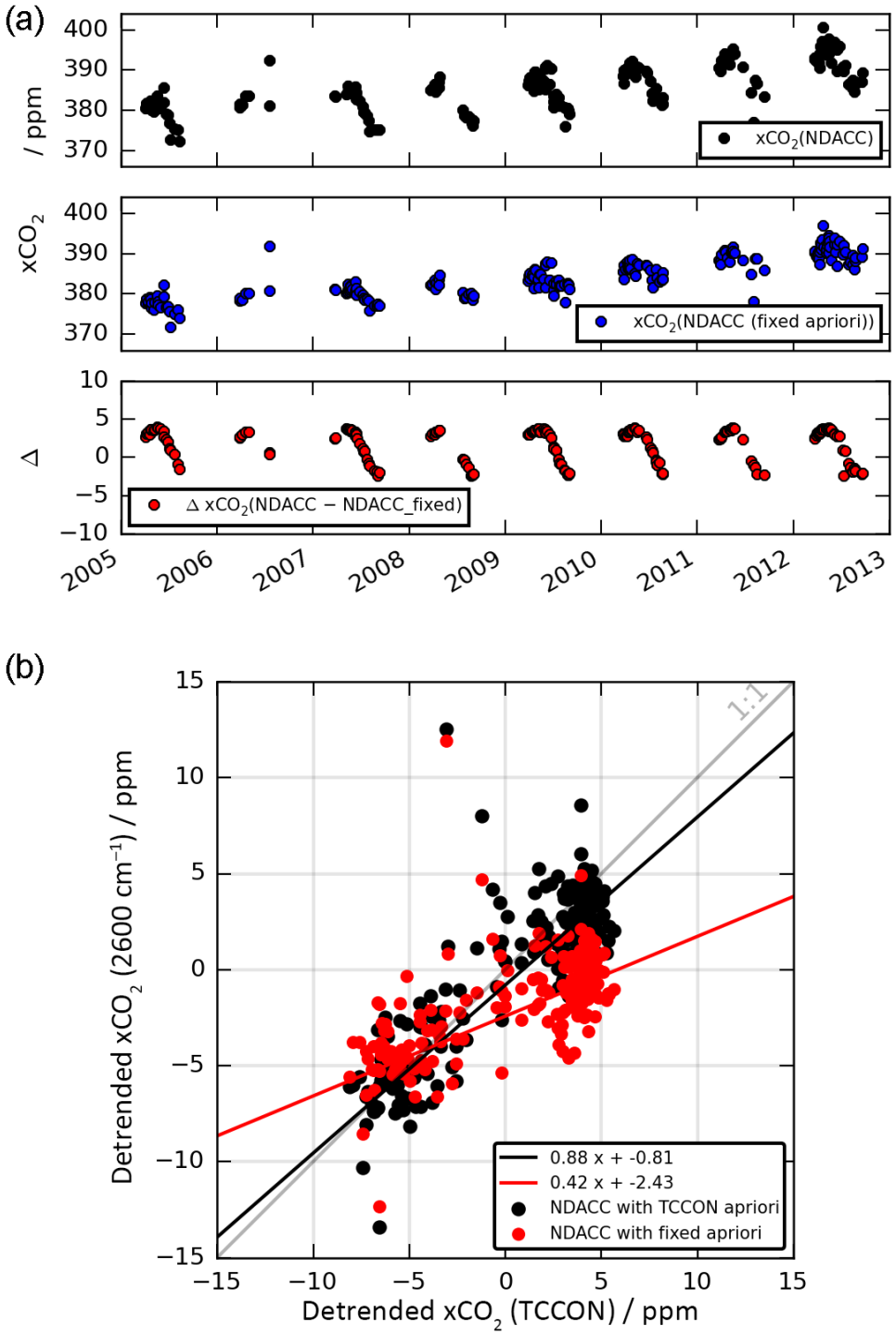

Figure 3.5.: **(a)** xCO_2 from the 2600 cm^{-1} NDACC spectra for retrievals using a modeled (upper panel) and fixed (center panel) a priori and their differences (lower panel). No residual secular trend is evident in the residuum. A clear seasonal pattern is visible, and thus a big part of the seasonal cycle is damped, when using a fixed a priori. **(b)** The corresponding correlation plot of the de-trended xCO_2 time series of TCCON vs. the NDACC retrievals with modeled and fixed a priori. *Published as Fig. 5 in Buschmann et al. [2016].*

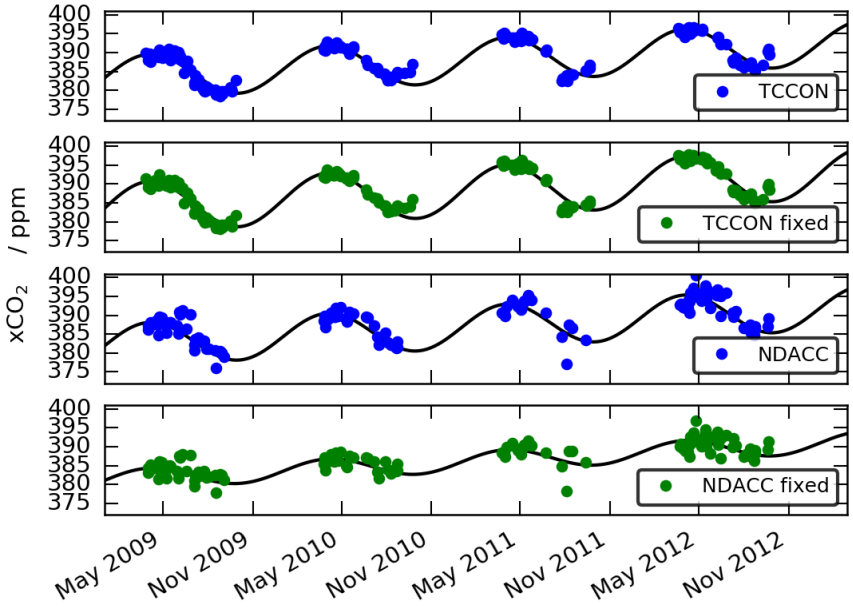

Figure 3.6.: Fits to the different retrievals. Top two panels: standard TCCON retrieval and TCCON retrieval with fixed a priori. Bottom two panels: NDACC with TCCON and fixed a priori. The fit parameters corresponding to Eq. (3.3) are presented in Table 3.3. For clarity, only a subset of the data from 2009 to 2013 is shown. *Published as Fig. 6 in Buschmann et al. [2016].*

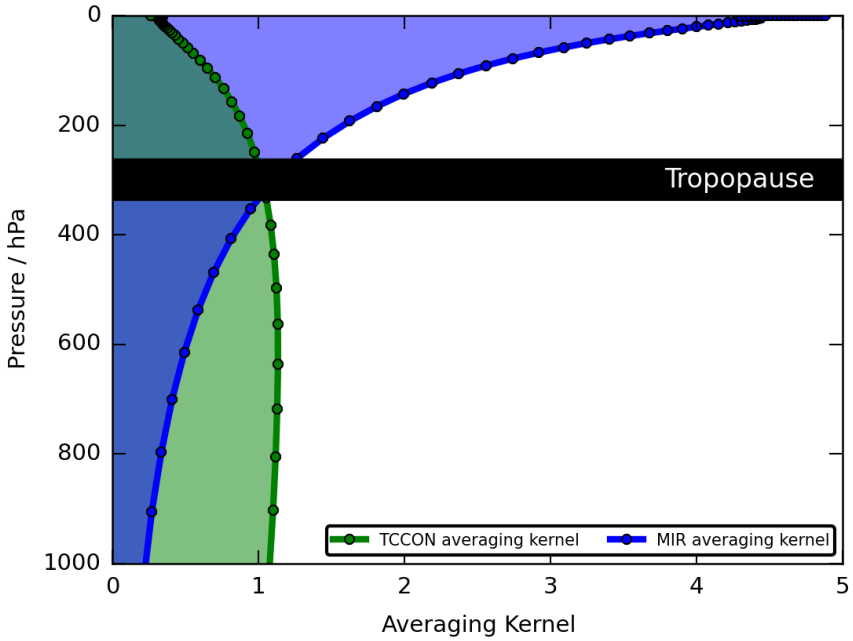

Figure 3.7.: Visualization of the tropospheric and stratospheric contribution of the MIR (blue) and TCCON (green) averaging kernels for an example solar zenith angle of 69°. *Published as Fig. 7 in Buschmann et al. [2016].*

3.4. Averaging kernel influence

This section was published as Sec. 4 in Buschmann et al. [2016]. References and citations have been updated.

In the last section, the influence of a varying a priori profile on the retrieval results was investigated. In the following the effect the different shape of the averaging kernels (given a common a priori) has on the retrieved xCO_2 is addressed. The differently shaped averaging kernels (see Fig. 3.4) must be taken into account in a direct comparison of the NDACC and TCCON xCO_2 products [Rodgers and Connor, 2003].

The general difference in the averaging kernel shape originates from the (compared to the NIR) narrow absorption lines in the MIR. Thus the NDACC xCO_2 averaging kernels show a higher sensitivity at lower atmospheric pressures.

We can use a common prior to quantify the differences between the two retrievals we expect to find for a given true atmospheric state. This is then an estimate of the averaging kernel smoothing error. Following the derivation in Sect. 4.3 in Rodgers and Connor [2003] and in Appendix A of Wunch et al. [2011b], two total column retrievals of a remote-sounding instrument can be compared by choosing a common a priori $\mathbf{x}_\mathrm{c}$ and a true atmospheric CO_2 profile $\mathbf{x}$. The difference of two retrieved total column amounts contributed by the different averaging kernels is then

$$c_\mathrm{corr} = \frac{1}{p_0} \sum_j \Delta p_j \left(\mathbf{a}^\mathrm{mir} - \mathbf{a}^\mathrm{nir}\right)_j (\mathbf{x} - \mathbf{x}_\mathrm{a})_j, \tag{3.4}$$

with the surface pressure represented by p_0, the column averaging kernels by $\mathbf{a}$, true profile by $\mathbf{x}$ and the common a priori by $\mathbf{x}_\mathrm{a}$. As the same a priori information is used in both the NDACC and TCCON retrievals, the common a priori $\mathbf{x}_\mathrm{a}$ is simply the TCCON a priori. The single elements are summed over the profile's pressure levels j, with Δp_j being the pressure difference between two levels. The NIR averaging kernels are mostly solar zenith angle dependent, and the Lamont averaging kernels interpolated to the respective zenith angles were used (as suggested by the TCCON database guidelines Wunch et al. [2015]).

Furthermore, this approach necessitates the knowledge of a true atmospheric profile of the target species ($\mathbf{x}$). As there are no independent measurements of the true atmospheric CO_2 profile with sufficient spatial and temporal coverage available, we use a model profile for this estimation.

As a true profile we chose a simulation from NOAA's CarbonTracker (CT2013) project [CarbonTracker; Peters et al., 2007], linearly interpolated to the site location and to the atmospheric pressure levels used in our retrieval. This allows for an estimation of the influence of the averaging kernel smoothing contribution between the two retrievals.

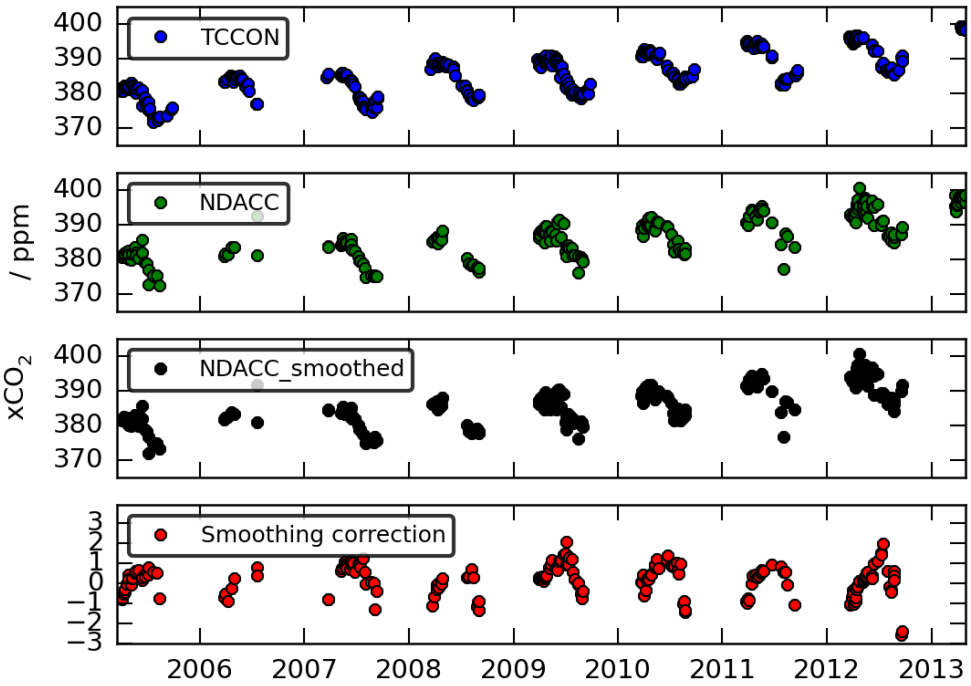

Figure 3.8.: An estimate of the magnitude of the averaging kernel smoothing correction as described in Eq. (3.4) for the Ny-Ålesund time series of the 2600 cm^{-1} windows with CarbonTracker 2013 as a true atmospheric profile. *Published as Fig. 8 in Buschmann et al. [2016].*

In Fig. 3.8, the averaging kernel correction for the Ny-Ålesund time series has been calculated (as shown above) for all data points. Afterwards the data from the different microwindows around 2600 cm^{-1} have been combined, and daily averages computed.

The residual in Fig. 3.8 shows a varying influence of the correction that is associated with the solar zenith angle of the measurements. The magnitude of the correction is solar zenith angle dependent and generally between 1 and -1 ppm. Results from the other microwindow regions show comparable behavior.

3.5. Lunar MIR xCH_4 retrieval

This section covers, in anticipation of chapter 4, the extension of the Ny-Ålesund CH_4 time series to include retrievals from MIR lunar absorption spectra. The intricacies of using the Moon as a light source are covered in detail in the next chapter.

Following the results from the previous sections in this chapter, the retrieval of xCO_2 from lunar spectra is not worth pursuing further, as already the xCO_2 retrieval from solar spectra is quite challenging and presents limited additional information on the carbon cycle.

Following the approach in the previous sections for the MIR xCO_2 retrieval an investigation of the a priori and averaging kernel properties is necessary to infer the suitability of the method. Sussmann et al. [2013] described the retrieval of MIR xCH_4 from NDACC MIR solar absorption spectra and compared them to TCCON measurements.

In the following a selection of microwindows suitable for the retrieval of xCH_4 is presented. Again, H_2O is retrieved in the same spectral region. Due to the absence of an atmospheric species with known abundance, the surface pressure is used (see section 2.3.7) to calculate the air mass factor as well.

Sussmann et al. [2013] used 3 microwindows (at $2614.55, 2835.65$ and $2921.30\,\mathrm{cm}^{-1}$) and the water vapour column was taken from the NCEP/NCAR reanalysis data. Sussmann et al. [2013] also investigated the impact of different a priori profiles. Here the standard TCCON a priori profiles are used. A total of 6 microwindows extending the microwindow selection used in Sussmann et al. [2013], are used. Five additional microwindows are used to retrieve H_2O. All microwindows used can be seen in Tab. 3.4, the interfering gases for each window are listed as well. The standard TCCON linelist (see Wunch et al. [2017a]) is used to retrieve the line parameters for the forward model.

center wavenumber	width	target gas	interfering species
2599.16	2.40	CH_4	N_2O, H_2O
2602.93	2.44	CH_4	N_2O, HDO
2614.55	1.7	CH_4	HDO, CO_2
2650.95	0.7	CH_4	HDO, CO_2
2835.65	0.3	CH_4	HDO
2921.30	0.6	CH_4	HDO, H_2O, NO_2
2819.85	0.70	H_2O	HCl, CH_4
2871.10	2.20	H_2O	CH_4, HDO
3001.20	0.65	H_2O	CH_4, O_3
3019.80	0.30	H_2O	–
3155.21	1.02	H_2O	CH_4

Table 3.4.: Microwindows used in the lunar MIR xCH_4 retrieval.

Additionally, in the MIR under low light conditions (like the moon), atmospheric emission becomes more prominent and as described in section 4.1 and appendix A.1, lunar emission can be neglected in the NIR, but becomes significant in the MIR to far infrared. However the retrieval approach is insensitive to broadband spectral features, especially when using micro windows, as the spectra are normalized to a window specific intensity base line. On the other hand, atmospheric emission and especially emission from room temperature optical components in the instrument can influence the retrieval.

Like before, the retrieval has been performed using the standard TCCON software suite GGG. The results of the retrieval and a comparison to the new lunar xCH_4 retrieval

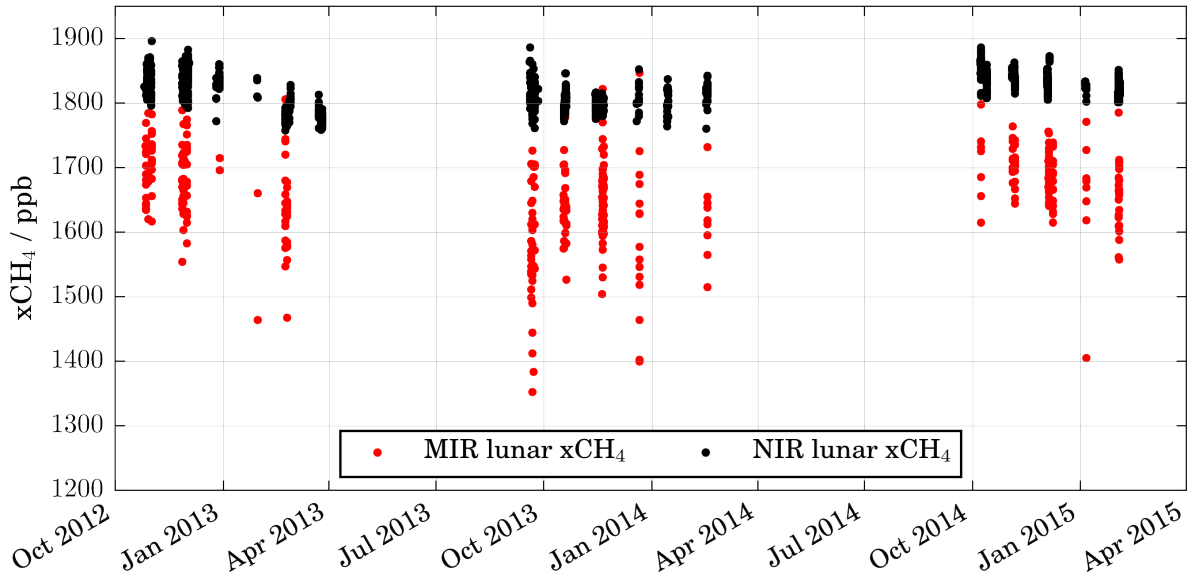

Figure 3.9.: Ny-Ålesund lunar xCH_4 retrieval from MIR spectra (red) compared to retrieval from lunar NIR spectra (black). Note that no smoothing correction was applied.

(see Chapter 4) are presented in Fig. 3.9. Here, the red dots show the results from the MIR lunar absorption spectra averaged over all microwindows (see Tab. 3.4). The two retrievals have not been made comparable by applying an averaging kernel smoothing correction. The only filter applied to the MIR time series was that the retrieval error has to be smaller than $1 \cdot 10^{19}$ molecules cm^{-2}. The results show a significant offset compared to the NIR retrievals, as well as a larger variability.

The offset can be explained by the shape of the averaging kernels, that similar to the MIR xCO_2 averaging kernels have a strong emphasis on the high atmosphere (compare xCO_2 averaging kernels in Fig. 3.4). This leads to an underestimation of the total CH_4 column, part of which would be compensated by applying an averaging kernel smoothing correction as shown in Sec. 3.4. Also, similar to the MIR xCO_2 case, Sussmann et al. [2013] show that the choice of the a priori has a strong influence on the retrieval. It can therefore be concluded that the lunar MIR spectra also have limited value to the extension of the xCH_4 time series.

3.6. Conclusion

In this chapter the trace gas retrieval of xCO_2 and xCH_4 from Ny-Ålesund middle-infrared spectra was investigated. From eight microwindows in NDACC MIR spectra vertical columns of CO_2 were retrieved using the profile scaling algorithm GFIT. Additionally,

absorption lines of N_2 were tested to be used for the calculation of the dry-air mole fraction. Due to their low line intensity, they did not yield reliable results and instead, the surface pressure was used.

The xCO_2 retrieval, using the standard TCCON a priori, resulted in a time series that was comparable to the TCCON reference. However, a more detailed analysis showed that the main reason of the agreement was the common a priori, which is already quite close to the true atmospheric profile. The repeated retrieval with a fixed a priori revealed that most of the previously seen seasonal cycle amplitude cannot be reproduced by the MIR retrieval. However, the retrieval was able to capture the secular increase of xCO_2.

The analysis of the MIR averaging kernels shows strong sensitivity in the stratosphere and low sensitivity in the troposphere. The smoothing error between the two retrievals (MIR and NIR) was estimated assuming the CarbonTracker model as a true profile. The resulting comparison showed, that the smoothing correction alone is not sufficient to compensate for the observed damped seasonal cycle. It can be concluded, that the profile scaling retrieval of MIR spectra does not provide additional information and therefore can not be used as a substitute for the NIR retrievals provided within TCCON.

Although the main focus of this work was on the xCO_2 retrieval, the MIR xCH_4 retrieval approach from Sussmann et al. [2013] was applied to the Ny-Ålesund NDACC spectra. Similar to the CO_2 study it can be concluded that the averaging kernel shape leads to a strong sensitivity to the chosen a priori. Therefore only a rudimentary comparison between the MIR and NIR xCH_4 retrievals was performed. However, in anticipation of the next chapter and the potential use of MIR spectra taken in the polar night with the Moon as a light source, xCH_4 was retrieved from lunar absorption spectra and compared to lunar NIR spectra, which will be introduced in the next chapter. The comparison of the time series with the standard TCCON a priori shows consistently lower xCH_4 values, which again is a result of the larger stratospheric sensitivity.

4. Extension of the CO_2 and CH_4 time series to the polar night

In this chapter, the second approach to extend the xCO_2 and xCH_4 time series will be presented. Solar absorption measurements are not possible in the arctic winter due to the polar night, when the Sun is permanently below the horizon (see 1.2).

During polar night, the Moon can be used as a light source above the atmosphere to perform lunar absorption measurements of atmospheric trace gases. This has been demonstrated repeatedly for measurements in the middle-infrared spectral region in Ny-Ålesund [Notholt and Lehmann, 2003; Notholt et al., 1993, 1997] and also in Arrival Heights, Antarctica [Wood et al., 2004].

The lower intensity of reflected sunlight off the lunar surface presents a challenge that is addressed by the introduction of a new thermo-electrically cooled InGaAs detector for measurements in the near-infrared spectral region. As has been shown in the previous chapter, MIR spectra are of limited use for the retrieval of trace gases like CO_2 and to lesser extent also CH_4.

In this chapter, first moonlight as a light source in the NIR will be investigated. Then the technical description of the new InGaAs detector and its performance is discussed, before presenting first proof-of-concept measurements in Bremen. These show the need for further optimization of the measurement setup. Consequently, the various options to improve the spectral signal-to-noise ratio, like lowering the resolution and increase of the measurements integration time are discussed. Additionally, potential issues when using lunar spectra are presented. The influence of scattered sunlight in the atmosphere, the usage of more appropriate atmospheric models during the night and disk-averaged solar lines are discussed. These result in a set of filter conditions applied to the raw retrieved data.

Afterwards, the focus lies on the newly retrieved Ny-Ålesund time series of xCO_2 and xCH_4. Section 4.5 describes the validation process of the lunar retrieval by comparing solar and lunar measurements on consecutive nights. Then, the time series' are compared to various reanalysis models and to in-situ measurements.

Parts of this chapter have been published in Buschmann et al. [2017a] and selected sections have been copied from the publication.

4.1. Lunar irradiance

Lunar irradiance analysed by an observer on Earth is a composite of two distinct light sources: reflected sunlight and thermal emission from the illuminated (and therefore heated) lunar surface. The absolute intensity of moonlight does not influence the retrieval of atmospheric trace gases by FTIR absorption spectroscopy as the intensity of the broadband transmission curve is used as a fit parameter in the retrieval. The order of magnitude of the expected intensity can be estimated by a simple calculation (see Appendix A.1) to be $3.4 \cdot 10^{-3} \frac{W}{m^2}$.

The total amount of irradiance estimated here, however, does not include a spectral distribution. To consider the different intensities in different spectral regions, the Planck curves for different black body radiators can be compared. The radiometric flux as a function of black body temperature and wavenumber (σ) is given for example in Davis et al. [2001]:

$$B(\sigma) = 2hc\sigma^3 \frac{1}{\exp \frac{hc\sigma}{k_B T} - 1} \tag{4.1}$$

The resulting plot (Fig. 4.1) shows this as function of wavenumber $\tilde{\nu}$ and different temperatures. The black body temperature of the solar photosphere is assumed to be $5700K$ and that of the illuminated lunar surface to be $335K$ Matthews [2008].

As can be seen in Fig. 4.1, the thermal lunar emission can be neglected in the NIR spectral region. Therefore, the irradiance of the reflected sunlight can be compared by the direct solar irradiance at the Earth's top-of-atmosphere (TOA) value of 1361 Wm^{-2} (used in Matthews [2008]. Assuming an average broadband lunar albedo of 13.6 % (see Matthews [2008]), a factor of about $2.9 \cdot 10^6$ can be calculated, meaning direct sunlight has an intensity about six order of magnitude stronger than moonlight. For this rough estimate other effects originating in orbit parameters, geometry or composition of the lunar surface are not considered. A comprehensive analysis of the lunar spectral irradiance, and the development of a model describing it, was performed by Kieffer and Stone [2005] for the RObotic Lunar Observatory (ROLO).

The visibility of the Moon at an observation site on Earth depends on its position and orientation on its orbit around the Earth. The illumination of the Moon (as seen from Earth) - the lunar phase - changes from full illumination (full Moon) to almost no illumination (new moon) within two weeks. An example of the illuminated lunar disk simulated by the *Stellarium* virtual planetarium [Stellarium, 2015] as seen from Ny-Ålesund around the full Moon on February 4 2015 is shown in Fig. 4.2.

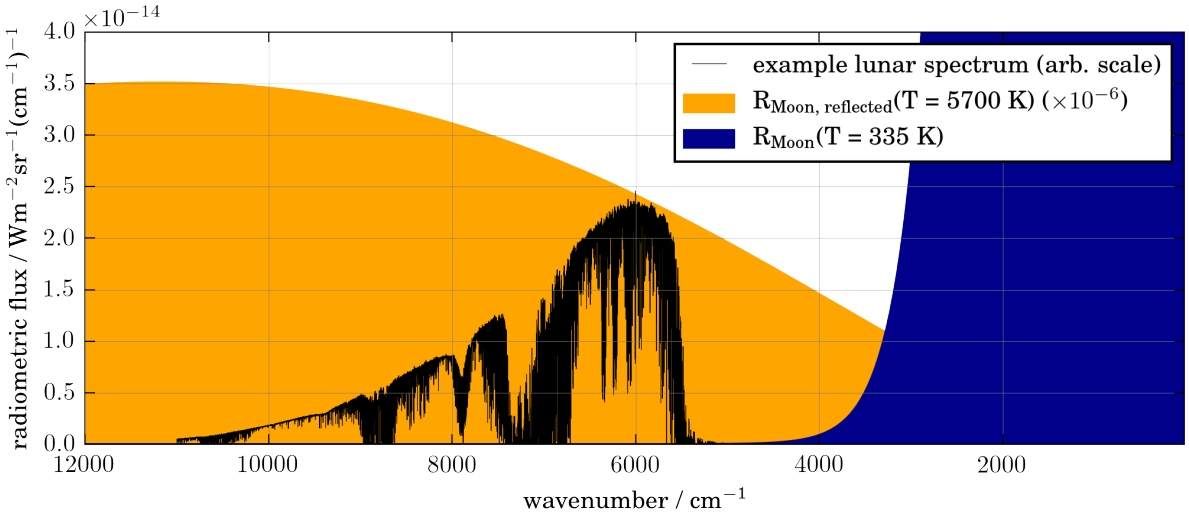

Figure 4.1.: The estimated irradiance from the reflected sunlight (orange) and thermal lunar emission (blue) including an averaged example spectrum taken by the Ny-Ålesund FTIR instrument on Feb 2 2015. Note that the FTIR spectrum is not calibrated and the shape of the envelope depends on instrumental properties, e.g. beam splitter, mirror absorption and detector sensitivity.

The terrain surrounding the observatory in Ny-Ålesund is characterised by a mountain range in the south and the open fjord in the north-east. The closest mountain (Mount Zeppelin) obstructs the line of sight for higher zenith angle solar and lunar measurements. In order to quantify this effect the Svalbard digital elevation model (DEM) provided by the [Norwegian Polar Institute] with a resolution 20 m can be used to derive a horizon line as seen from the observatory. The derivation and results are presented in Appendix A.6.

The total number of potential measurement hours can be calculating by excluding all times, where the lunar elevation is below the horizon height. Additionally, lunar phases with insufficient illumination ($> 85\%$) and times where the Sun is above $-5°$ elevation have to be excluded. The lunar positions are calculated using the Python module *PyEphem* which is based on the JPL ephemeris [PyEphem, 2015]. Using the above information, the sum of possible measurement times can be calculated. Depending on lunar orbital parameters the maximum number of measurement hours in this projects time frame ranges from about $1751h$ in 2012 to $1316h$ in 2016. The visibility due to clear sky conditions is, of course, not included in this estimate.

Figure 4.2.: An illustration of the lunar phases around the full Moon from 2015-01-30 to 2015-02-08 each at 00:00 local time. The individual images are screenshots from the *Stellarium* simulation software Stellarium [2015].

4.2. The thermo-electrically cooled InGaAs detector

As discussed in section 4.1, reflected sunlight from the lunar surface has an intensity six order of magnitude lower than direct sunlight. The standard InGaAs detector used for measurements in the TCCON setup is rated to have a maximum noise-equivalent power (NEP) of about $2 \cdot 10^{-12}$ $\frac{\mathrm{W}}{\sqrt{\mathrm{Hz}}}$ (see Tab. 4.1). This value gives the power of the incident light needed to produce a signal with the same strength as the inherent detector noise, which means a lower NEP value gives a better signal-to-noise ratio for a fixed amount of incident light.

Recently, a new class of InGaAs detectors was used in an FTS to measure reflected sunlight off the Earths surface from a mountain-top site to investigate the spatial distribution of trace gases in the Los Angeles basin [Fu et al., 2014; Wong et al., 2015]. In their setup a thermo-electrically (TE) cooled InGaAs detector was used to compensate for the intensity loss when using reflected sunlight. In this class of diodes, the active area is mounted directly to a Peltier-element (TE-cooling element) within the diode housing.

	50% Cutoff [μm]	Peak D* min (typ) [$\frac{\mathrm{cm}\sqrt{\mathrm{Hz}}}{\mathrm{W}}$]	NEP [$\frac{\mathrm{W}}{\sqrt{\mathrm{Hz}}}$]
TCCON equivalent diode	2.60	4.2E+10 (5.9E+10)	2.1E-12 (1.5E-12)
TE cooled InGaAs 1.7μm	1.62	5.0E+13 (9.9E+13)	1.8E-15 (8.9E-16)
TE cooled InGaAs 1.9μm	1.83	9.9E+12 (1.4E+13)	9.0E-15 (6.3E-15)

Table 4.1.: Sensitivity parameters of different versions of used InGaAs detectors Teledyne Judson Datasheet [2003].

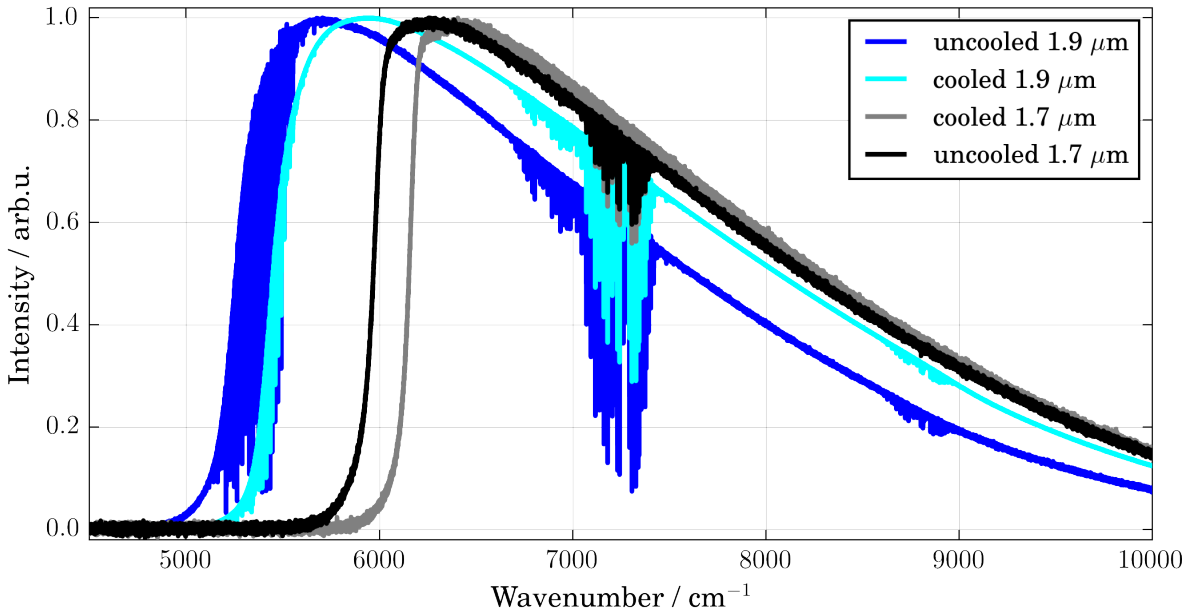

Figure 4.3.: Example lamp spectra for the two different TE cooled diodes used in the detector (see Table 4.1). For each diode a cooled and uncooled spectrum is shown.

In this study a similar, TE-cooled InGaAs detector has been purchased from Bruker after consultation with the JPL group[1]. Generally, any InGaAs detector can be manufactured in variants with differing cut-on wavenumbers. The doped semiconductor material exhibits different band-gaps and therefore different sensitivity ranges in the infrared, that are dependent on the composition of the In-Ga-As-ratios. A standard InGaAs diode has a cutoff wavelength of around 1.7 µm (corresponding to 5882 cm^{-1}). Diodes with increased cut-off wavelength are available until the lattice mismatch of the compositions crystal structure becomes unstable. The TCCON detector is equipped by default with an extended range InGaAs diode with a cut-off wavelength of about 2.6 cm^{-1}. It has to be noted, that the change in cut-off wavelength also changes the diodes sensitivity.

The detector delivered by Bruker had a cut-off wavelength of about 1.7 µm, which would be high enough to measure the absorption lines of CO_2, CH_4 and O_2 in the NIR region between 5800 – 8000 cm^{-1}. However, the cooling of the diode by the two-stage Peltier-element (see inlet in Fig. 4.4) results in thermal stress to the diodes crystal structure. This then results in a shift of the cut-off wavelength. Unfortunately, this means that the absorption lines of CH_4 and part of the CO_2 band is not resolvable any more, if the diode is cooled. A substitute diode with a slightly extended range (cut-off wavelength of 1.9 µm) was bought and installed in the detector. For a comparison of the diode parameters see Tab. 4.1 and for a comparison of lamp spectra of the two diodes under both, cooled and uncooled conditions can be seen in Fig. 4.3.

[1]Stanley P. Sanders, Jet Propulsion Laboratory, California Institute of Technology, private communication

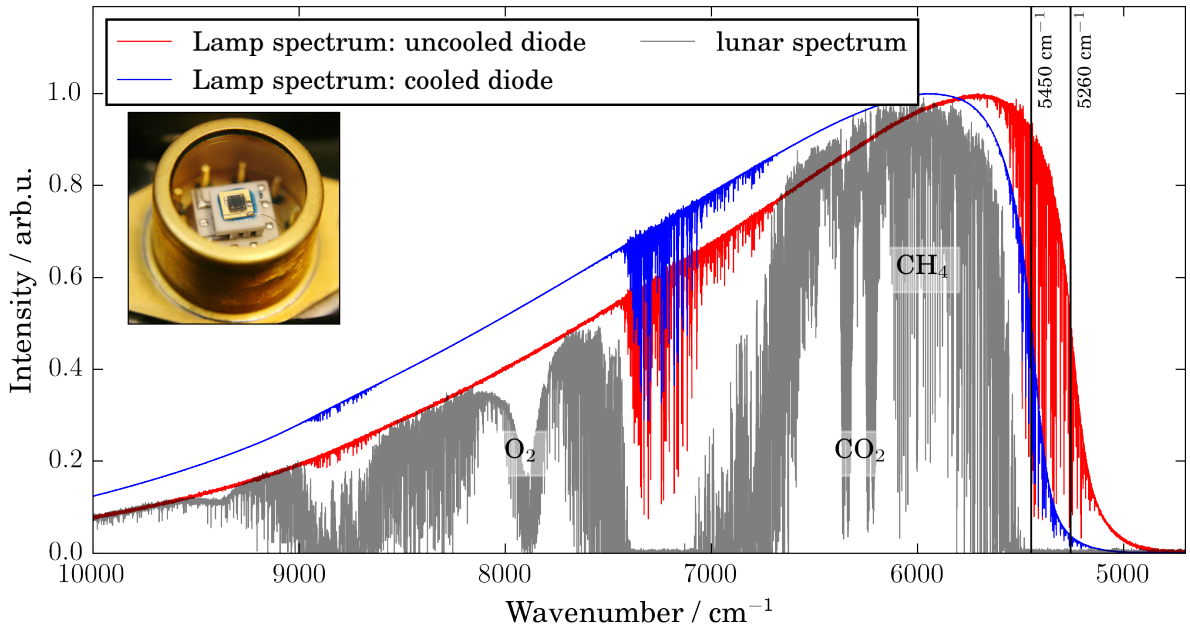

Figure 4.4.: Example measurements of the InGaAs diode: Cooled (blue) and uncooled (red) lamp spectra. Note the indication of the cut-on wavenumbers. An averaged lunar spectrum is shown in gray and a picture of the diode was added. *Published as Fig. 1 in Buschmann et al. [2017a].*

The diode is thermally connected to the detector housing which is equipped with solid aluminium cooling fins. As the FTS in Bremen and Ny-Ålesund are not evacuated and are constantly purged with dry-air, a sufficient transport of excess heat can be assumed. The power supply for the TE-cooling unit is connected to the detector via a separate voltage stabilizer. It should be noted that the detector housing (as delivered) had to be modified to fit the TE-cooling power connector while mounted in a Bruker 125HR FTS by repositioning the socket to the back of the housing.

For the first performance tests of the new detector in Bremen, an external power supply was used for the TE-cooling. However, the connection out of the FTS into a regular wall socket introduced electrical noise. For the final deployment of the new detector in the Ny-Ålesund FTS, an internal, auxiliary power supply on the stepper motor control can bus board was used and then no electrical noise was visible.

In order to achieve the same signal-to-noise ratio from lunar and solar absorption measurements with the same measurement parameters, the detector has to be six orders of magnitude more sensitive. The NEP increase of a TCCON extended InGaAs diode to the new TE cooled 1.9 µm diode is about three orders of magnitude. Therefore changes to the experimental setup are required to further increase the signal-to-noise ratio of the measured spectra.

4.3. Proof of concept and first light of the new detector in Bremen

The new InGaAs detector equipped with the extended range diode as described in the previous section was employed for first tests in the Bremen FTS. The new detector was first deployed to Ny-Ålesund in the autumn of 2012 for the 2012/2013 polar night. Before that, it was tested and the previously mentioned technical issues resolved by testing the detector in the Bremen FTS. At several full moon periods between 2012 and 2014, the detector was additionally brought back from Ny-Ålesund in summer to perform further tests in Bremen. Unlike Ny-Ålesund, Bremen offers the possibility of solar measurements during the day and lunar measurements during the night year-round. The proof-of-concept for the usage of the new detector for lunar NIR measurements was published in Buschmann et al. [2015]. The publication was part of a joint book publication of all participants of the Earth System Science Research School (ESSReS). The results have since been re-processed using the 2014 version of GGG.

The low intensity of the reflected sunlight requires further changes to the experimental setup. Part of the continued measurements in Bremen was to test varying parameters like spectral resolution, integration time and aperture size and their effect on the retrieved quantities. Additionally, the retrieval code (GGG) was tested with the newly recorded lunar spectra. In the absence of independent, co-located and simultaneous xCO_2 and xCH_4 measurements, solar absorption measurements are the obvious choice to investigate the performance of the lunar absorption measurements. In Fig. 4.5 a example time series shows measurements of xCO_2, xCH_4 and xO_2 for four days just before the July 2013 full moon. In this case, two time series are presented, one where the DMF is calculated via the O_2 ratio and the other via the surface pressure (see Sec. 2.3.7). The lunar measurements clearly show a larger scatter. The increased scatter is a result of the low signal-to-noise ratio of the spectra. The large offset between pressure and O_2 derived DMFs is a result of the known errors in the O_2 spectroscopy, which are corrected for during TCCON post processing. At times close to sunrise or sunset a sharp increase in the pressure derived DMFs can be observed. This is caused by an undefined light path and further investigated in Section 4.4.3. Experimental parameters have been changed during this time series and a proper comparison of solar and lunar retrievals will be presented later with data from Ny-Ålesund in Chapter 4.5.

The first measurements with the Bremen FTS show that the signal-to-noise ratio of the spectra must be further increased to reduce the scatter in the lunar data. The different possibilities for improvement will be discussed in the following section. Additionally, it should be noted that the gold plated solar tracker mirrors in Bremen were more degraded than the ones in Ny-Ålesund. An additional increase in signal intensity was observed, when measuring with the Ny-Ålesund FTS.

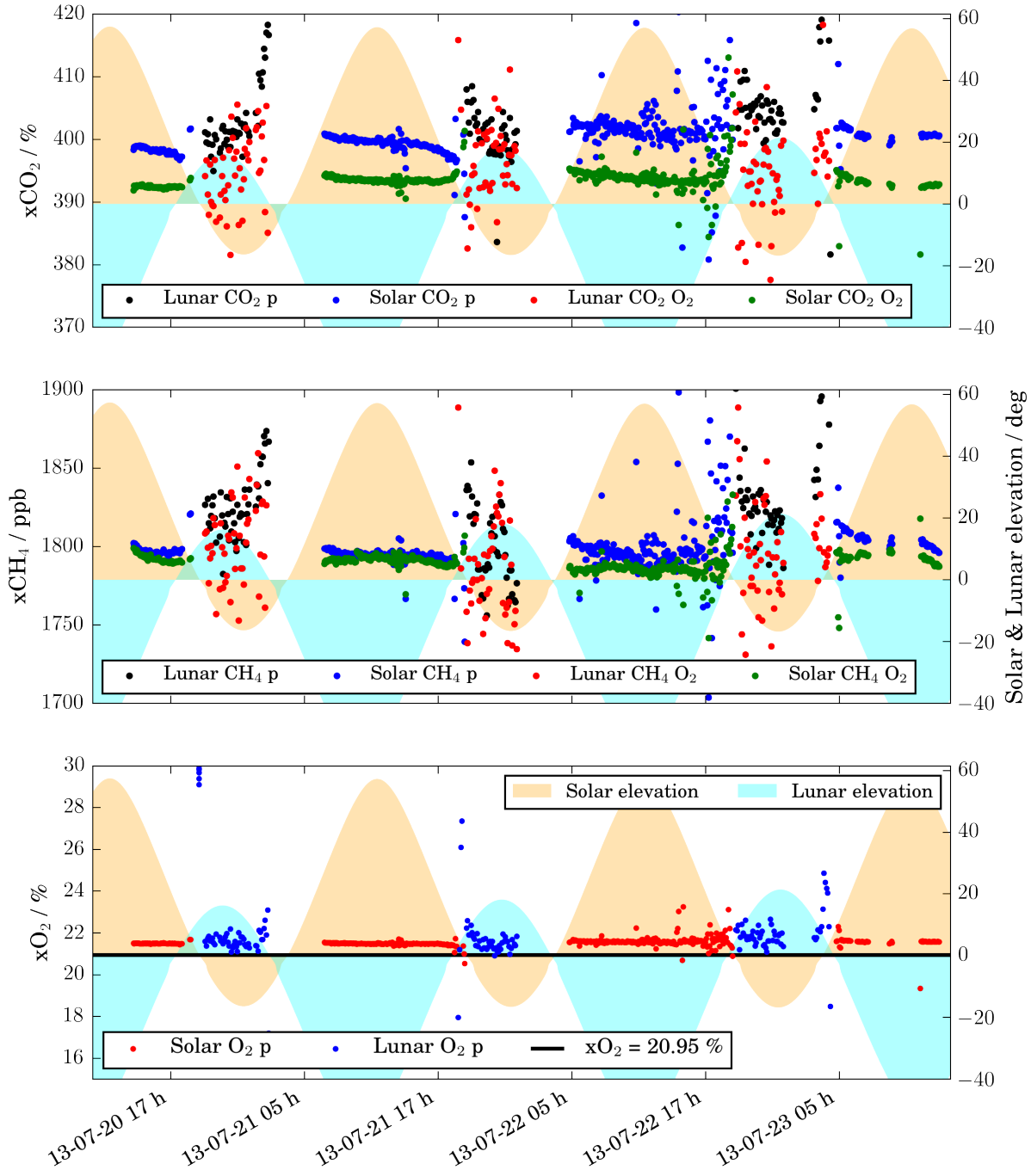

Figure 4.5.: Unfiltered, retrieved of xCO_2, xCH_4 and xO_2 from Lunar NIR spectra (red) compared to retrieval from Solar NIR spectra (green). The black and blue dots show the corresponding surface pressure retrieval. The solar and lunar elevation angles have been added on the right axes for the shaded areas.

4.4. Optimisation of measurement parameters and retrieval method

4.4.1. The effect of spectral resolution and noise on the retrieval

This section was published as Sec. 3.4 in Buschmann et al. [2017a]. References and citations have been updated.

The resolution used in the TCCON is better than 0.02 cm^{-1}, corresponding to a maximum optical path difference (OPD) of 45 cm. Initial tests showed that even with the cooled detector, the spectral signal-to-noise ratio did not allow for a robust retrieval unless a lot of spectra were averaged; however, the path of moonlight through the atmosphere changes rapidly with time. Although this is more prominent in lower latitudes, it still must be considered here, especially at large lunar zenith angles. To avoid bias from inaccurate knowledge of the viewing geometry, the integration time per measurement must be as small as possible.

One option to decrease the measurement time is to increase the velocity of the instrument's scanning mirror; however, this has no effect on the spectral signal-to-noise ratio. The scanner velocity was therefore not changed and kept at 10 kHz to minimise potential differences from the solar absorption measurements. The second option is to decrease the spectral resolution, which increases the spectral signal-to-noise ratio. Additionally, it allows for shorter measurement times and thus for more spectra to be averaged within the same time, resulting again in an increased signal-to-noise ratio.

The influence of resolution on the retrieval can be analysed in further detail and to circumvent differences arising from a varying atmospheric state. Previously, Petri et al. [2012] investigated this for the TCCON standard retrieval windows. Here the analysis was repeated with emphasis on lower resolutions (down to 1.0 cm^{-1}) and additionally spectra with different signal-to-noise ratios were used. A set of 60 consecutive solar spectra has been selected and the interferograms cropped at lengths corresponding to a range of maximum optical path differences between 45 cm (0.02 cm^{-1}) and 0.9 cm (1.0 cm^{-1}). The interferograms were reprocessed and the spectra calculated with the i2s program within the GGG2014 program suite.

In addition to this series of spectra, different magnitudes of white noise were added to the created spectra to simulate the effect of the lower signal-to-noise ratio expected in lunar spectra. The signal-to-noise-ratios are calculated from the reprocessed spectra by dividing the maximum mean signal between absorption lines at about 6000 cm^{-1} by the root mean square of a blacked out region of the spectrum. Figure 4.6 shows the results of

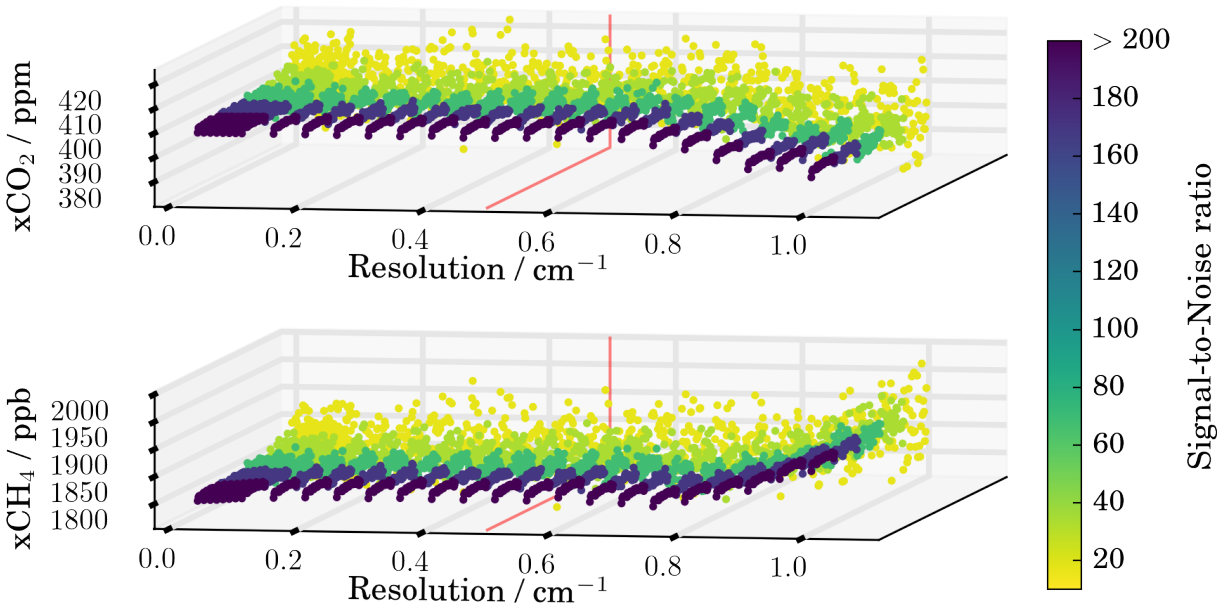

Figure 4.6.: Retrieved xCO_2 and xCH_4 from cropped interferograms with different resolutions and different levels of white noise (z-axis and colorbar) added to the spectra. *Published as Fig. 5 in Buschmann et al. [2017a].*

the standard retrieval of xCO_2 and xCH_4 for the various combinations of resolution and signal-to-noise ratio of the series.

The decrease in resolution leads to an increase in S/N. Fig. 4.7 shows the increase in S/N measured as a function of spectral resolution with a Bruker 125 HR, normalized to the SNR at $0.02\,\mathrm{cm}^{-1}$, i.e. a spectrum recorded with $1.0\,\mathrm{cm}^{-1}$ resolution has a 10 times larger S/N (see blue line). Additionally, the shorter scan length allows to record more spectra in the same time frame. Averaging leads to an increase in S/N by a factor of $\sqrt{N}$ with N measurements (red line). The combination of both effects (black line) shows the potential increase in S/N with resolution for a fixed integration time. A lower resolution would potentially also allow for a larger entrance aperture. However, at lower resolutions the size of the entrance aperture is limited by the size of the image of the lunar disk, rather than the resolution.

For better visibility, Fig. 4.8 shows a subset of the data from Fig. 4.6, showing the mean retrieved xCO_2 and xCH_4 DMFs at a given resolution. Two series have been selected, with high (red) and low (black) signal-to-noise ratios. The associated errors can be estimated by the standard deviation (1σ) of the arithmetic mean and do not change much with resolution for a given S/N. The mean errors and their standard deviation for xCO_2 are 4.0 ± 0.6 ppm for the low S/N case (black dots in Fig. 4.8) compared to 0.6 ± 0.05 ppm for the high S/N case (red dots). Similarly the errors for CH_4 are 18.5 ± 3.2 ppb (low S/N, black dots) and 2.9 ± 0.3 ppb (high S/N, red dots).

A distinct cut-off above 0.7 cm^{-1} can be identified in the xCO_2. For higher resolutions, i.e. $0.02 - 0.7$ cm^{-1}, no significant difference is visible in high signal-to-noise conditions.

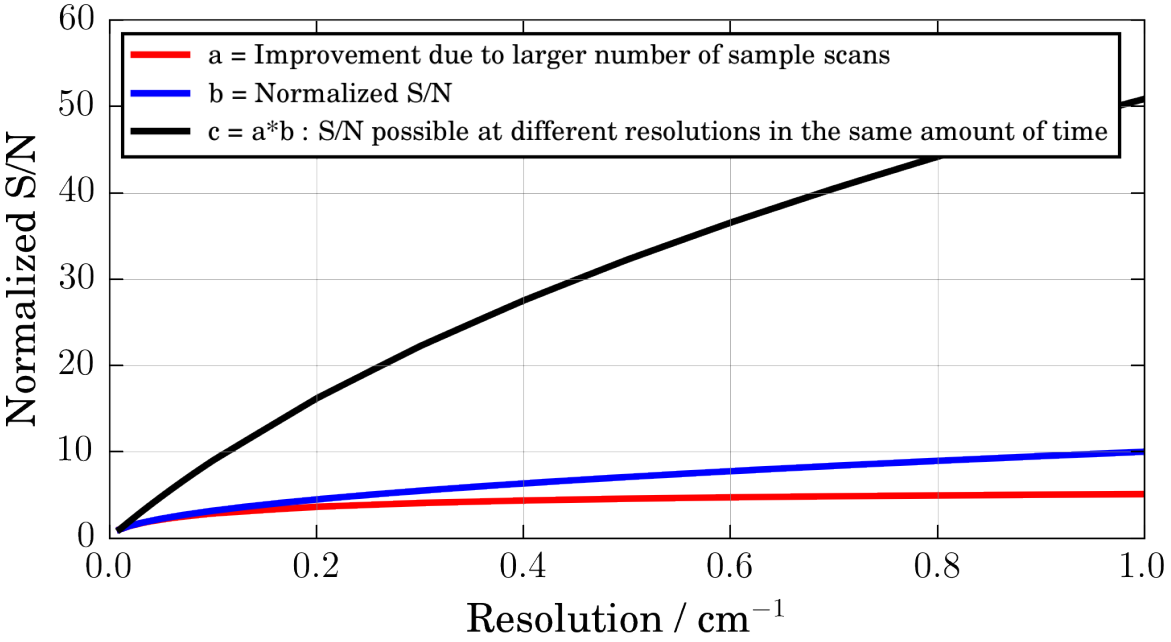

Figure 4.7.: Spectral signal-to-noise ratio as a function of resolution. The improvement due to lower resolution (blue line) and averaging over larger number of spectra in the same time frame (red line) and the resulting relative S/N from both effects (black line), normalised to the S/N at 0.02 cm^{-1}. *Published as Fig. 6 in Buschmann et al. [2017a].*

In general, a lower signal-to-noise ratio of the spectra leads to increased scatter of the retrieved DMFs, but to no significant bias. Table 4.2 shows the bias in the retrieved DMFs of high and low signal-to-noise ratio spectra for the two resolutions used in the measurement setup later.

S/N	Resolution [cm^{-1}]	ΔxCO$_2$ [%]	ΔxCH$_4$ [%]
> 300	0.08	0.03 $\pm$ 0.57	0.28 $\pm$ 2.61
	0.5	0.07 $\pm$ 0.65	0.76 $\pm$ 3.03
≈ 30	0.08	-0.13 $\pm$ 4.12	0.00 $\pm$ 15.03
	0.5	-0.20 $\pm$ 4.50	0.79 $\pm$ 22.89

Table 4.2.: Comparison of the biases, introduced by lower resolution measurements and low signal-to-noise ratio. Subset of data points from Fig. 4.8. *Published as Tab. 1 in Buschmann et al. [2017a].*

Gisi et al. [2012] showed that lower resolution solar spectra can be used to retrieve DMFs with a low resolution FTS (Bruker EM27/SUN). Recently Hedelius et al. [2016] investigated errors and biases from a 0.5 cm^{-1} FTS (Bruker EM27) for TCCON relevant species. The three studies [Gisi et al., 2012; Hedelius et al., 2016; Petri et al., 2012] report different biases in xCO$_2$ when changing the resolution to 0.5 cm^{-1} in the range from -0.12 % % to 0.13 %. For xCH$_4$, Hedelius et al. [2016] reported an increase of 0.28 % when decreasing

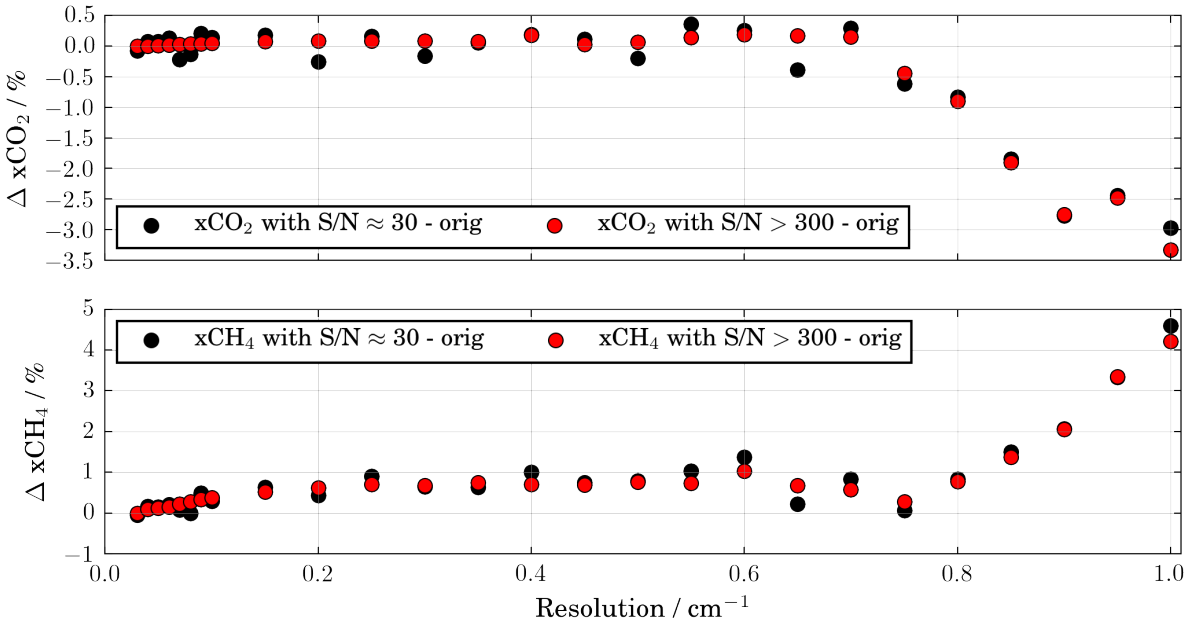

Figure 4.8.: Mean of the retrieved xCO_2 and xCH_4 from cropped interferograms at different resolutions with low and high signal-to-noise ratio. Shown is the relative difference to the highest signal-to-noise ratio and highest resolution. *Published as Fig. 7 in Buschmann et al. [2017a].*

the the resolution to 0.49 cm^{-1}. In our analysis (see Tab. 4.2) a consistent decrease in mean ΔxCO_2 and ΔxCH_4, i.e. the difference between DMFs from low and high resolution spectra, is observed when moving to lower resolutions. However, when considering the assigned errors (1σ standard deviation) this is not significant, especially under lower signal-to-noise conditions.

For the final decision on the best resolution for low S/N conditions the possible number of recorded spectra per time interval has to be considered. This number does not increase linearly, due to instrumental effects, i.e. the deceleration of the moving mirror and the time needed for data acquisition and storage. The first measurements were taken at a reasonably high spectral resolution of 0.08 cm^{-1} (OPD = 11.25 cm). The measurement setup was adjusted after further tests. The benefit of a better signal-to-noise ratio on the measurement precision lead to finally decreasing the resolution to 0.5 cm^{-1} (OPD = 1.8 cm) and all measurements from 2015 onwards were taken with a resolution of 0.5 cm^{-1}.

The effect of different resolutions on the retrieved columns can also be investigated by comparing different measurements taken consecutively with different resolutions. Figure 4.9 shows lunar absorption measurements of the target species on October 7 2014. The first and third batch of measurements were taken with a resolution of 0.085 cm^{-1} (OPD = 10.59 cm), the second batch was measured with 0.5 cm^{-1} (OPD = 1.8 cm) resolution. No significant bias is observed. Decreasing the spectral resolution also changes the infor-

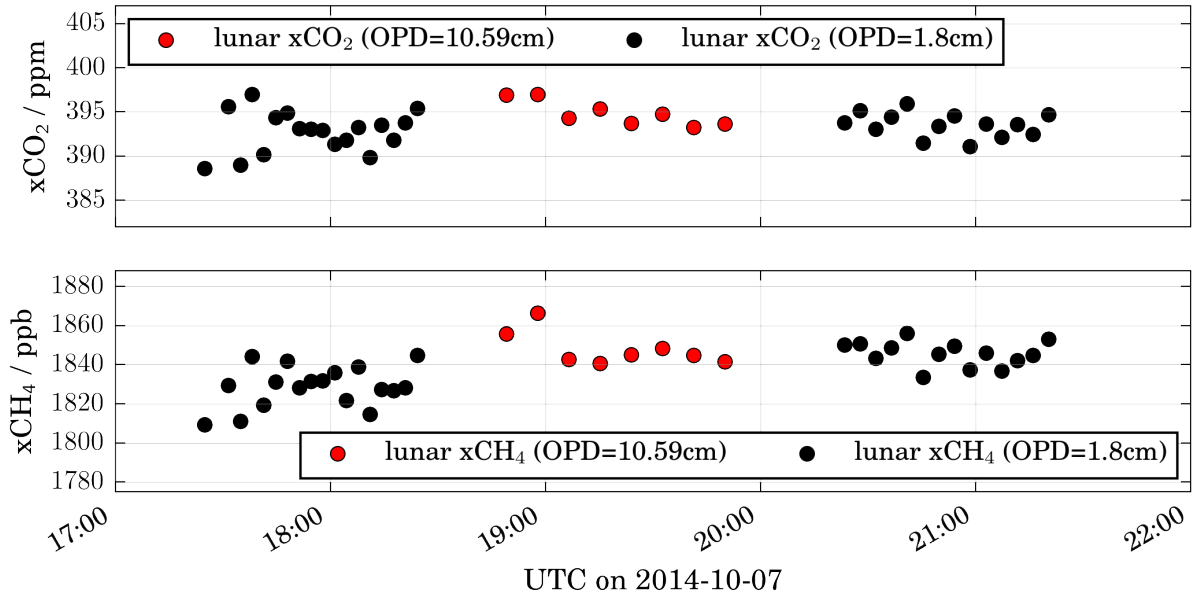

Figure 4.9.: Comparison of retrieved xCO_2 and xCH_4 for different resolutions from low (OPD = 1.8 cm$\widehat{=}$0.5 cm^{-1}, black) and higher (OPD = 10.59 cm$\widehat{=}$0.085 cm^{-1}, red) resolution measurements on 2014-10-07. *Published as Fig. 8 in Buschmann et al. [2017a].*

mation content of the recorded spectral lines. This results in a change in shape of the measurements averaging kernels and is discussed below.

4.4.2. Airmass factor

The light path through the atmosphere is quantified by the concept of airmass. For a given zenith angle α, a ray of light passing through the atmosphere has a certain length. The airmass is defined as the ratio between this thickness of the atmosphere at $\alpha = 0$ and the thickness along the line-of-sight. By definition, a zenith-viewing ($\alpha = 0$) instrument has an airmass of 1. The higher the zenith angle α, i.e. the ray passing through the atmosphere closer to the horizon, has a larger airmass, with a maximum at a zenith angle of $\alpha = 90°$.

When tracking the Sun or the Moon along their trajectory, the zenith angle changes during the course of a measurement. In the TCCON setup the FTS performs two consecutive scans, one on the way to maximum optical path difference and a reversed scan on the way back to the starting position of the movable mirror. This leads to an integration time of under 2 minutes per scan and the change in airmass during one scan is typically neglected.

For the lunar measurements multiple scans (up to 40) with lower resolution are taken. The FTS is again set to measure 2 scans (forward and backward) per mirror movement cycle, like before. However, the additional scans are stacked ontop of each other and averaged to increase the signal-to-noise ratio. All consecutive (e.g. forward) scans are therefore measured at a different zenith angle and the averaged interferogram contains information from multiple airmasses.

Figure 4.10 shows the changing airmass over the course of one day. As an example the airmass of the spectra taken on 2013-07-22 (see Fig. 4.5) were taken. GFIT calculates the airmass via the ratio of the line-of-sight-column and the vertical column and the resulting airmass coefficient is provided by the standard software output. The top panel in Fig. 4.10 shows the airmass provided by GFIT for the O_2 column (black dots) and two models for the calculation of the airmass. The simplest approach is to consider a flat, non-spherical Earth and atmosphere. The resulting airmass is then simply described by the inverse of the cosine of the zenith angle. Of course, this approach is not suitable for higher zenith angles. Therefore an empirical model by Kasten and Young [1989] is used, which represents the airmass adequately for this analysis:

$$A(\beta) = \frac{1}{\sin(\beta) + 0.50572(6.07995 + \beta)^{-1.6364})} \tag{4.2}$$

for an airmass A as a function of the elevation angle $\beta = 90° - \alpha$ (see Fig. 4.10). In reality, the dispersive characteristics of the atmosphere result in a frequency dependent airmass, which is captured by the ray tracing calculations within GFIT for the actual retrieval. However, these effects are small and this simple model allows for the change in

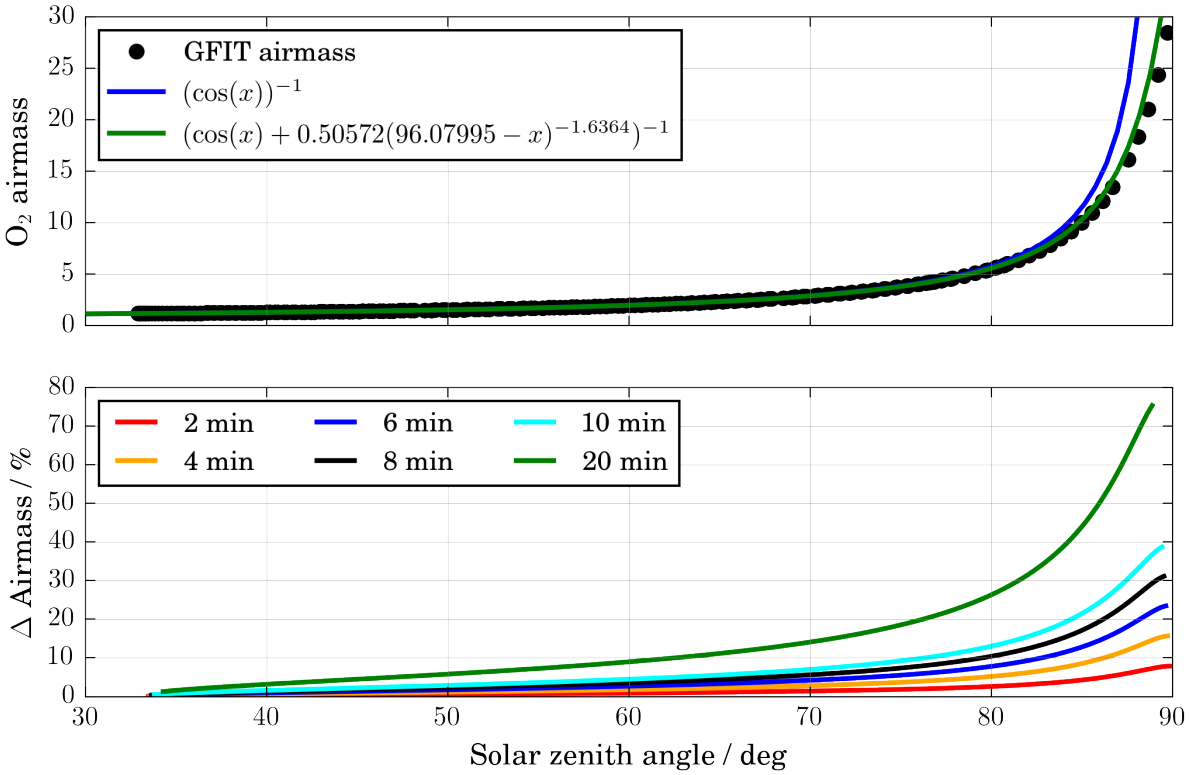

Figure 4.10.: The impact of the measurement time on the airmass. Top panel shows measured airmass (black dots) from 2012-07-22 in Bremen and the simple secant and an extended model of the zenith angle (blue and green line). The lower panel shows the change in airmass from the beginning to the end of a measurement for different integration times.

airmass within a given time to be easily calculated. The lower panel in Fig. 4.10 shows the results, when using the solar zenith angle on 2012-07-22 as a basis. The y-axis shows the difference in airmass at the beginning of a potential measurement and the one at the end of the measurement: $(A(\alpha_i) - A(\alpha_j))/A(\alpha)$ for a zenith angle α and beginning (α_i) and end (α_j) angles.

Accurate knowledge of the airmass is necessary for the retrieval, because the forward model uses the calculated light path through the atmosphere to create the artificial spectrum for the retrieval process (see Sec. 2.3). To an extent this can be mitigated by the O_2-ratio approach (see Sec. 2.3.7). Additionally, an incorrectly assumed airmass leads to non-matching line shapes of the spectroscopic measured and theoretical lines.

At high zenith angles the analysis shows an difference of up to 40 % for a 10 min integration time. At $\alpha = 85°$ for a 10 min measurement, the difference in airmass is just under 20 %. It is therefore advisable to limit the integration time as much as possible, especially in case of high zenith angle situations. An additional argument for a short integration time is the decreased possibility of cloud obstruction during one measurement.

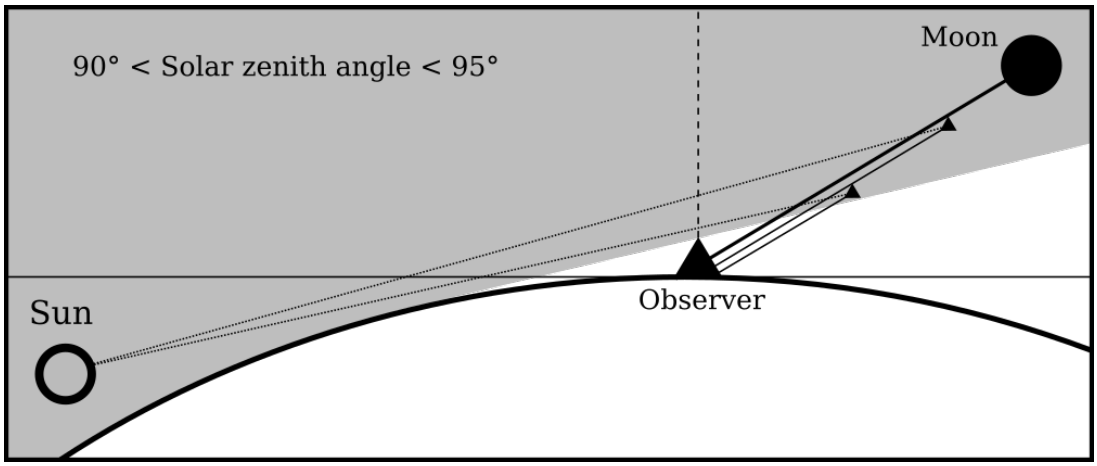

Figure 4.11.: Diagram highlighting the light path through the atmosphere at high Solar zenith angles. Parts of the observer – Moon light path are illuminated by the Sun, even if the Sun is below the horizon.

4.4.3. The influence of backscattered sunlight

The path of the photons through the atmosphere needs to be clearly defined to retrieve an accurate airmass to calculate the DMFs. If the target species is relatively uniformly distributed, uncertainties in the light path geometry cancel out, when using the O_2 ratio approach to calculate the DMFs. In case of sunlight the effect of stray light is negligible, due to its high intensity relative to any scattered light source under clear sky conditions.

In case of moonlight, scattered sunlight in the Earth's atmosphere needs to be considered. If the sun is above or shortly below the horizon, objects (e.g. aerosols) in the observer – Moon light path potentially scatter sun light to the observer. An illustration of the Sun – Moon – observer illumination geometry is presented in Fig. 4.11.

date	xCO_2	xCH_4	LZA	SZA
2013-09-22 16:37	437.84	1988.72	84.20	88.30
2013-09-23 05:31	435.69	1958.34	68.36	88.50
mean (SZA> 95°)	395.74	1804.36		

Table 4.3.: The DMFs of CO_2 (im ppm) and CH_4 (im ppb) retrieved using the surface pressure compared to the nightly mean, where the Sun was below $-5°$ elevation. Values for lunar and solar zenith angle are also given.

The presence of this kind of scattering leads to an overestimation of the DMF if only the observer – Moon light path is considered in the retrieval of the airmass factor. Fig. 4.12 shows the retrieved xCO_2 from lunar spectra on one particular night in September 2013. The dots show xCO_2, when the airmass is calculated via the surface pressure, as described in 2.3.7 and the blue markers show the xCO_2 retrieved via the O_2-ratio approach.

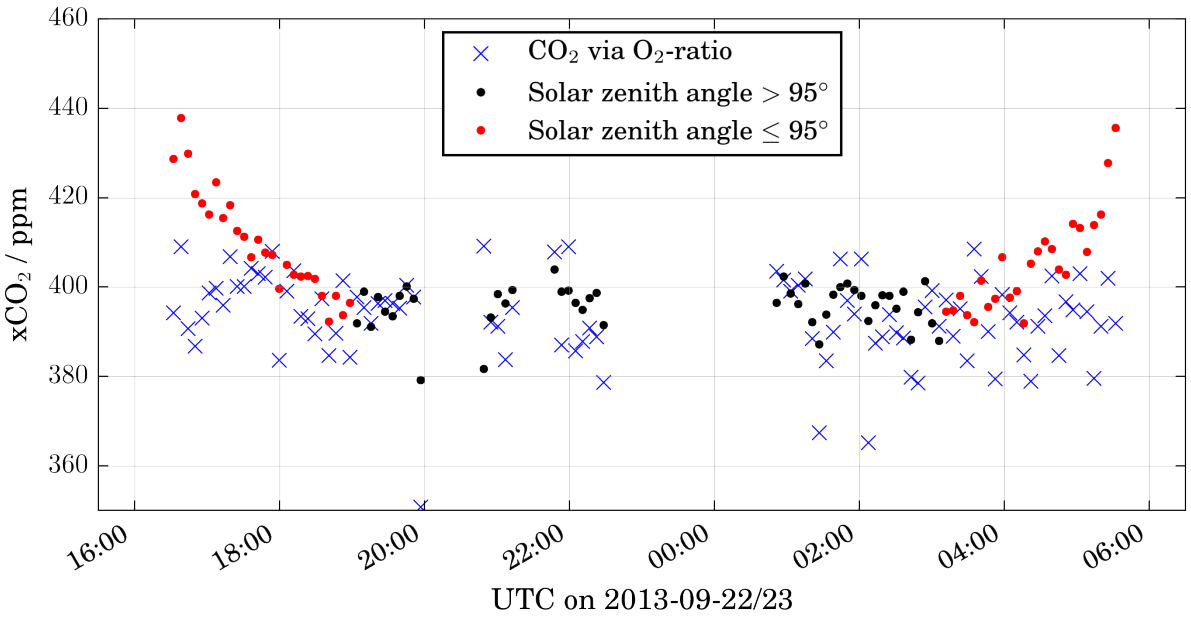

Figure 4.12.: Time series of xCO_2 on 2013-09-22/23. Shown are the retrieved lunar xCO_2 values with a corresponding solar zenith angle of smaller (red) and larger (black) than 95°. Blue markers show the same retrieval using the O_2-ratio approach.

The surface pressure retrieved values are color-coded to highlight the solar zenith angle (SZA) at the time of the measurement. It can be clearly seen, that the DMF of CO_2 increases if the solar zenith angle is smaller than 95°. In Tab. 4.3 two measurements where selected and the DMFs of CO_2 and CH_4 are presented alongside the solar and lunar zenith angles. In these particular measurements xCO_2 shows an increase of about 40 ppm compared to the mean of all measurements during that night, where the solar zenith angle is smaller than 95°. For CH_4 an increase of up to 180 ppb respectively. In both cases this corresponds to an inrease of about 10 %.

Due to the antisymmetric relationship of solar and lunar zenith angle (LZA) around full Moon this could also be indicative of a lunar zenith angle dependence of the retrieval. This can be investigated by plotting a large number of data points (to get a larger sample size) from the time series against the lunar zenith angle. Again the measurements are color coded to highlight measurements, where the solar zenith angle is smaller than 95°. Figure 4.13 shows an increase in the DMF of both CO_2 and CH_4, independent of lunar zenith angle, when the solar zenith angle is smaller than 95°. As a result, all lunar measurements with a corresponding solar zenith angle $< 95°$ will be discarded (compare Sec. 4.4.6).

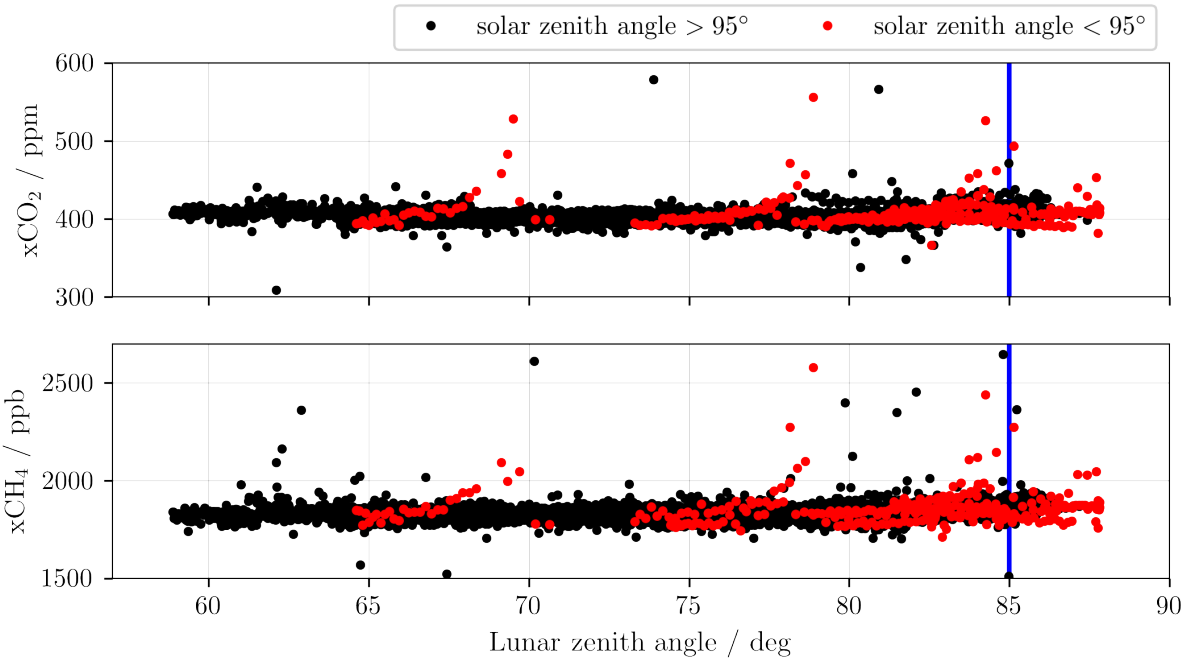

Figure 4.13.: Effect of backscattered sunlight on lunar retrieval. Highlighted (in red) are all lunar xCO_2 and xCH_4 values with a corresponding solar zenith angle smaller than 95°.

4.4.4. Adjustment of the atmospheric model

This section was published as Sec. 3.3 in Buschmann et al. [2017a]. References and citations have been updated.

Information on the target gas is retrieved from the processed spectra by the least-square fitting algorithm GFIT (see Sec. 2.3.7). The software assumes an a priori profile of the target gas and calculates an artificial spectrum given additional information on the atmospheric profile. In TCCON the interpolation of the NCEP/NCAR reanalysis data [NCEPNCAR, 2016] to the sites latitude, longitude and local noon is used as an atmospheric model, resulting in one model profile per day. The NCEP/NCAR reanalysis data is publicly available and was provided via `http://www.esrl.noaa.gov/psd/` [NCEPNCAR, 2016]. In case of lunar measurements, this presents a potential problem around midnight, as consecutive measurements would use different atmospheric models, i.e. the one interpolated to local noon.

Given that the reanalysis data are available in six hour time intervals, we use the model profile interpolated to the site coordinates and the time of measurement, resulting in specific model profiles for each measurement. These profiles presumably better reflect the atmospheric conditions, especially at night. The increased computational effort for this per-spectrum-model approach is affordable for this comparatively small time series.

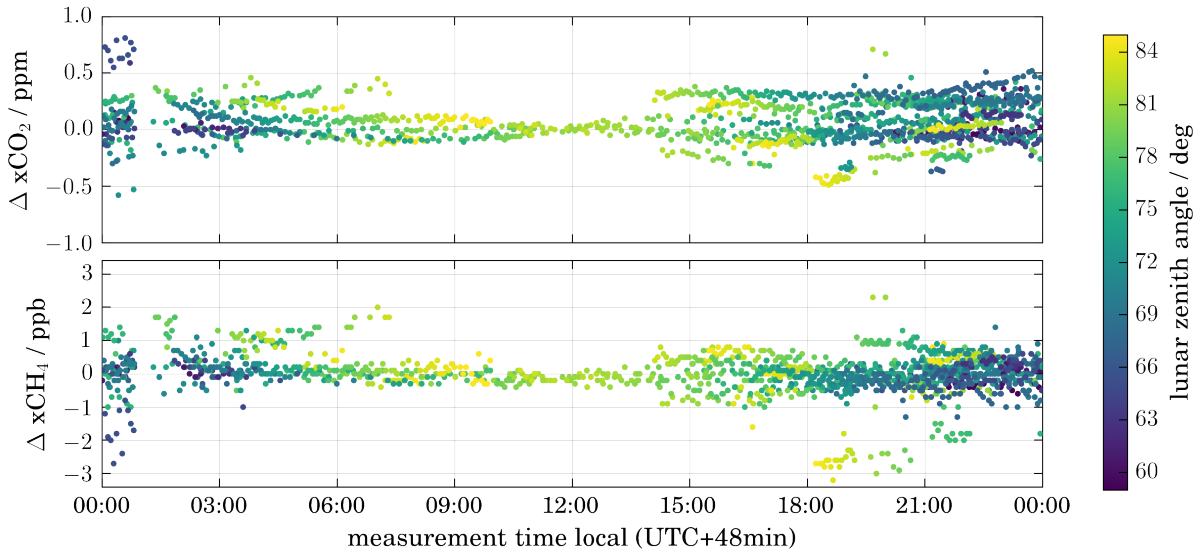

Figure 4.14.: Differences in the lunar absorption retrieval results (2012 – 2015) using the site and time of measurement interpolated atmospheric model compared to using the model interpolated to site and local noon for both target species dependent on the lunar zenith angle. *Published as Fig. 3 in Buschmann et al. [2017a].*

A comparison of the differences in retrieved xCO_2 and xCH_4 between the daily and spectrum-specific model profiles is shown in Fig. 4.14 for the lunar time series and for selected days in the TCCON time series in Fig. 4.15. The two retrievals show minimal differences at local noon (as they should), but differences of about ± 0.5 ppm (CO_2) and about ± 2 ppb (CH_4) can occur later in the day, under quickly varying atmospheric conditions distant in time from local noon. Note that the measurements showing potentially large deviations are typically filtered out within TCCON as they occur at high solar zenith angles.

4.4.5. Solar lines

In the Sun, hydrogen is transformed into helium in a high temperature plasma under great gravitational pressure via nuclear fusion. The process emits large amounts of energy and therefore electromagnetic radiation, which eventually exits the sun. Apart from H and He, the sun also contains trace amounts of heavier elements which are also present in the solar corona. These atomic species absorb part of the radiation emitted by the sun and are visible as absorption lines in any solar spectrum. These so called Fraunhofer-lines are therefore also present in solar spectra recorded with ground-based instruments.

These narrow Fraunhofer-lines are subject to Doppler shift, depending on the parallel velocity component of the atoms along the line-of-sight. Due to the solar rotation around

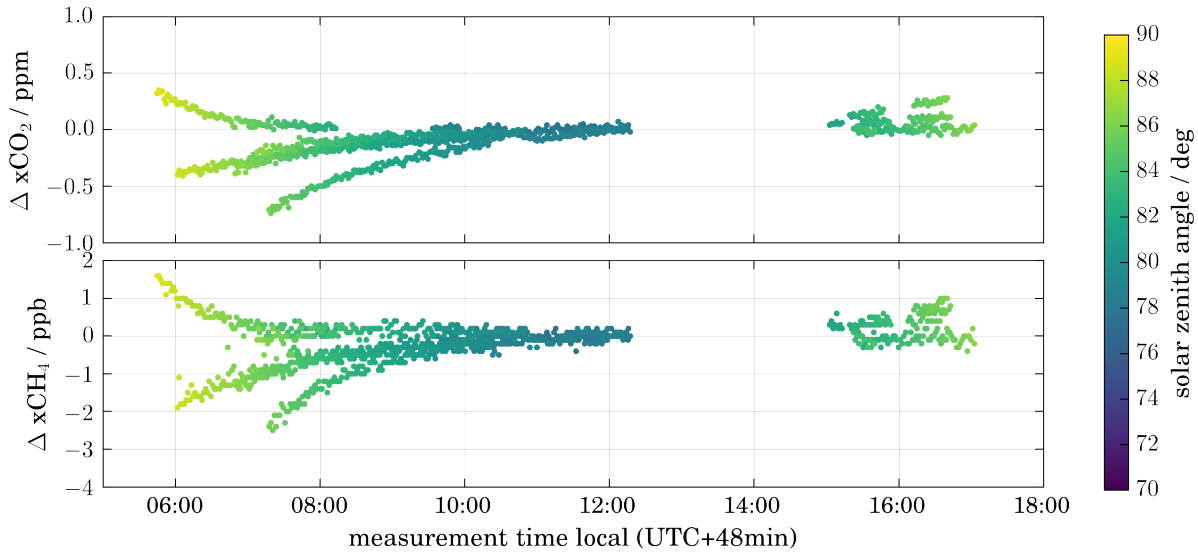

Figure 4.15.: Same as Fig. 4.14 but for TCCON solar absorption measurements for the time between 2013-09-19 and 2013-09-24. Note the generally higher differences at high zenith angles. Between 12:30 and 15:00 local time the sun moves behind a mountain at lower zenith angles. *Published as Fig. 4 in Buschmann et al. [2017a].*

its axis, at any time, part of the solar disk is moving towards the Earth and the opposite side away from it. Similarly, an earthbound observer is moving towards and away from the Sun, depending on the time of day. This leads to varying solar line positions when targeting a specific area on the solar disk. In case of direct sunlight spectra used in TCCON, this is circumvented by focusing the small aperture to the center of the solar disk (where the parallel velocity component is minimal).

When using reflected sunlight from the Moon, however, a disk-integrated solar line shape needs to be assumed to optimally represent the Fraunhofer lines in the simulated spectrum used in the retrieval. GFIT offers the option to automatically trigger the usage of disk-integrated solar lines, as long as the field of view chosen in the measurement setup is sufficiently large ($> 9.2\,\mathrm{mrad}$) or the Moon is chosen as the light source in the retrieval run parameters.

Additionally, the broadened, disk-averaged solar line positions are subject to additional Doppler shift, due to the movement of the Moon on its orbit around the Earth. Depending on the lunar phase, i.e. before or after full moon, the shift can be positive or negative. The solar line position is a fit parameter in the retrieval and thus free to adjust, which ensures correct attribution of the spectral lines in the retrieval. The example fits from a lunar absorption spectrum from 2015-10-25 in Fig. 4.16 show the calculated and measured spectra (blue and black lines) with the solar line contribution highlighted (yellow lines). The residuum, that is the difference between measured and calculated spectrum, shows

no visible signs of distortions specific to solar line positions. It can be concluded that the solar lines are correctly attributed in the retrieval of the target gases CO_2, CH_4 and O_2.

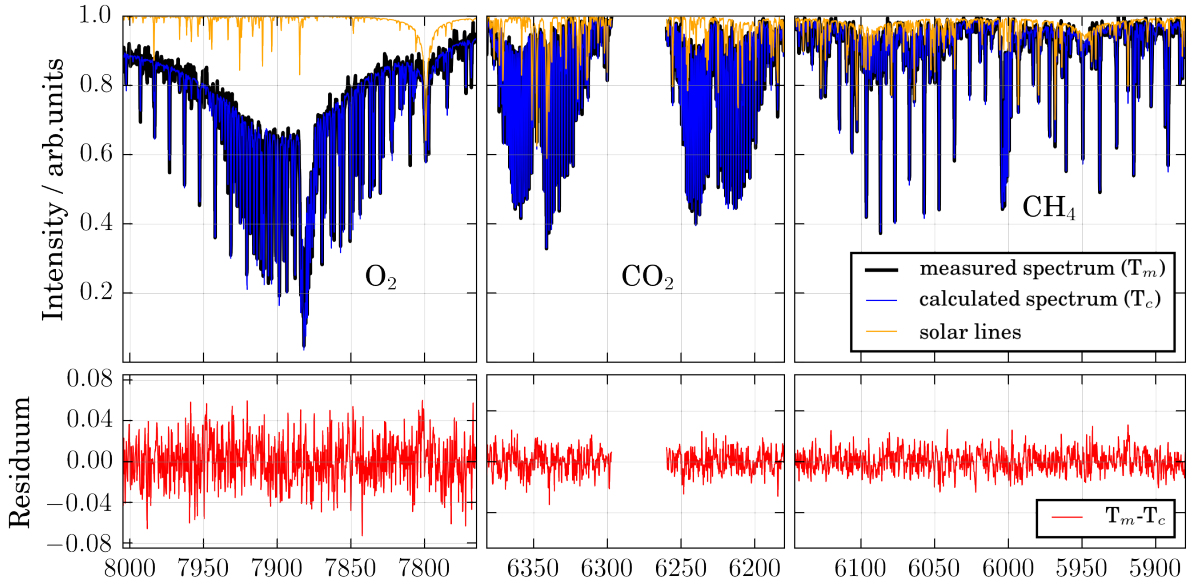

Figure 4.16.: Example fit of a measured spectrum (black line) on October 25 2015, the corresponding calculated spectrum (blue line), the contribution of the solar lines (orange) and their residuum (red line) for the retrieved windows of O_2, CO_2 and CH_4. *Published as Fig. 2 in Buschmann et al. [2017a].*

4.4.6. Filter conditions for lunar spectra

Lunar absorption spectra have been recorded as often as possible. Some have to be discarded for the final analysis, because their quality is insufficient to retrieve the DMFs of the target species reliably. A set of filter rules has been applied to each spectrum and only spectra that pass all criteria are used for further analysis. In all cases, the application of each filter rule has been tested on the whole data set and the impact on the removal of suspected outliers investigated. This section describes the individual filter conditions and justifies their application.

If the recorded time of a measurement does not match the time of the actual measurement, the real and assumed light paths will not match and the resulting wrong airmass will bias the retrieved DMF. Within the TCCON community the xAir parameter is used to identify this. It is defined similarly to Equ. 2.7 [Wunch et al., 2015]:

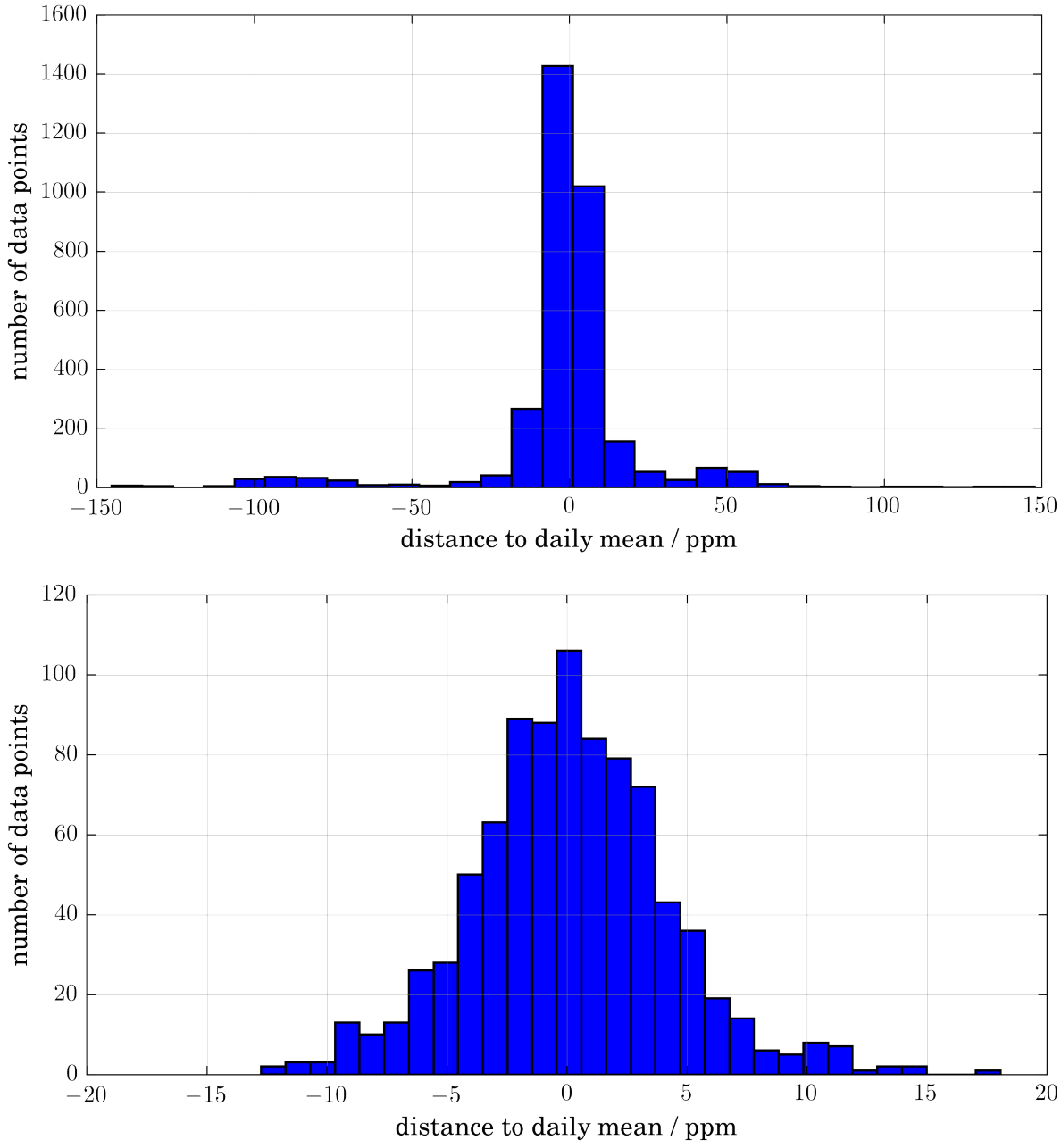

Figure 4.17.: Impact of the filter condition on the lunar NIR xCO_2 retrieval. Shown is the distribution of distance to the daily mean without any (top) and with all (bottom) filter conditions applied.

$$\mathrm{xAir} = \frac{\mathrm{VC_{air}}}{\mathrm{VC_{O2}}} 0.2095 - \mathrm{xH_2O} \frac{m_{\mathrm{H2O}}}{m_{\mathrm{air}}^{\mathrm{dry}}} \tag{4.3}$$

$$\mathrm{VC_{air}} = \frac{p_0 \mathrm{N}_a}{m_{dry}^{air} \bar{g}} \tag{4.4}$$

The network wide agreed value for a measurement is 0.98 [Wunch et al., 2015]. The xAir from lunar measurements shows greater scattering noise than typical solar retrieved xAir, as it depends on the retrieved O_2 column VC_{O_2}. Here, xAir values greater than (1.02) and smaller than (< 0.92) have been discarded. Additionally, the time stamps of the measurements have been verified by comparison to independently logged time stamps.

To be sure that the light path of the measured spectra is not influenced by sunlight backscattered in Earth's atmosphere, the lunar data are filtered by rejecting all times, where the solar zenith angle is $< 95°$, i.e. the Sun has to be more than 5° below the horizon. This was previously discussed in Sec. 4.4.3.

There are known issues for the TCCON measurements at high zenith angles, referred to as airmass-dependence. Which most likely is a result of uncertainties in the available spectroscopic data on O_2. For the final time series, all data with a lunar zenith angle $> 85°$ have been discarded.

The retrieval code performs an iterative least square fit of the calculated and measured spectrum in the target spectral region (as described in Sec. 2.3). If the fit does not converge in the preset maximum number of steps (set to 15), the corresponding data are discarded automatically. All data with number of iterations greater than 12 in any one of the target windows of CO_2, CH_4 and O_2 are discarded as well.

The FTS logs the maximum velocity deviation (MVD) of the scanning mirror during interferogram acquisition in the metadata of the data file. Disturbances in the scanner movement can cause spectral artifacts, therefore large deviations (MVD > 5) have been discarded. In the period before a realignment of the instrument in February 2013 most interferograms show greater deviations in scanner velocity. This behaviour points to an issue with the scanner rope tension at this time and the corresponding values have been flagged accordingly.

Finally, the fit residuum, i.e. the difference between the fitted and the measured spectral window, are calculated during the retrieval process and automatically converted to DMF-errors (in ppm or ppb) by GFIT. This filter is, of course, dependent on the spectral noise. The spectra taken at the beginning of the time series have a generally lower signal to noise ratio. A more strict filter setting for the later, lower resolution measurements with a better signal-to-noise ratio is sensible. As this filter is applied last and the previous

filter rules should have discarded most of the outliers already, fairly loose filter conditions have been selected here. The filters for early measurements have been set to maximum errors of 120 ppm for CO_2, 500 ppb for CH_4 and 10 % for O_2. For the later lower-noise measurements, maximum errors of 40 ppm for CO_2, 200 ppb for CH_4 and 5 % for O_2 have been selected. A spectrum is discarded, when any of the three conditions are met. It should be noted, that the presented filter conditions are not mutually exclusive.

In case of CO_2 very little daily variation should be perceivable in the total column. The distribution of all values around the daily mean should therefore be Gaussian. Figure 4.17 highlights the effect of the filter settings on the time series. Here, the all retrieved xCO_2 values have been de-trended by substracting their respective daily means. Without the filter applied, clear aggregations of outliers can be observed non-symmetrically around the daily mean. After the application of the filters, the distribution is a lot more symmetrical and Gaussian-shaped, as it should be.

4.5. Validation by solar absorption retrieval

This section was published as Sec. 4 in Buschmann et al. [2017a]. References and citations have been updated.

The validation of the measurements performed during the polar night is difficult. In the absence of other options, here we compare to solar absorption measurements taken within TCCON. In spring and autumn there are a few consecutive days around the full moon when solar absorption measurements during the day and lunar absorption measurements during the night are possible. Such comparison measurements were performed in March and September 2013. Here the DMFs of xCO_2 and xCH_4 for both solar and lunar measurements were retrieved using equation 2.6. For the comparison of xO_2 equation 2.7 was used, respectively.

Assuming the total column values do not change significantly during that time period, the means of the two retrievals can be compared directly. Figure 4.18 shows the comparison results and the calculated means for a comparison in September 2013. Table 4.4 shows the corresponding values of the arithmetic mean and its standard deviation as an indication of the error for both comparison campaigns in March and September 2013. The same analysis was performed on the available smoothed model output. The calculated standard deviation of the models of about 0.2 ppm and 0.3 ppm for CO_2 and 1.0 ppb and 1.6 ppb for CH_4 for March and September, respectively, indicate that the assumption of stable DMFs for the observed time frame is reasonable.

The accuracy of the lunar measurements can be determined via the bias of the lunar compared to the solar measurements and can be deduced from Table 4.4 as well. In

		xCO_2 [ppm]	xCH_4 [ppb]	xO_2 [%]
March 2013	solar	397.47 ± 0.67	1773.78 ± 2.99	21.33 ± 0.08
	lunar	396.81 ± 3.89	1775.72 ± 17.64	21.34 ± 0.36
	Jena CO_2	398.01 ± 0.13	–	–
	CT15 CO_2	396.89 ± 0.22	–	–
	MACC CO_2	397.16 ± 0.18	–	–
	MACC CH_4	–	1784.09 ± 1.06	–
September 2013	solar	393.16 ± 0.49	1810.26 ± 3.11	21.38 ± 0.06
	lunar	392.15 ± 8.03	1813.62 ± 38.02	21.40 ± 0.60
	Jena CO_2	391.56 ± 0.26	–	–
	CT15 CO_2	391.29 ± 0.24	–	–
	MACC CO_2	392.07 ± 0.39	–	–
	MACC CH_4	–	1800.79 ± 1.58	–

Table 4.4.: Comparison of the retrieved solar, lunar and model DMFs for the two comparison time periods. Note that xO_2 was calculated using the surface pressure and the offset to the true atmospheric value of 20.95% is caused by spectroscopic errors. *Published as Tab. 2 in Buschmann et al. [2017a].*

March 2013 the difference between solar and lunar measurements is 0.66 ± 4.56 ppm for xCO_2 and -1.94 ± 20.63 ppb for xCH_4. In the September 2013 campaign a bias of 1.01 ± 8.52 ppm for xCO_2 and -3.36 ± 41.13 ppb for xCH_4 can be observed. The diurnal variability of the lunar measurements is used to define the precision. As the later measurements have a higher precision, a typical value achieved in the 2014/2015 winter is used. Here the standard deviations of the daily mean of 2 ppm for xCO_2 and 10 ppb for (xCH_4), corresponding to 0.5 % in both cases.

The target accuracy can be estimated via the detrended year-to-year wintertime variability. Here model output can be used as a proxy. In the smoothed, detrended MACC CO_2 and CH_4 model (see Sec. 4.6.1) the arithmetic mean of the first week of January differs by 0.55 ppm in xCO_2 and 9.84 ppb in xCH_4 between 2012 and 2014. At the same time, the standard deviation of all values for the first week of January between 2012 and 2014 is about 1.8 ppm for xCO_2 and 18.8 ppb for xCH_4. However, these estimates are potentially subject to unknown biases in the models, i.e. the model could be biased similarly every year. Additionally, the seasonal variability surely is an upper limit for the target precision. Here the seasonal cycle amplitude measured by solar FTS is about 15 ppm for xCO_2 and about 40 ppb for xCH_4.

As described in section 2.3.7 (see equation 2.6), the dry-air column is calculated using the vertical column of O_2, retrieved from the 7885 cm^{-1} spectral region. Here airglow emissions in the high atmosphere could potentially disturb the O_2 spectra. This can typically be ignored in solar absorption spectra, as the magnitude of the emissions is

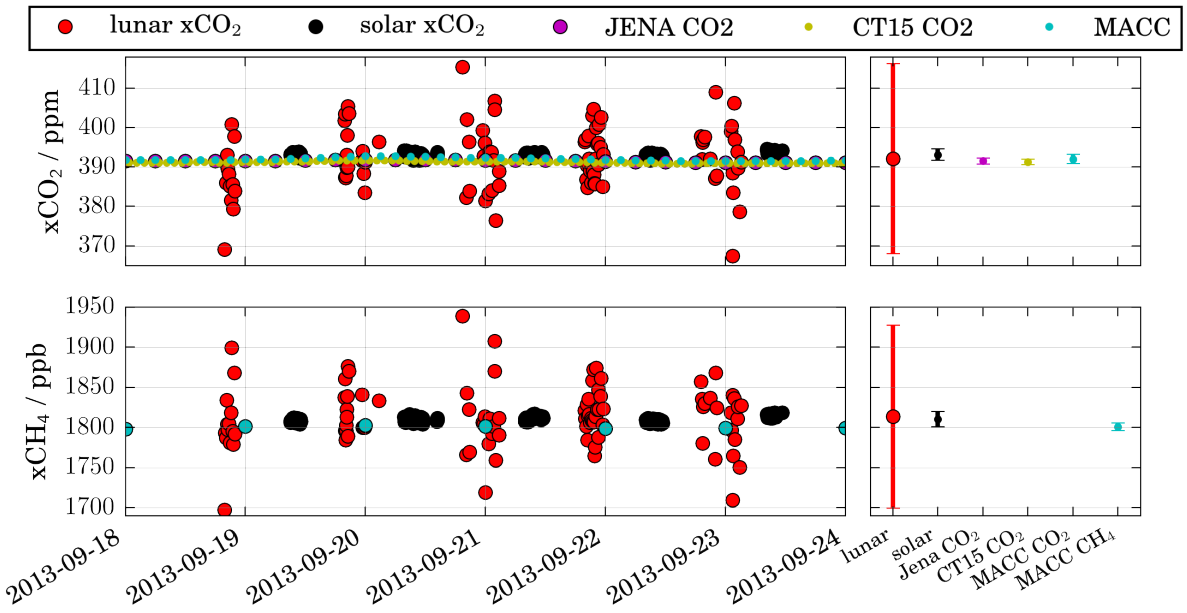

Figure 4.18.: Comparison of the solar and lunar measurements of xCO_2 and xCH_4 in September 2013 (dots) and the corresponding arithmetic means (lines). Values are given in Table 4.4. *Published as Fig. 10 in Buschmann et al. [2017a].*

negligible, when viewing directly into the sun. In case of lunar spectra, however, air-glow emissions could potentially fill in the spectral lines and influence the measurements. To test this, xO_2 was retrieved using the surface pressure to calculate the dry-air column as described in equation 2.7.

In both comparison periods, no significant difference between the solar and lunar retrievals of xO_2 can be observed. Note that xO_2 retrieved via surface pressure shows an offset of 0.4 % in both cases (lunar and solar). This offset originates in the line parameters used for the O_2 retrieval and is compensated in the xCO_2 and xCH_4 retrieval with the TCCON in-situ correction. Washenfelder et al. [2006] reported values that are 2.27 ± 0.25 % larger if the surface pressure retrieved dry column was used. Here we find a mean difference of 1.96 ± 0.14 %, when calculating the mean and standard deviation of the solar and lunar mean xO_2 values shown in the sidebars in Fig. 4.19. Note that these retrievals were performed with updated spectroscopy available within GGG2014 compared to that used by Washenfelder et al. [2006].

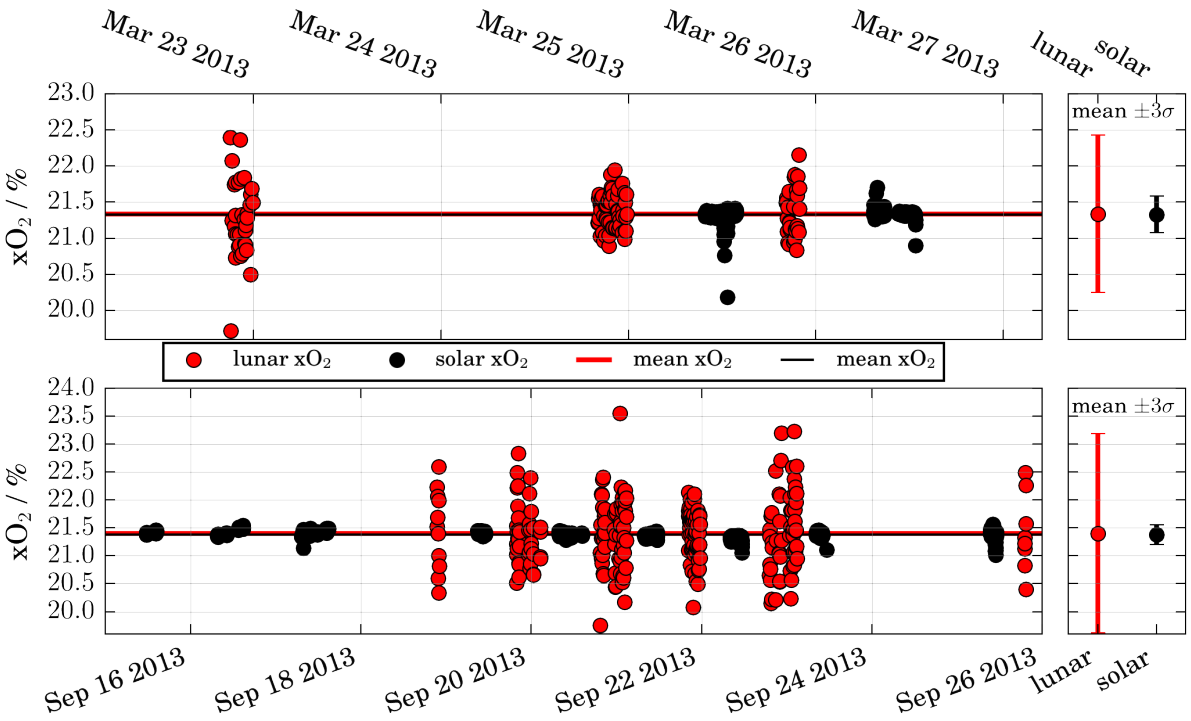

Figure 4.19.: Comparison of the solar and lunar measurements of xO_2 in March and September 2013. *Published as Fig. 11 in Buschmann et al. [2017a].*

4.6. Comparison of the new time series to model simulations

4.6.1. Averaging kernel smoothing

An abbreviated version of this section was published as Section 5.1 in Buschmann et al. [2017a]. References and citations have been updated.

The rigorous comparison of ground-based column measurements of a trace gas to model simulations requires resampling the model profile as if it was measured by the instrument. The smoothed column dry-air mole fraction $\hat{c}$ can be calculated following Connor et al. [2008]; Rodgers and Connor [2003]; Wunch et al. [2010] by adding the column integrated a priori profile (c_a) to the difference between the model ($\mathbf{x}$) and the dry TCCON a priori profile ($\mathbf{x_a}$) weighted with the averaging kernel ($\mathbf{a}$):

$$\hat{c} = c_a + \mathbf{h}^T \mathbf{a}^T (\mathbf{x} - \mathbf{x}_a) \tag{4.5}$$

Here, **h** represents the pressure weighting function (see Connor et al. [2008]). Following [Connor et al., 2008; Rodgers and Connor, 2003; Wunch et al., 2011b], the vertical columns of the target species accounting for the averaging kernel sensitivity are:

$$VC_{gas,ak} = \sum_i \frac{f^{dry}_{gas,i}\ a_i\ \Delta p_i}{g_i\ m^{dry}_{air}\ \left(1 + f^{dry}_{H_2O,i}\ \frac{m_{H_2O}}{m^{dry}_{air}}\right)} \tag{4.6}$$

and the vertical column of dry-air:

$$VC_{air} = \sum_i \frac{\Delta p_i}{g_i\ m^{dry}_{air}\ \left(1 + f^{dry}_{H_2O,i}\ \frac{m_{H_2O}}{m^{dry}_{air}}\right)} \tag{4.7}$$

with the wet-air correction:

$$f^{dry}_{H_2O} = \frac{f_{H_2O}}{1 - f_{H_2O}} \tag{4.8}$$

and correcting the dry-air TCCON a priori:

$$x^{dry}_a = f^{dry}_{gas} = \frac{f_{gas}}{1 - f_{H_2O}} \tag{4.9}$$

This yields the smoothing equation:

$$\hat{c} = c_a + \left(\frac{VC^{model}_{gas,ak} - VC^{apriori}_{gas,ak}}{VC_{air}}\right) \tag{4.10}$$

The pressure weighting function was used as derived in Connor et al. [2008]:

$$h_i = \left| \left(-p_i + \frac{p_{i+1} - p_i}{\ln\left(\frac{p_{i+1}}{p_i}\right)}\right) + \left(p_i - \frac{p_i - p_{i-1}}{\ln\left(\frac{p_i}{p_{i-1}}\right)}\right) \right| \tag{4.11}$$

Given a vertical model profile, the measurement's averaging kernel and the vertical columns of water vapour and the a priori profile of the target gas, the smoothed dry-air mole fraction of the model output can be calculated. Due to the high random error of the lunar FTS measurements, daily means have been calculated for both the measurements and the model data, after the smoothing was applied.

4.6.2. Lunar Averaging Kernels

This subsection was published as Sec. 3.5 in Buschmann et al. [2017a]. References and citations have been updated.

The sensitivity of the retrieved dry-air mole fraction of the target gas depends on the a priori information and the measurement's altitude dependent sensitivity, i.e. the averaging kernels. The a priori profiles used are the default TCCON ones. The averaging kernel of a measurement strongly depends on the retrieval methodology and the information content of the corresponding spectrum. As such it depends on the viewing geometry as well as the resolution, the absorption strength and the signal-to-noise ratio. The weight different altitude levels have in the retrieval can be parameterized as a function of the zenith angle. As the instrument faces the light source at a certain zenith angle, the measurement samples different contributions from the various atmospheric layers. The pressure broadening of the absorption features shows a specific altitude dependent sensitivity and this information depends on the chosen resolution and the signal-to-noise ratio of the measurement.

The set-up of the lunar measurements is similar to that of TCCON measurements, and therefore the averaging kernels are quite similar, aside from effects of resolution and noise for a given zenith angle. The top panel in Fig. 4.20 shows the averaging kernels for the lunar measurements. The middle panel shows the difference from the standard TCCON ones from Ny-Ålesund, interpolated to the corresponding zenith angles. The lines are color gradient coded with their respective zenith angles and different color schemes reflect different resolutions.

Pressure broadening leads to spectral lines originating from gases at low pressure being narrower than those at higher pressure. The narrow part of a spectral line sampled with fewer points therefore cannot give as much information as one with higher resolution. This leads to averaging kernels from low resolution spectra being less sensitive to the stratosphere and more sensitive in the lower troposphere than their high resolution counterparts. This can be seen in the lower panel of Fig. 4.20, where the difference between standard TCCON averaging kernels and their lower-resolution counterparts at the same zenith angle is shown. As expected, decreasing the spectral resolution leads to greater differences between the averaging kernels.

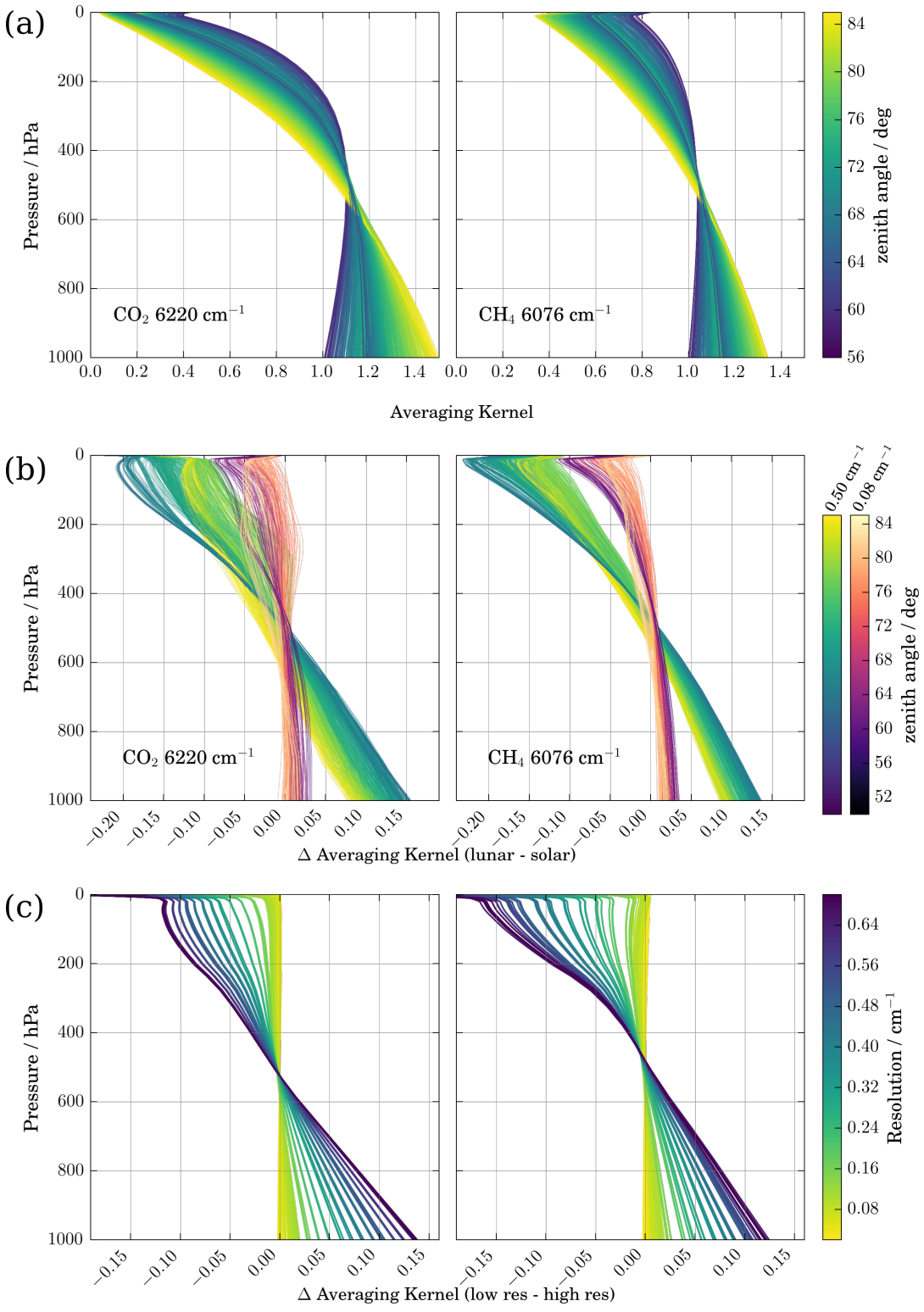

Figure 4.20.: (a) Averaging kernels of the lunar measurements. (b) Difference between lunar and solar averaging kernels color coded for different spectral resolutions. (c) Differences between low resolution and TCCON spectra averaging kernels as a function of resolution. *Published as Fig. 9 in Buschmann et al. [2017a].*

4.6.3. Model comparison – time series

This subsection was published as Sec. 5.2 in Buschmann et al. [2017a]. References and citations have been updated.

In this section the FTIR time series is compared to CO_2 model results from three different models: the MACC CO_2 model version 14r2 [MACCCO2, 2016], the CarbonTracker 2015 [CT2015, 2016] model and the Jena CO_2 inversion version s04_v3.7 [JenaCO2, 2005]. In case of the CH_4 time series, the MACC CH_4 v10 [MACCCH4, 2016] is used. As described in Section 4.6.1 the models DMF profile has been smoothed with the corresponding a priori and averaging kernel of the lunar and solar measurement, respectively. For times where there are no FTS measurements available, an averaging kernel was calculated using the solar zenith angle of the corresponding time. In winter the lunar zenith angle was used instead. For times where no FTS measurements were possible at all, e.g. Sun and Moon are below the horizon, a mean zenith angle of 65° was assumed.

The resulting model time series can now be compared directly to the FTS measurements. Figure 4.22 shows the comparison of the FTS and the smoothed model time series for CO_2. The CH_4 comparison is shown in Fig. 4.21.

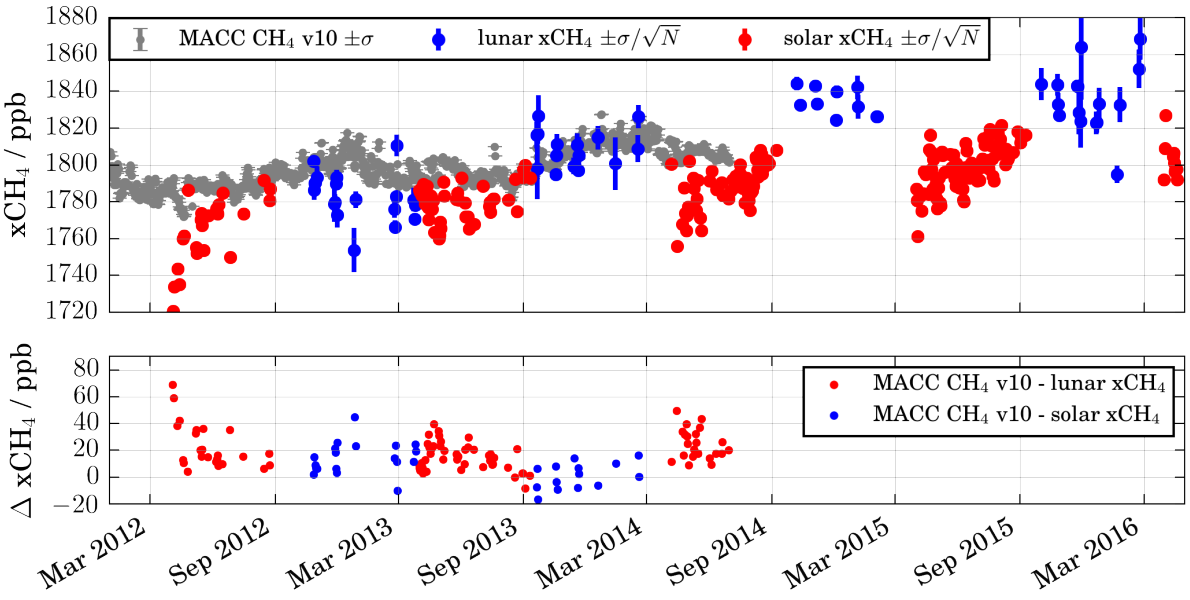

Figure 4.21.: Comparison of the daily means of lunar (blue) and solar (red) xCH_4 FTIR measurements to the AK-smoothed MACC CH_4 model v10 (gray). Errorbars show the standard error ($\sigma/\sqrt{N}$, with N number of measurements).The lower panel shows the difference model - measurement. *Published as Fig. 13 in Buschmann et al. [2017a].*

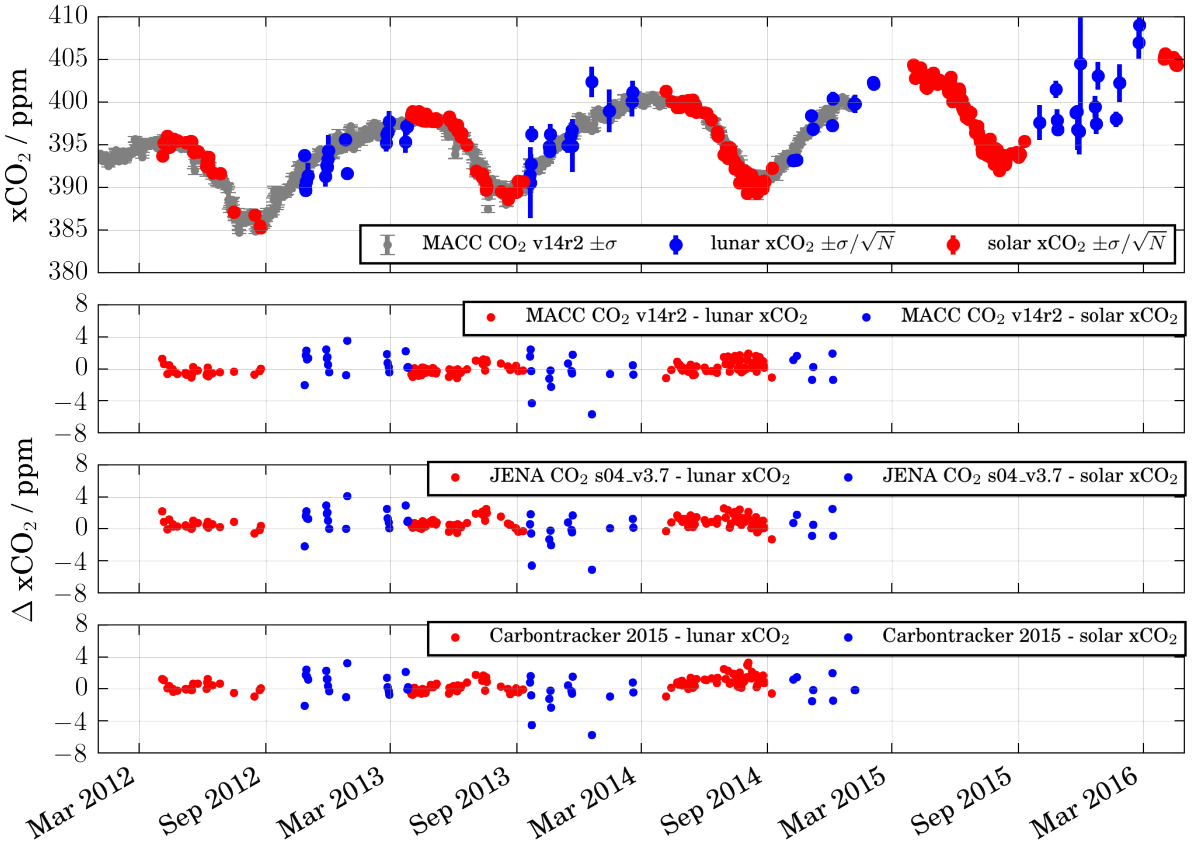

Figure 4.22.: Comparison of the daily means of lunar (blue) and solar (red) xCO_2 FTIR measurements to the AK-smoothed MACC CO_2 model v14r2 (top panel, gray). Errorbars show the standard error ($\sigma/\sqrt{N}$, with N number of measurements). The lower panels show the difference model - measurement for all models. *Published as Fig. 12 in Buschmann et al. [2017a].*

4.6.4. Model comparison – seasonal cycle

This subsection was published as Sec. 5.3 in Buschmann et al. [2017a]. References and citations have been updated.

The detrended seasonal cycles of both target species are similar from year to year. In the following, the detrended seasonal cycles are compared to the models already discussed in section 4.6.3.

Figure 4.23 shows the seasonal cycle of xCO_2 as observed with the Ny-Ålesund FTS between 2012 and 2016, detrended with a linear increase of 2.6 ppm yr^{-1}, an offset of 380.0 ppm on 1 January 2012 and condensed to 1 year. The seasonal cycle of xCO_2 shows little difference between the three models, and therefore the comparison can be performed with an model average. The shaded area in Fig. 4.23 shows the 3σ standard deviation

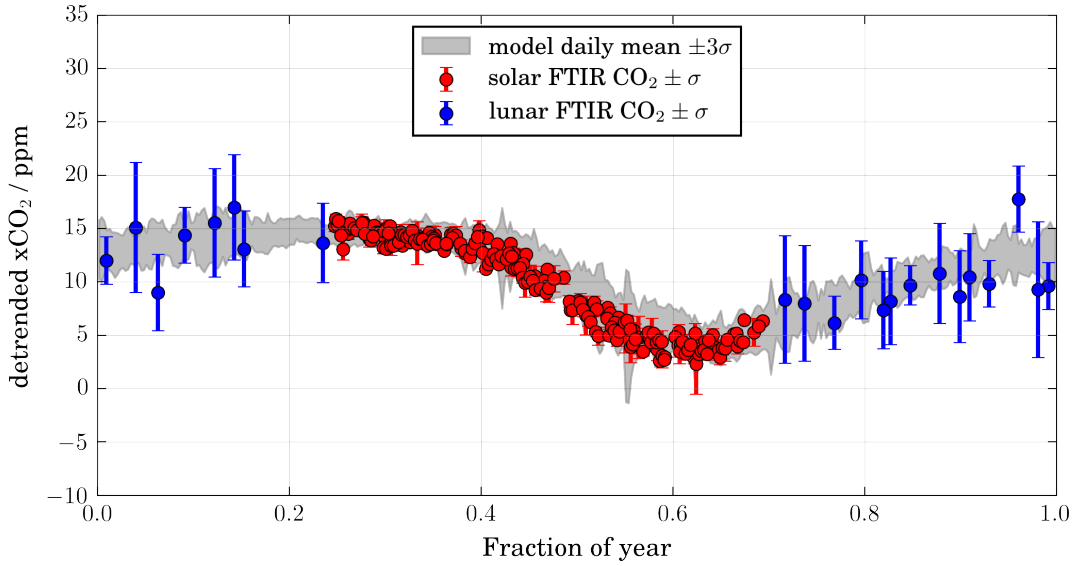

Figure 4.23.: Comparison of solar (red) and lunar (blue) xCO_2 FTIR measurements. Errorbars show 1σ standard deviation of the daily mean. The lunar data points have been averaged over one full moon period each. The shaded gray area shows the 1σ standard deviation of the three model daily means (MACC, CarbonTracker and Jena) as shown in Fig. 4.22. *Published as Fig. 14 in Buschmann et al. [2017a].*

around the daily mean of the combined model data points of all three models (MACC, CarbonTracker and Jena). The weighted average of all FTS measurements during one full moon period is shown (green dots) with errorbars corresponding to the standard error ($\sigma/\sqrt{N}$) of the daily mean calculated from N measurements. The weights are chosen to be the inverse squared residual of the spectral fits.

The difference between the models and the TCCON measurements in summer is quite small, except for a phase shift in the onset of the downward slope at the beginning of the growing season decline. In winter the models agree well with the FTIR lunar absorption measurements, within the given error margin.

In the case of CH_4 a similar comparison has been performed and the results can be seen in Fig. 4.24. Here the xCH_4 time series have been linearly detrended with an annual increase of 10.6 ppb yr^{-1} and an offset of 1760.0 ppb on 1 January 2012. Figure 4.24 shows the 3σ standard deviation around the daily means of the MACC CH_4 model (shaded area) compared to the FTS measurements (red and blue dots) averaged over one full moon measurement cycle. The error bars correspond to the 1σ standard deviation of the mean.

In spring/summer the FTS measurements show generally smaller values than the model and a larger spread. From late summer throughout the winter the measurements are in better agreement with the model. At specific events in spring, the FTS measurements

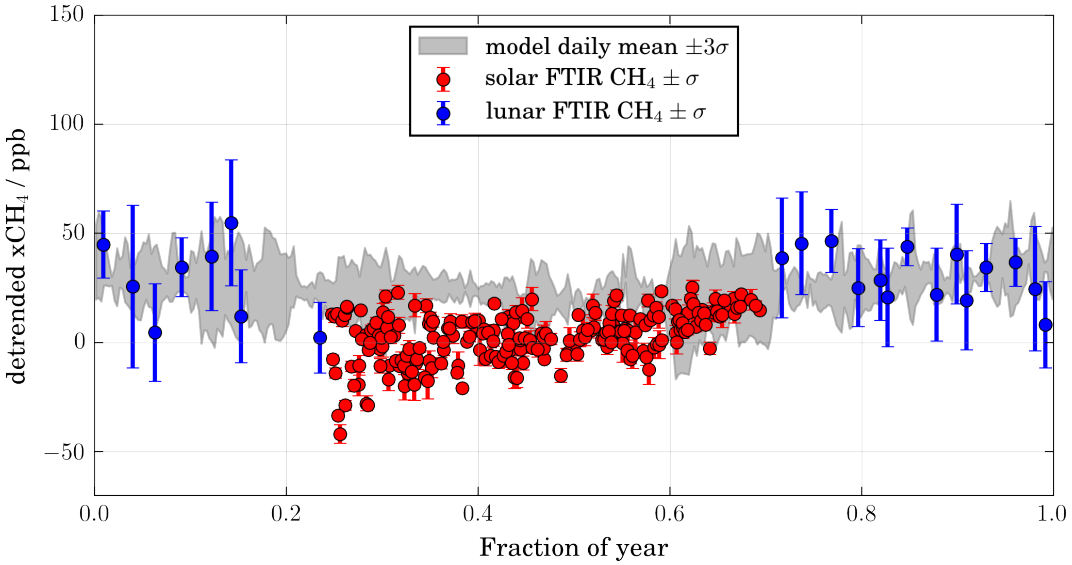

Figure 4.24.: Comparison of solar (red) and lunar (blue) xCH_4 FTIR measurements. Errorbars show 1σ standard deviation of the daily mean. The lunar data points have been averaged over one full moon period each. The shaded gray area shows the 1σ standard deviation of the MACC CH_4 model daily means as shown in Fig. 4.21. *Published as Fig. 15 in Buschmann et al. [2017a].*

show sudden decreases of xCH_4 (compare Fig. 4.21 and Fig. 4.24). This could be due to the model not being able to capture vertical transport very well, which has been shown previously by Ostler et al. [2016]. Here, stratospheric intrusions during the breakdown of the polar vortex in spring can lead to large, short-term decreases in xCH_4. This is currently being investigated by using a stratospheric species as a tracer to seperate the xCH_4 column in a tropospheric and stratospheric part and exceeds the scope of this paper.

4.7. Comparison to ground-based in-situ measurements

In addition to the comparison of the xCO_2 and xCH_4 time series' to model simulations, they can also be compared to in-situ measurements. At the GAW (Global Atmospheric Watch) station Zeppelin Observatory, on a mountain at an altitude of 475 m just south of Ny-Ålesund, atmospheric abundances of various trace gases are measured routinely. The flask samples are analyzed and available online via the NOAA GMD (Global Monitoring Division) [Dlugokencky et al., 2014].

Although the measurements offer high precision, the temporal coverage is limited to the time, when the flasks are filled. Additionally they do not have a vertical resolution, i.e. they only sample boundary layer air.

As such, these measurements provide complementary information on the atmospheric composition, which has to be considered, when comparing them directly to remote sensing measurements. A smoothing correction, similar to the ones presented in the previous chapters for FTS-to-FTS or FTS-to-model comparisons is not possible.

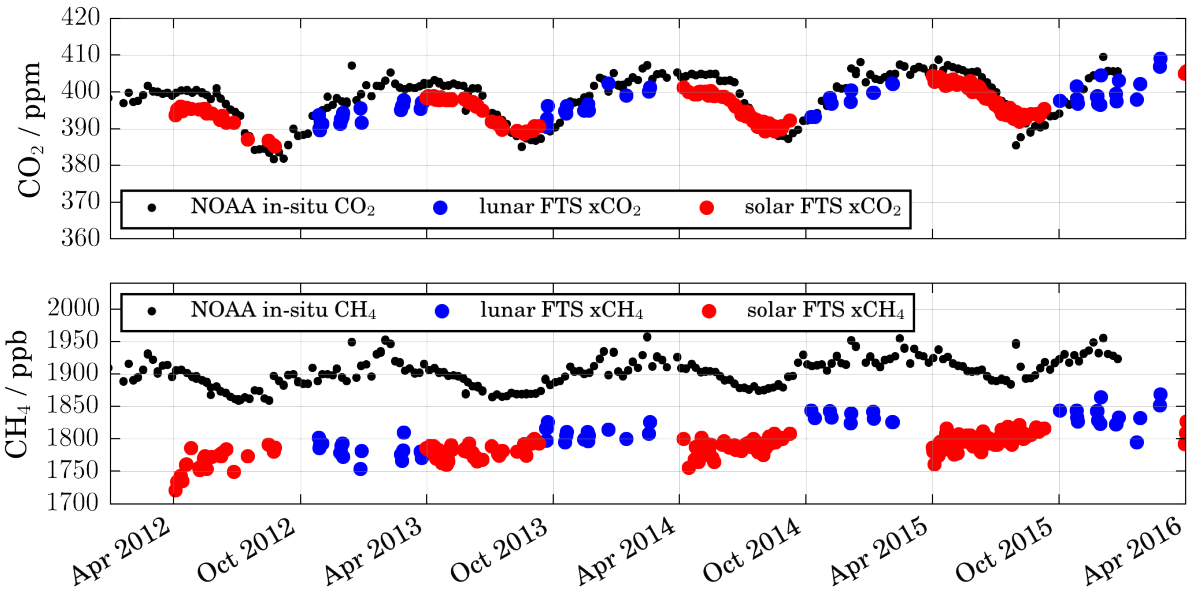

Figure 4.25.: Comparison of NOAA surface flask measurements from Zeppelin station (black dots) to the FTS timeseries from solar (red) and lunar (blue) retrievals. Note that no averaging kernel smoothing was applied.

Figure 4.25 shows the retrieved daily mean time series from solar (red) and lunar (blue) absorption measurements for both xCO_2 and xCH_4. The in-situ flask data is shown in black. The xCO_2 time series shows a generally good agreement. Differences can be seen in the seasonal cycle amplitude. The FTS measurements have slightly higher values in autumn (minimum) and smaller values in spring (maximum). This dampening is caused by the inherent column averaging of the xCO_2 measurement. Additionally, a slight phase shift between the FTS and in-situ measurements can be observed. The seasonal minimum is reached slightly later (on the order of days) in the year by the in-situ measurements. This can be explained by the time lag between local boundary layer conditions and their propagation into the total column and, additionally, the influence of atmospheric transport on the total column composition.

For xCH_4, the differences are greater. A significant offset is visible between the in-situ and remote sensing measurements. The bulk of which can be attributed to the strong stratospheric sink for CH_4, which leads in the column average to a reduction throughout the year. In specific cases, stratospheric intrusions in spring lead to a sudden drop in xCH_4, that is not captured by the in-situ measurements, which was already discussed in the previous section.

4.8. Conclusion

In this chapter the usage of near-infrared lunar absorption spectra was investigated. The Ny-Ålesund time series of xCO_2 and xCH_4 was extended to the polar night from 2012 to 2016. An estimate of the lunar irradiance shows about 6 orders of magnitude smaller intensity than direct sunlight. The usage of a thermo-electrically cooled InGaAs detector increases the sensitivity by 3 orders of magnitude. Additionally, a larger entrance aperture, the reduction of spectral resolution and averaging over multiple interferograms provide an increase in spectral signal-to-noise ratio. The first setup of the detector and early comparison between solar and lunar absorption measurements were performed in Bremen. These showed the need for further improvement of the signal-to-noise ratio. The impact of lower resolution and increased noise on the retrieval was tested and a continuously optimized set of measurement parameters implemented for the measurements in Ny-Ålesund. Eventually, a spectral resolution of 0.5 cm^{-1}, an integration time of under 10 minutes, corresponding to 40 interferogram scans and a maximum entrance aperture of 3.15 mm were selected.

Additionally, several potential issues of the lunar measurements have been addressed. If the Sun is above $-5°$ elevation, backscattered sunlight can result in a badly defined light path of the lunar measurements and subsequently the corresponding retrieved values have to be discarded. The atmospheric model used in the retrieval process was optimized to use reanalysis data interpolated to the local noon. The impact of an atmospheric model interpolated to the actual time of measurement was investigated and implemented for the lunar retrieval. Example time series show a difference of up to ± 1 ppm for xCO_2 and ± 2 ppb for xCH_4 for retrievals from both solar and lunar absorption spectra, when comparing to the previous atmospheric model selection. No evidence of bias introduced by airglow was found by comparing the retrieved oxygen column of both solar and lunar measurements. Similarly, the influence of the doppler broadened Fraunhofer lines in the disk averaged solar spectrum is correctly implemented in the retrieval code. A set of filter conditions was found to discard unreliable data and implemented in the lunar post processing routine.

The lunar measurements show, under optimal conditions, a standard deviation of the daily mean (1σ) of about 2 ppm for xCO_2 and about 10 ppb for xCH_4, corresponding to a precision of about 0.5 %. The lunar time series of xCO_2 and xCH_4 has been validated with TCCON measurements during two campaigns, where solar spectra were recorded during the day and lunar spectra recorded during the night in spring and autumn 2013. The observed bias between the two time series was not significant. The time series were also compared to model simulations of various reanalysis models. For xCO_2, the time series was compared to three CO_2 models: the MACC CO_2 model (v.14r2), CarbonTracker 2015, Jena CO_2 inversion (s04_v3.7). All models show a generally good agreement. For xCH_4, the FTS measurements were compared to the MACC model (v10). The comparison

shows a good agreement in autumn/winter, but larger differences in spring, probably due to stratospheric intrusions not captured in the model. Finally, the lunar measurements were compared to available surface in-situ measurements. For CO_2, these show a larger seasonal cycle amplitude and a slight phase shift of the cycle. The stratospheric depletion of CH_4 leads to generally smaller column averaged abundances compared to the surface measurements.

5. Summary & Outlook

The goal of this thesis has been to extend the Ny-Ålesund time series of xCO_2 and xCH_4. To achieve this, two options were investigated, the usage of middle-infrared spectra already routinely measured and the introduction of a new detector to enable lunar absorption measurements during the polar night. The conclusions from both will be detailed in the following.

MIR retrieval of xCO_2 and xCH_4

For xCO_2 a set of spectral microwindows with distinct absorption lines of CO_2 was chosen to perform a profile scaling retrieval on. An initial analysis showed promising results for the xCO_2 time series. However, a more detailed analysis reveals the strong dependence of the retrieved values on the chosen a priori profile. The main cause was found to be the shape of the averaging kernels, that show high sensitivity of stratospheric contribution and very low sensitivity in the troposphere. By choosing a fixed, constant a priori it was shown, that the secular increase in xCO_2 is well captured and independent of the a priori. However, the seasonal cycle is strongly dampened and very much dependent on the a priori. This effect was quantified by performing a smoothing error estimation. For this, the time series were smoothed using the CarbonTracker model as a proxy for the true atmospheric profile. It was shown, that this correction is not able to compensate for the dampened seasonal cycle. In summary, the approach to retrieve xCO_2 from mid-infrared spectra works well to retrieve the secular increase but the results for shorter time scales, like the seasonal cycle, are not captured reliably. Additionally, the retrieval of xCH_4 has been briefly investigated. Similarly to the previous case, the results are dependent on the chosen a priori, as has been shown elsewhere [Sussmann et al., 2013]. The suggested retrieval was extended to include additional microwindows and applied to the Ny-Ålesund lunar MIR absorption spectra.

The results of the MIR xCO_2 retrieval have been published in Buschmann et al. [2016].

Lunar absorption spectroscopy of xCO_2 and xCH_4

A new thermo-electrically cooled InGaAs detector was introduced that increases the sensitivity for low light conditions. Measurements of xCO_2 and xCH_4 have been performed in Bremen and Ny-Ålesund. The Ny-Ålesund time series has been extended to include the polar night from 2012 onwards. Several improvements to the measurement setup finally lead to a precision of about 2 ppm for xCO_2 and about 10 ppb for xCH_4 (here both represent the 1σ standard deviation of the daily mean) under optimal conditions.

Due to the lack of vertically resolved in-situ measurements (like Aircraft or AirCore profiles), the new time series was validated via the comparison to standard solar absorption TCCON measurements. Measurement campaigns in spring and autumn 2013 allowed for the Sun to be measured during the day and the Moon during the night and the results show no significant bias to the TCCON measurements. The validated product was then compared to various atmospheric reanalysis models. Three CO_2 models were chosen: MACC CO_2 model v. 14r2, CarbonTracker 2015 and Jena CO_2 inversion s04_v3.7. All show a good agreement with the FTS measurements. For CH_4, the MACC CH_4 model v10 was used. Here larger deviations between model and FTS are observed in spring, but the winter shows an overall good agreement. The xCO_2 and xCH_4 time series additionally has been compared to the Ny-Ålesund in-situ flask sampling product.

The initial proof-of-concept measurements in Bremen have been published in Buschmann et al. [2015]. The results of the lunar absorption retrieval and the model comparison have been published in Buschmann et al. [2017a].

Outlook

It was shown, that the information content of the middle-infrared xCO_2 and xCH_4 retrievals was insufficient to be used as a substitute for near-infrared measurements. However, the strong sensitivity of the retrievals in the stratosphere could be exploited by a profile retrieval approach to obtain stratospheric measurements.

The Ny-Ålesund TCCON time series as well as the lunar measurements have yet to be independently validated. The validation could be performed with aircraft profiles or with the new balloon based AirCore system [Karion et al., 2010]. However, a reliable guided return mechanism must be implemented before the deployment on an island such as Spitsbergen.

The high sensitivity of the cooled InGaAs detector could be used for surface reflection measurements in Ny-Ålesund. Similar to the measurements performed by Fu et al. [2014]

for the Los Angeles basin, the Ny-Ålesund FTS would then switch measurements between a solar- and ground-viewing geometry, overlooking the fjord. By scanning laterally across the fjord, mapping of the ocean – atmosphere gas fluxes would be feasible.

In a future study, the lunar absorption measurements can be used to validate satellite products. There are several thermal infrared sounding instruments currently in orbit, most prominantly the Infrared Atmospheric Sounding Interferometer (IASI) on MetOp and the Atmospheric Infrared Sounder (AIRS) on Aqua. They can perform measurements during polar night as they do not rely on reflected solar irradiance and so far no polar night specific ground-based validation scheme is available.

The adaptation of the lunar xCO_2 and xCH_4 measurements into the routine measurement schedule in winter allows for continued monitoring of changes to the Arctic total column carbon cycle. This enables the sustained monitoring of potentially large emissions from permafrost and sea floor seepage sources. The increasingly longer time series will decrease uncertainty in the shape of the seasonal cycles and the identification of sources and sinks in the Arctic can be inferred via atmospheric transport simulations.

Acknowledgements

This PhD project would not have been possible without the help and support from many people. First and foremost, I would like to thank Justus Notholt for the opportunity to work in the FTIR group at IUP. I am truly grateful for the possibility to pursue this PhD and the autonomy that allowed me to explore so many different aspects of the FTS measurements.

I would like to thank:

- Nicholas Deutscher, who supported me especially during his time at IUP and taught me a great deal about the retrieval process.
- Tine Weinzierl, for her thorough introduction to the quirks of the instruments in Bremen and Ny-Ålesund, the setup of the new detector and all the stories and laughs we shared in the lab or our common trips to Ny-Ålesund.
- Mathias Palm, for his introduction to optimal estimation, his continuous guidance on the retrieval process and helpful feedback on papers and this thesis.
- Thorsten Warneke, for his support on all kinds of topics from general physics to the carbon cycle.
- The AWIPEV staff, for their efforts to make the visits to Ny-Ålesund equally productive and fun. Especially Winfried Markert, who stayed up many nights to help measure as many lunar spectra as possible.
- All members of the FTIR group at IUP, especially Hella van Asperen for being the best office mate one can hope for.
- All members of IUP for providing an extremely pleasant and stimulating environment to work in.
- All participants of the ESSReS. The common seminars, lectures and excursions were always a great treat. Special thanks are in order to Klaus Grosfeld, Stefanie Klebe and Helge Meggers who made this all possible.
- The NDACC and TCCON, for the friendly acceptance into their communities and the great annual meet-ups.

- Bruker, specifically Gregor Surawicz for the help with the new detector.
- All co-authors, for all their feedback and suggestions.
- Sabrina Arnold for her helpful feedback on this thesis.
- Prof. Dr. John Burrows for agreeing to be the second reviewer of this dissertation.
- The open source communities of both Debian GNU/Linux and Python for their dedicated work.

Finally, I want to thank my family for their continuous encouragement and understanding for not seeing them as often as I probably should. Last but not least, Hanna, thank you for your unconditional support and our time together.

Funding

I would like to gratefully acknowledge the financial support I received from various sources. The main funding was provided by the German research foundation (DFG), who funded the lunar absorption measurements as part of the grant no. 404/17. Further funding was provided by the Horizon-2020 project "Gap Analysis for Integrated Atmospheric ECV CLImate Monitoring (GAIA-CLIM)" funded by the European Union under grant agreement No. 640276 and the Transregional Collaborative Research Centre TR 172 "ArctiC Amplification: Climate Relevant Atmospheric and SurfaCe Processes, and Feedback Mechanisms (AC)^3" funded by the DFG. Additionally, the costs of conference participations were partly covered by the Helmholtz Earth System Science Research School (ESSReS), the University of Bremen, the Connaught Summer Institute in Arctic Science by the Canadian NSERC CREATE Training Program in Arctic Atmospheric Science (CREATE-AAS) and the Wilhelm-und-Else-Heraeus-Foundation in collaboration with the German Physical Society (DPG).

A. Appendix

A.1. Estimation of lunar irradiance

The total irradiance of the Moon can be estimated by calculating the irradiance of the reflected sunlight and thermal emission by the lunar surface, assuming a black body in both cases. The power radiated by a black body is given by the Stefan-Boltzmann-Law

$$P = \sigma A T^4 \tag{A.1}$$

It depends on the Stefan-Boltzmann constant σ, the area A and the temperature T. Assuming a uniformly radiating black body, the irradiance R at a given distance l can be calculated by dividing P by the area of a sphere with radius l:

$$R = \frac{P}{4\pi l^2} = \frac{\sigma A T^4}{4\pi l^2} \tag{A.2}$$

The total irradiance of the Moon can now be compared to the total irradiance of the Sun for an arbitrary position above Earth's atmosphere (TOA). In case of the Moon, however there are two sources of radiation, the reflected sunlight and the thermal (black body) radiation emitted from the Moon's surface heated by incident sunlight.

The reflected radiation can be estimated by calculating the incident radiation from the Sun at the distance Sun – Moon and using the result as a source for the calculation of the irradiance on the Earth's TOA:

$$\begin{aligned} R_{\mathsf{Moon,reflected}} &= \frac{P_{\mathsf{Sun}}}{4\pi(l_{\mathsf{SE}} + l_{\mathsf{EM}})^2} A_{\mathsf{Moon,disc}} \frac{1}{l_{\mathsf{EM}}^2 4\pi} \\ &= \frac{\sigma T_{\mathsf{Sun}}^4 r_{\mathsf{Sun}}^2 r_{\mathsf{Moon}}^2}{4(l_{\mathsf{SE}} + l_{\mathsf{EM}})^2 l_{\mathsf{EM}}^2} \end{aligned} \tag{A.3}$$

This estimation solely depends on the black body temperature of the Sun's photosphere, the radii of Sun and Moon and the distances between Sun – Earth and Earth – Moon.

$$\begin{aligned} R_{\mathsf{Moon,reflected}} &= \frac{5.67 \cdot 10^{-8} \frac{W}{m^2 K^4} (5700K)^4 (7 \cdot 10^8 m)^2 (1.3 \cdot 10^6 m)^2}{4(1.5 \cdot 10^{11} m + 4 \cdot 10^8 m)^2 (4 \cdot 10^8 m)^2} \\ &\approx 3.4 \cdot 10^{-3} \frac{W}{m^2} \end{aligned} \tag{A.4}$$

The radiance of the lunar black body radiation reaching Earth's TOA can be calculated in a similar way:

$$\begin{aligned} R_{\mathsf{Moon}} &= \frac{P_{\mathsf{Moon}}}{4\pi l_{\mathsf{EM}}^2} \\ &= \frac{\sigma A_{\mathsf{Moon}} T_{\mathsf{Moon}}^4}{4\pi l_{\mathsf{EM}}^2} \\ &\approx \frac{5.67 \cdot 10^{-8} \frac{W}{m^2 K^4} (1.3 \cdot 10^6 m)^2 (335K)^4}{4\pi (4 \cdot 10^8 m)^2} \\ &\approx 0.6 \cdot 10^{-3} \frac{W}{m^2} \end{aligned} \tag{A.5}$$

A.2. Clear sky determination for automated measurements

In spring 2014 a new solar tracker assembly was installed at the observatory in Ny-Ålesund. The new system allows for semi-autonomous measurements without the need for an operator to start the process. The system relies therefore on a external trigger for detection of cloud free conditions. In case of sunlight, the sensors on the BSRN field monitoring the incoming solar energy flux can easily be used to determine the presence of clouds in front of the sun by setting a threshold that refers to the inbound energy under cloud free conditions. In case of moonlight the sensors are not sensitive enough to detect the difference in energy flux with and without direct moonlight.

Another measure for cloud cover is the ratio of outbound to inbound long wave radiation. Under cloud free conditions there is little atmospheric reflectance and the outbound energy flux is much greater than the inbound flux. The BSRN station Ny-Ålesund measures the long wave energy flux with a pyrgeometer between 3500 and 50000 nm. The above mentioned energy flux ratio for a moonlight measurement period in September 2013 is

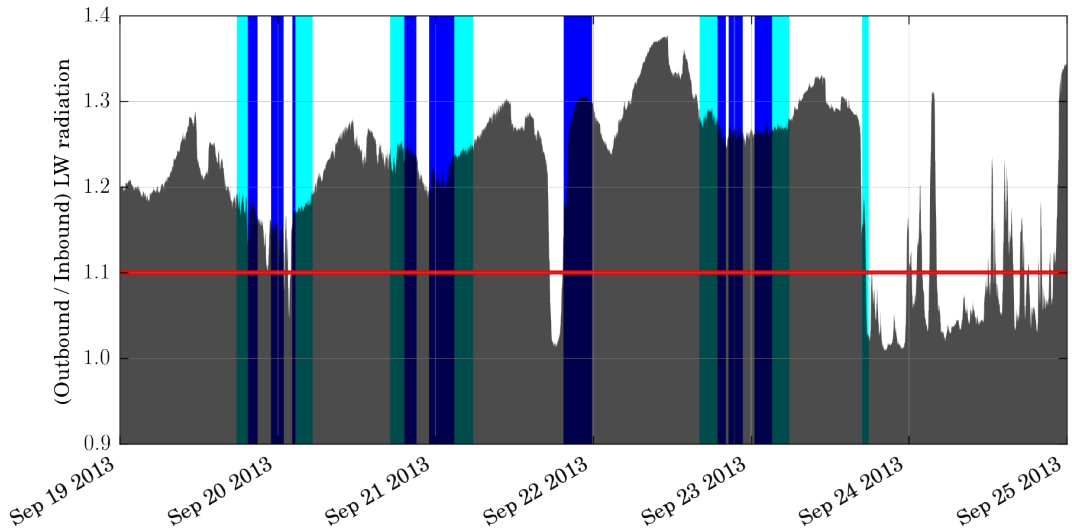

Figure A.1.: The ratio of outbound to inbound long wave energy flux as a function of time, measured with the BSRN stations pyrgeometer. The lines indicate the time when spectra were taken under cloud free conditions with the Sun (cyan) and Moon (blue).

shown in Fig. A.1. The cyan colored areas mark spectra taken under cloud free conditions when the solar altitude is below -3°. The blue colored areas show measurement times under cloud free conditions but with the Sun above -3°. A reasonable threshold for the ratio of outbound to inbound long wave radiation flux of 1.1 can be identified. This corresponding to a difference between outbound and inbound flux of about 40 Wm^{-2}. Below this value, cloud conditions can be considered too poor for high quality spectra. The parameters were implemented in the solar tracker software that retrieves the necessary BSRN data via the internal observatory data network.

A.3. FTS footprint

The profile scaling retrieval in GGG projects the slant column along the line-of-sight to the vertical column. This introduces spatial averaging, as in reality, the positions of measured gases in different altitudes are dependent on the zenith and azimuth angles of an individual measurement. This means that the atmosphere sampled at the heighest levels of the retrieved profile are further away from the location of the instrument than the lower levels.

A simple spherical model of the Earths atmosphere without consideration of refraction or dispersion can give an estimate of the actual location of the sampled air at different altitudes. In this simple model the distance to the instrument location can be calculated for latitudinal and longitudinal position via:

$$\Delta_{\mathrm{lat}}(y) = \cos(\beta)\frac{\mathrm{h}}{\tan(90^\circ - \alpha)}\frac{360}{2\pi r} \tag{A.6}$$

$$\Delta_{\mathrm{lon}}(x) = \frac{\mathrm{h}}{\tan(90^\circ - \alpha)}\sin(\beta)\frac{360}{\cos(x)2\pi r} \tag{A.7}$$

for a zenith angle α and a corresponding azimuth angle β and Earths radius $r = 6370$ for a latitude y and longitude x. The results are shown in Fig. A.2 for the lunar absorption measurements. The upper panel shows the positions of an air parcel, sampled at the color coded altitude on 2015-02-04 for 24 hours around the full moon for all possible lunar zenith angles in 10 minute intervals. The lower panel in Fig. A.2 shows the same plot for all lunar measurements from 2012 to 2016.

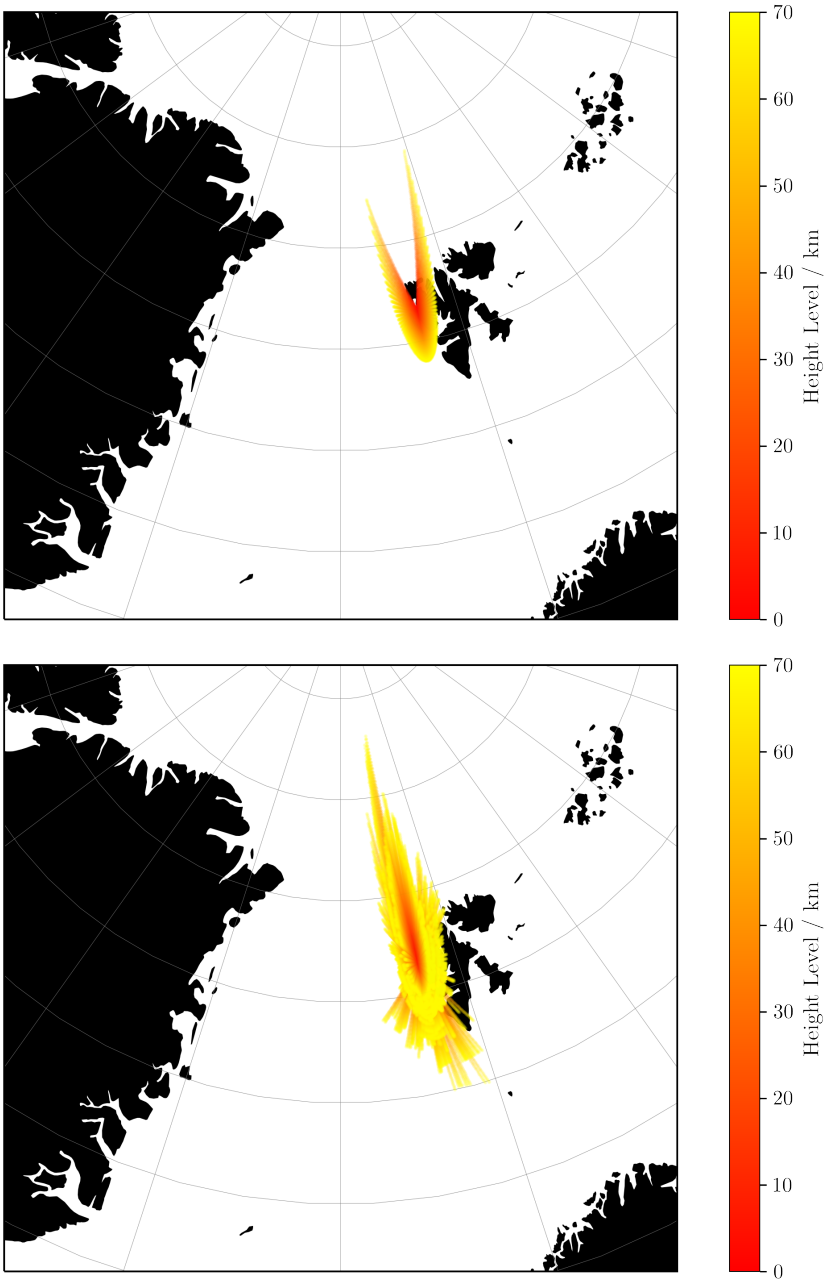

Figure A.2.: The positions of sampled air parcels for a given lunar zenith and azimuth angle and their altitude (colorbar). Top panel: All zenith and azimuth angles in 10 minute intervals within 24 hours around the full moon on 2015-02-04. Lower panel: Same as above, but for zenith/azimuth angles of all lunar measurements between 2012 and 2016.

A.4. Ny-Ålesund surface pressure calibration

In 2011 the surface pressure sensor was changed to the pressure sensor deployed by the Baseline Surface Radiation Network (BSRN). The BSRN data are made publicly available by AWIPEV at `https://doi.org/10.1594/PANGAEA.150000` [Maturilli et al., 2015]. Before 2011-08-22 the calibration was accounting for the height difference between the FTS and the previous pressure sensor[1]. The surface pressure correction can be calculated by

$$p = (p_{out} + \Delta p) e^{\frac{-g \cdot h}{R_{air}^{dry} \cdot T(K)}} \tag{A.8}$$

where T(K) is the local temperature in Kelvin ($T(K) = 6.4 + 273.15K$) and R_{air}^{dry} is the specific gas constant for dry air (R = 287J kg^{-1}K^{-1}) and g is the local gravitational acceleration of 9.83 ms^{-2}. This yields the previous pressure correction of

$$p_{out} = (p_{out} + 0.2) \cdot e^{\frac{-9.83 \cdot 8.7}{287 \cdot (t_{out} + 273.15)}} \tag{A.9}$$

The switch to the BSRN sensor required a re-calibration. On 2012-03-21 two Digiquarz pressure sensors were deployed to determine the pressure bias between the BSRN field and the Ny-Ålesund FTS. The pressure time series for the different sensors is shown in Fig. A.3. It has to be corrected for a sensor-to-sensor offset of 0.162 hPa. Taking this bias into account, this yields a pressure bias of 1.034 hPa that has to be substracted from the raw BSRN field data. Note that this only applies to the period where raw input is taken from the BSRN sensor.

The mean difference of 0.094 hPa between the Digiquartz at the BSRN field and the official BSRN pressure sensor might be due to inter-instrument biases and because the Digiquartz was located about 10 to 20 cm above the official sensor somewhere inside the sensor housing. This difference is therefore neglected and we directly compare the Digiquartz next to the FTS with the official BSRN sensor. For the actual offset calculation we calculate the height difference between the official BSRN field sensor and the FTS according to the formula above. First the mean difference between the BSRN sensor and the FTS sensor is: -0.94 hPa .

Solving the equation above for h yields:

$$h = \frac{R}{g} T(K) \ln \frac{p_0}{p} = \frac{287}{9.83} 279.55 \ln \frac{p_{BSRN}}{p_{FTS} - 0.162} \tag{A.10}$$

[1] private communication with Siegrid Debatin, AWI Potsdam and Mathias Palm, IUP Bremen

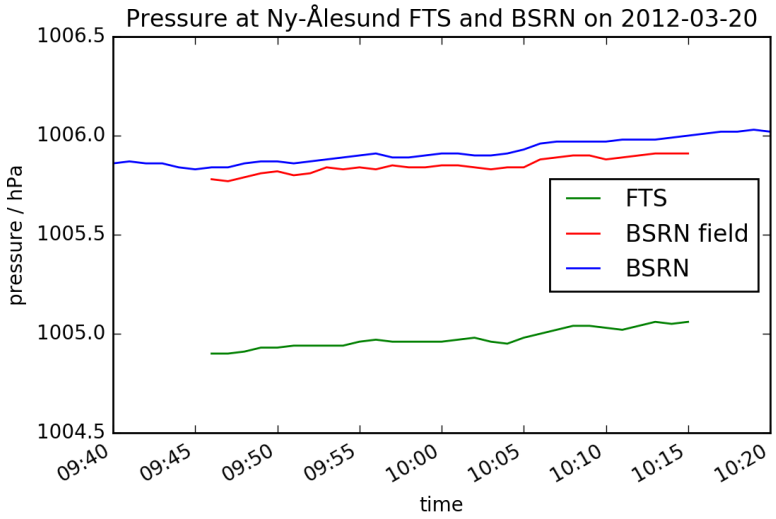

Figure A.3.: The surface pressure measured in parallel, by the BSRN sensor (blue) and independently at the BSRN site (red) and next to the FTS (green).

Taking the mean of the parallel comparison measurements for p_{bsrn} and p_{ftir} yields: $h = 7.6$ m. This yields a new correction to be applied to the raw BSRN field sensor:

$$p = p_0 e^{\frac{-9.83 \cdot 7.6}{287 \cdot (T + 273.15)}} \tag{A.11}$$

A.5. Stability of the Ny-Ålesund FTS

The instrumental line shape (ILS) describes the shape of an absorption line as measured by the instrument. In an ideal instrument this would be equal to actual, physical, line shape produced by the molecules in the atmosphere. A number of mechanisms can disturb the natural line shape of absorption lines, most notably the finite length and discrete sampling of the interferogram or misalignment of the instrument.

The ILS can be deduced from comparison of a measured absorption line to a theoretically expected line. In this case, the expected line has to be known, which is achieved by measuring a gas cell with a known abundance of a target gas, typically with distinct narrow lines at low pressure, e.g. HCl or HBr.

From the cell absorption measurement, the modulation efficiency and phase error of the instrument are retrieved and used as an indicator for the alignment quality of the instrument. The standard retrieval code used within the TCCON and NDACC-IRWG is LINEFIT [Hase et al., 1999].

Figure A.4 shows phase error and modulation efficiency as a function of the optical path difference (OPD). A phase error of smaller than ±0.04 rad and a modulation efficiency of ±2 % of 1.0 up to a maximum optical path difference of 180 cm can be considered to be a well aligned instrument, especially for low resolution measurements like the ones performed for the lunar absorption spectra.

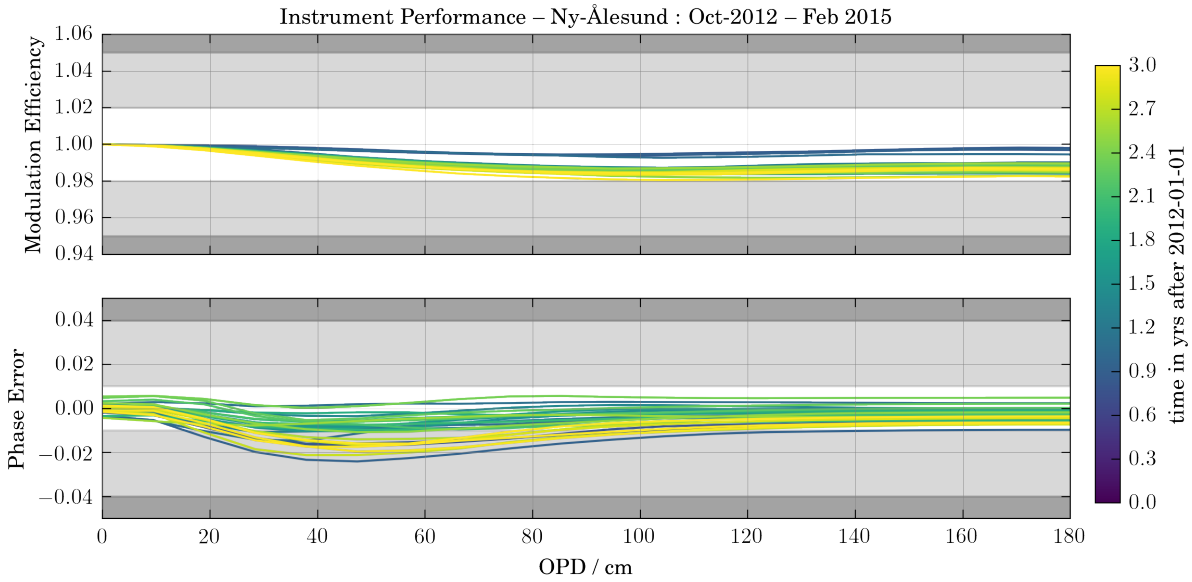

Figure A.4.: Modulation efficiency and phase error from LINEFIT retrievals as an indicator for instrument stability of the Ny-Ålesund FTS from 2012 to 2015.

A.6. Horizon line calculation from Svalbard DEM

The terrain height (in degrees) as viewed on the horizon from a specific location and height can be calculated if height and distance information for the surrounding terrain is available. The angle at which any point around the observer is viewed can then be calculated using the arctangent of the ratio between distance and height. From the resulting image the maximum values are taken in a set of directions around the observer. The resulting terrain height can be verified by a panorama picture scaled and shifted to the correct viewing angles, which is shown in Fig. A.5.

The terrain height data used for this analysis was provided by the digital elevation model (DEM) of the Norwegian Polar Institute. The resulting horizon line, as seen from the solar tracker of the Ny-Ålesund FTS can then be used to calculate accurate visibility prediction for solar and lunar measurements.

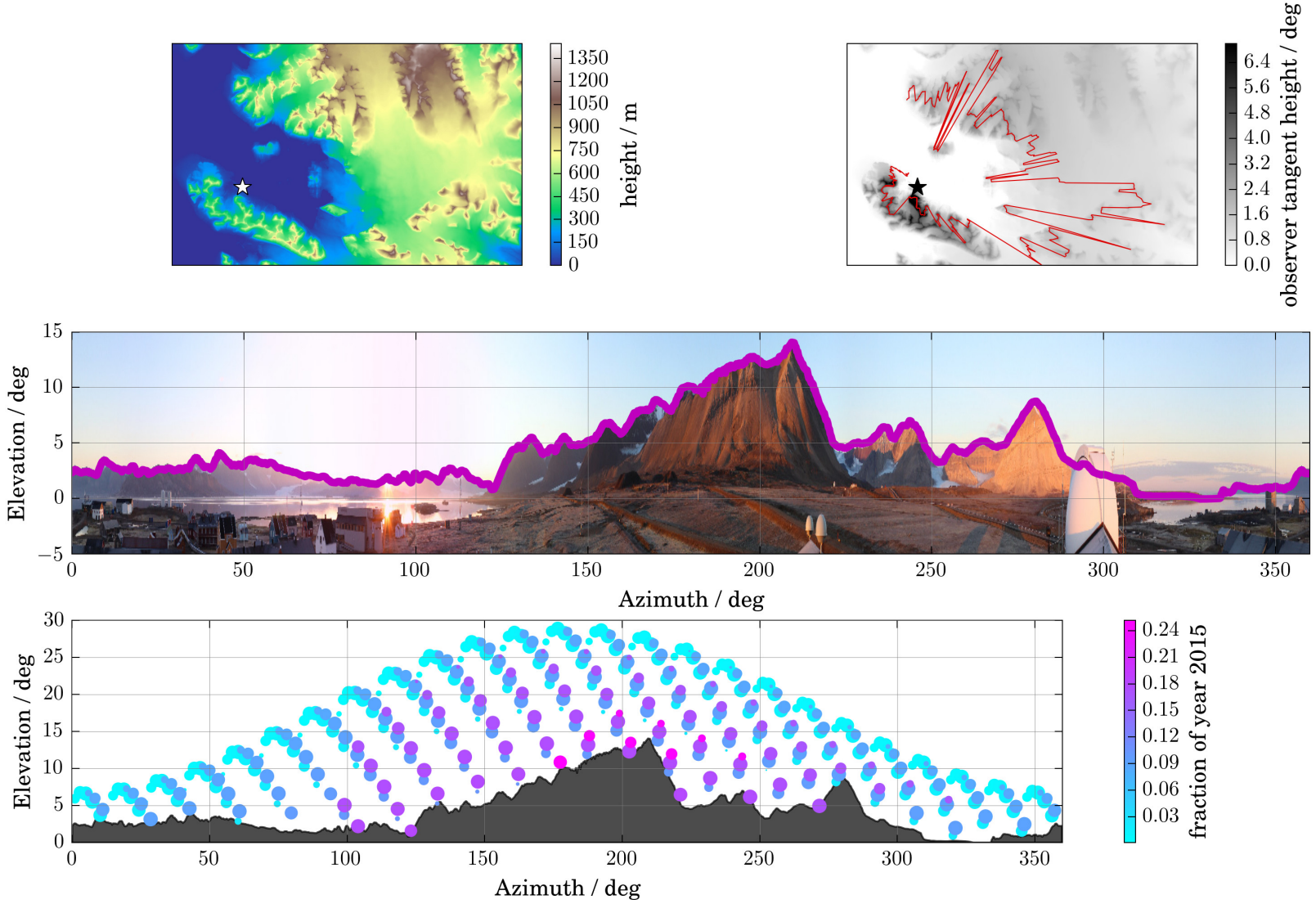

Figure A.5.: **Top left:** Svalbard DEM provided by Norwegian Polar Institute. The white asterisk marks the location of the AWIPEV observatory in Ny-Ålesund. **Top right:** The tangent heights as viewed from the observatory (asterisk). **Centre:** The calculated terrain height around the observatory and a panoramic picture (taken 2013-09-13 06:10 UTC). **Bottom:** Hourly lunar positions in spring 2015, the colour index shows the time of year and size indicates the lunar phase.

Bibliography

Arctic Monitoring and Assessment Programme AMAP. AMAP Assessment 2015: Methane as an Arctic Climate Forcer. http://www.amap.no/documents/doc/amap-assessment-2015-methane-as-an-arctic-climate-forcer/1285, 2015.

S. Barthlott, M. Schneider, F. Hase, A. Wiegele, E. Christner, Y. González, T. Blumenstock, S. Dohe, O. E. García, E. Sepúlveda, K. Strong, J. Mendonca, D. Weaver, M. Palm, N. M. Deutscher, T. Warneke, J. Notholt, B. Lejeune, E. Mahieu, N. Jones, D. W. T. Griffith, V. A. Velazco, D. Smale, J. Robinson, R. Kivi, P. Heikkinen, and U. Raffalski. Using XCO_2 retrievals for assessing the long-term consistency of NDACC/FTIR data sets. *Atmospheric Measurement Techniques*, 8(3):1555–1573, 2015. doi: 10.5194/amt-8-1555-2015. URL https://www.atmos-meas-tech.net/8/1555/2015/.

P. Bergamaschi, S. Houweling, A. Segers, M. Krol, C. Frankenberg, R. A. Scheepmaker, E. Dlugokencky, S. C. Wofsy, E. A. Kort, C. Sweeney, T. Schuck, C. Brenninkmeijer, H. Chen, V. Beck, and C. Gerbig. Atmospheric CH4 in the first decade of the 21st century: Inverse modeling analysis using SCIAMACHY satellite retrievals and NOAA surface measurements. *Journal of Geophysical Research: Atmospheres*, 118(13):7350–7369, 2013. ISSN 2169-8996. doi: 10.1002/jgrd.50480. URL http://dx.doi.org/10.1002/jgrd.50480.

H. Bovensmann, J. P. Burrows, M. Buchwitz, J. Frerick, S. Noël, V. V. Rozanov, K. V. Chance, and A. P. H. Goede. SCIAMACHY: Mission Objectives and Measurement Modes. *Journal of the Atmospheric Sciences*, 56(2):127–150, 1999. doi: 10.1175/1520-0469(1999)056⟨0127:SMOAMM⟩2.0.CO;2. URL https://doi.org/10.1175/1520-0469(1999)056<0127:SMOAMM>2.0.CO;2.

M. Buchwitz, M. Reuter, O. Schneising, H. Boesch, S. Guerlet, B. Dils, I. Aben, R. Armante, P. Bergamaschi, T. Blumenstock, H. Bovensmann, D. Brunner, B. Buchmann, J.P. Burrows, A. Butz, A. Chédin, F. Chevallier, C.D. Crevoisier, N.M. Deutscher, C. Frankenberg, F. Hase, O.P. Hasekamp, J. Heymann, T. Kaminski, A. Laeng, G. Lichtenberg, M. De Mazière, S. Noël, J. Notholt, J. Orphal, C. Popp, R. Parker, M. Scholze, R. Sussmann, G.P. Stiller, T. Warneke, C. Zehner, A. Bril, D. Crisp, D.W.T. Griffith, A. Kuze, C. O'Dell, S. Oshchepkov, V. Sherlock, H. Suto, P. Wennberg, D. Wunch, T. Yokota, and Y. Yoshida. The Greenhouse Gas Climate Change Initiative (GHG-CCI): Comparison and quality assessment of near-surface-sensitive satellite-derived {CO2} and {CH4} global data sets. *Remote Sensing of Environment*, (0):

–, 2013. ISSN 0034-4257. doi: http://dx.doi.org/10.1016/j.rse.2013.04.024. URL http://www.sciencedirect.com/science/article/pii/S0034425713003520.

J.P. Burrows, E. Hölzle, A.P.H. Goede, H. Visser, and W. Fricke. SCIAMACHY—scanning imaging absorption spectrometer for atmospheric chartography. *Acta Astronautica*, 35(7):445 – 451, 1995. ISSN 0094-5765. doi: https://doi.org/10.1016/0094-5765(94)00278-T. URL http://www.sciencedirect.com/science/article/pii/009457659400278T. Earth Observation.

M. Buschmann, N.M. Deutscher, M. Palm, T. Warneke, T. Weinzierl, and J. Notholt. Near-Infrared Lunar Absorption Spectroscopy for the Retrieval of Column Averaged CO2 and CH4. In G. Lohmann, H. Meggers, V. Unnithan, D. Wolf-Gladrow, J. Notholt, and A. Bracher, editors, *Towards an Interdisciplinary Approach in Earth System Science*, Springer Earth System Sciences, pages 85–90. Springer International Publishing, 2015. ISBN 978-3-319-13864-0. doi: 10.1007/978-3-319-13865-7_10. URL http://dx.doi.org/10.1007/978-3-319-13865-7_10.

M. Buschmann, N. M. Deutscher, V. Sherlock, M. Palm, T. Warneke, and J. Notholt. Retrieval of xCO_2 from ground-based mid-infrared (NDACC) solar absorption spectra and comparison to TCCON. *Atmospheric Measurement Techniques*, 9(2):577–585, 2016. doi: 10.5194/amt-9-577-2016. URL http://www.atmos-meas-tech.net/9/577/2016/.

M. Buschmann, N. M. Deutscher, M. Palm, T. Warneke, C. Weinzierl, and J. Notholt. The arctic seasonal cycle of total column CO_2 and CH_4 from ground-based solar and lunar FTIR absorption spectrometry. *Atmospheric Measurement Techniques*, 10(7):2397–2411, 2017a. doi: 10.5194/amt-10-2397-2017. URL https://www.atmos-meas-tech.net/10/2397/2017/.

M. Buschmann, N.M. Deutscher, M. Palm, T. Warneke, T. Weinzierl, and J. Notholt. Column averaged dry-air mole fractions of CO_2 and CH_4 at Ny-Ålesund from 2012 to 2016, 2017b. URL https://doi.org/10.1594/PANGAEA.872007.

T. Butz. *Fouriertransformation für Fußgänger*. Vieweg+Teubner Verlag, 2012. doi: 10.1007/978-3-8348-8295-0.

CarbonTracker. CT2013 results provided by NOAA ESRL, Boulder, Colorado, USA. http://carbontracker.noaa.gov.

F. Chevallier, N. M. Deutscher, T. J. Conway, P. Ciais, L. Ciattaglia, S. Dohe, M. Fröhlich, A. J. Gomez-Pelaez, D. Griffith, F. Hase, L. Haszpra, P. Krummel, E. Kyrö, C. Labuschagne, R. Langenfelds, T. Machida, F. Maignan, H. Matsueda, I. Morino, J. Notholt, M. Ramonet, Y. Sawa, M. Schmidt, V. Sherlock, P. Steele, K. Strong, R. Sussmann, P. Wennberg, S. Wofsy, D. Worthy, D. Wunch, and M. Zimnoch. Global CO2fluxes inferred from surface air-sample measurements and from TCCON retrievals of the CO2 total column. *Geophysical Research Letters*, 38(24):n/a–n/a,

2011. ISSN 1944-8007. doi: 10.1029/2011GL049899. URL http://dx.doi.org/10.1029/2011GL049899. L24810.

P. Ciais, C. Sabine, G. Bala, L. Bopp, V. Brovkin, J. Canadell, A. Chhabra, R. DeFries, J. Galloway, M. Heimann, C. Jones, C. Le Quéré, R. B. Myneni, S. Piao, and P. Thornton. *Climate Change 2013: The Physical Science Basis. Contribution of Working Group I to the Fifth Assessment Report of the Intergovernmental Panel on Climate Change*. Cambridge University Press, 2013.

B.J. Connor, H. Boesch, G. Toon, B. Sen, C. Miller, and D. Crisp. Orbiting Carbon Observatory: Inverse method and prospective error analysis. *Journal of Geophysical Research: Atmospheres*, 113(D5), 2008. ISSN 2156-2202. doi: 10.1029/2006JD008336. URL http://dx.doi.org/10.1029/2006JD008336. D05305.

D. Crisp, R.M Atlas, F.-M Breon, L.R Brown, J.P Burrows, P Ciais, B.J Connor, S.C Doney, I.Y Fung, D.J Jacob, C.E Miller, D O'Brien, S Pawson, J.T Randerson, P Rayner, R.J Salawitch, S.P Sander, B Sen, G.L Stephens, P.P Tans, G.C Toon, P.O Wennberg, S.C Wofsy, Y.L Yung, Z Kuang, B Chudasama, G Sprague, B Weiss, R Pollock, D Kenyon, and S Schroll. The Orbiting Carbon Observatory (OCO) mission. *Advances in Space Research*, 34(4):700 – 709, 2004. ISSN 0273-1177. doi: https://doi.org/10.1016/j.asr.2003.08.062. URL http://www.sciencedirect.com/science/article/pii/S0273117704003539. Trace Constituents in the Troposphere and Lower Stratosphere.

E. Damm, B. Rudels, U. Schauer, S. Mau, and G. Dieckmann. Methane excess in Arctic surface water-triggered by sea ice formation and melting. *Scientific reports*, 5:16179, 2015.

S. P. Davis, M. C. Abrams, and J. W. Brault. *Fourier Transform Spectrometry*. Academic Press, 2001.

W. Demtröder. *Laserspektroskopie 1 - Grundlagen*, volume 6. Springer, 2011. ISBN 978-3-642-21305-2. doi: 10.1007/978-3-642-21306-9.

N. M. Deutscher, D. W. T. Griffith, G. W. Bryant, P. O. Wennberg, G. C. Toon, R. A. Washenfelder, G. Keppel-Aleks, D. Wunch, Y. Yavin, N. T. Allen, J.-F. Blavier, R. Jiménez, B. C. Daube, A. V. Bright, D. M. Matross, S. C. Wofsy, and S. Park. Total column CO_2 measurements at Darwin, Australia - site description and calibration against in situ aircraft profiles. *Atmospheric Measurement Techniques*, 3(4):947–958, 2010. doi: 10.5194/amt-3-947-2010. URL http://www.atmos-meas-tech.net/3/947/2010/.

B. Dils, M. Buchwitz, M. Reuter, O. Schneising, H. Boesch, R. Parker, S. Guerlet, I. Aben, T. Blumenstock, J. P. Burrows, A. Butz, N. M. Deutscher, C. Frankenberg, F. Hase, O. P. Hasekamp, J. Heymann, M. De Mazière, J. Notholt, R. Sussmann, T. Warneke,

D. Griffith, V. Sherlock, and D. Wunch. The Greenhouse Gas Climate Change Initiative (GHG-CCI): comparative validation of GHG-CCI SCIAMACHY/ENVISAT and TANSO-FTS/GOSAT CO_2 and CH_4 retrieval algorithm products with measurements from the TCCON. *Atmospheric Measurement Techniques*, 7(6):1723–1744, 2014. doi: 10.5194/amt-7-1723-2014. URL `https://www.atmos-meas-tech.net/7/1723/2014/`.

E. J. Dlugokencky, L. Bruhwiler, J. W. C. White, L. K. Emmons, P. C. Novelli, S. A. Montzka, K. A. Masarie, P. M. Lang, A. M. Crotwell, J. B. Miller, and L. V. Gatti. Observational constraints on recent increases in the atmospheric CH4 burden. *Geophysical Research Letters*, 36(18):n/a–n/a, 2009. ISSN 1944-8007. doi: 10.1029/2009GL039780. URL `http://dx.doi.org/10.1029/2009GL039780`. L18803.

E. J. Dlugokencky, P. M. Lang, K. A. Masarie, A. M. Crotwell, and M. J. Crotwell. Atmospheric Carbon Dioxide Dry Air Mole Fractions from the NOAA ESRL Carbon Cycle Cooperative Global Air Sampling Network, 1968-2013, Version: 2014-06-27. `ftp://aftp.cmdl.noaa.gov/data/trace_gases/co2/flask/surface/`, 2014.

E.J. Dlugokencky, E.G. Nisbet, R. Fisher, and D. Lowry. Global atmospheric methane: budget, changes and dangers. *Philosophical Transactions of the Royal Society of London A: Mathematical, Physical and Engineering Sciences*, 369(1943):2058–2072, 2011. ISSN 1364-503X. doi: 10.1098/rsta.2010.0341. URL `http://rsta.royalsocietypublishing.org/content/369/1943/2058`.

D. Fu, T. J. Pongetti, J.-F. L. Blavier, T. J. Crawford, K. S. Manatt, G. C. Toon, K. W. Wong, and S. P. Sander. Near-infrared remote sensing of Los Angeles trace gas distributions from a mountaintop site. *Atmospheric Measurement Techniques*, 7(3):713–729, 2014. doi: 10.5194/amt-7-713-2014. URL `http://www.atmos-meas-tech.net/7/713/2014/`.

M. C. Geibel, J. Messerschmidt, C. Gerbig, T. Blumenstock, H. Chen, F. Hase, O. Kolle, J. V. Lavrič, J. Notholt, M. Palm, M. Rettinger, M. Schmidt, R. Sussmann, T. Warneke, and D. G. Feist. Calibration of column-averaged CH_4 over European TCCON FTS sites with airborne in-situ measurements. *Atmospheric Chemistry and Physics*, 12(18):8763–8775, 2012. doi: 10.5194/acp-12-8763-2012. URL `https://www.atmos-chem-phys.net/12/8763/2012/`.

M. Gisi, F. Hase, S. Dohe, T. Blumenstock, A. Simon, and A. Keens. XCO_2-measurements with a tabletop FTS using solar absorption spectroscopy. *Atmospheric Measurement Techniques*, 5(11):2969–2980, 2012. doi: 10.5194/amt-5-2969-2012. URL `http://www.atmos-meas-tech.net/5/2969/2012/`.

A. Goldman, R.H. Tipping, Q. Ma, C.D. Boone, P.F. Bernath, P. Demoulin, F. Hase, M. Schneider, J.W. Hannigan, M.T. Coffey, and C.P. Rinsland. On the line parameters for the (1–0) infrared quadrupolar transitions of 14N2 . *Journal of Quantitative Spectroscopy and Radiative Transfer*, 103(1):168 – 174, 2007. ISSN 0022-4073.

doi: http://dx.doi.org/10.1016/j.jqsrt.2006.05.010. URL http://www.sciencedirect.com/science/article/pii/S0022407306001439.

F. Hase, T. Blumenstock, and C. Paton-Walsh. Analysis of the instrumental line shape of high-resolution Fourier transform IR spectrometers with gas cell measurements and new retrieval software. *Appl. Opt.*, 38(15):3417–3422, May 1999. doi: 10.1364/AO.38.003417. URL http://ao.osa.org/abstract.cfm?URI=ao-38-15-3417.

J. K. Hedelius, C. Viatte, D. Wunch, C. M. Roehl, G. C. Toon, J. Chen, T. Jones, S. C. Wofsy, J. E. Franklin, H. Parker, M. K. Dubey, and P. O. Wennberg. Assessment of errors and biases in retrievals of X_{CO_2}, X_{CH_4}, X_{CO}, and X_{N_2O} from a $0.5\,cm^{-1}$ resolution solar-viewing spectrometer. *Atmospheric Measurement Techniques*, 9(8):3527–3546, 2016. doi: 10.5194/amt-9-3527-2016. URL http://www.atmos-meas-tech.net/9/3527/2016/.

JenaCO2. C. Rödenbeck. Estimating CO2 sources and sinks from atmospheric mixing ratio measurements using a global inversion of atmospheric transport Technical Report 6, Max Planck Institute for Biogeochemistry. http://www.bgc-jena.mpg.de/CarboScope/, 2005.

A. Karion, C. Sweeney, P. Tans, and T. Newberger. AirCore: An Innovative Atmospheric Sampling System. *Journal of Atmospheric and Oceanic Technology*, 27(11):1839–1853, 2010. doi: 10.1175/2010JTECHA1448.1. URL https://doi.org/10.1175/2010JTECHA1448.1.

F. Kasten and A.T. Young. Revised optical air mass tables and approximation formula. *Appl. Opt.*, 28(22):4735–4738, Nov 1989. doi: 10.1364/AO.28.004735. URL http://ao.osa.org/abstract.cfm?URI=ao-28-22-4735.

H.H. Kieffer and T.C. Stone. The Spectral Irradiance of the Moon. *The Astronomical Journal*, 129(6):2887, 2005. URL http://stacks.iop.org/1538-3881/129/i=6/a=2887.

K. Kohnert, A. Serafimovich, S. Metzger, J. Hartmann, and T. Sachs. Strong geologic methane emissions from discontinuous terrestrial permafrost in the Mackenzie Delta, Canada. *Scientific Reports*, 7(1):5828, 2017. ISSN 2045-2322. doi: 10.1038/s41598-017-05783-2. URL https://doi.org/10.1038/s41598-017-05783-2.

S. Kulawik, D. Wunch, C. O'Dell, C. Frankenberg, M. Reuter, T. Oda, F. Chevallier, V. Sherlock, M. Buchwitz, G. Osterman, C. E. Miller, P. O. Wennberg, D. Griffith, I. Morino, M. K. Dubey, N. M. Deutscher, J. Notholt, F. Hase, T. Warneke, R. Sussmann, J. Robinson, K. Strong, M. Schneider, M. De Mazière, K. Shiomi, D. G. Feist, L. T. Iraci, and J. Wolf. Consistent evaluation of ACOS-GOSAT, BESD-SCIAMACHY, CarbonTracker, and MACC through comparisons to TCCON. *Atmospheric Measurement Techniques*, 9(2):683–709, 2016. doi: 10.5194/amt-9-683-2016. URL https://www.atmos-meas-tech.net/9/683/2016/.

A. Kuze, H. Suto, M. Nakajima, and T. Hamazaki. Thermal and near infrared sensor for carbon observation Fourier-transform spectrometer on the Greenhouse Gases Observing Satellite for greenhouse gases monitoring. *Appl. Opt.*, 48(35):6716–6733, Dec 2009. doi: 10.1364/AO.48.006716. URL `http://ao.osa.org/abstract.cfm?URI=ao-48-35-6716`.

C. Le Quéré, R. Moriarty, R. M. Andrew, J. G. Canadell, S. Sitch, J. I. Korsbakken, P. Friedlingstein, G. P. Peters, R. J. Andres, T. A. Boden, R. A. Houghton, J. I. House, R. F. Keeling, P. Tans, A. Arneth, D. C. E. Bakker, L. Barbero, L. Bopp, J. Chang, F. Chevallier, L. P. Chini, P. Ciais, M. Fader, R. A. Feely, T. Gkritzalis, I. Harris, J. Hauck, T. Ilyina, A. K. Jain, E. Kato, V. Kitidis, K. Klein Goldewijk, C. Koven, P. Landschützer, S. K. Lauvset, N. Lefèvre, A. Lenton, I. D. Lima, N. Metzl, F. Millero, D. R. Munro, A. Murata, J. E. M. S. Nabel, S. Nakaoka, Y. Nojiri, K. O'Brien, A. Olsen, T. Ono, F. F. Pérez, B. Pfeil, D. Pierrot, B. Poulter, G. Rehder, C. Rödenbeck, S. Saito, U. Schuster, J. Schwinger, R. Séférian, T. Steinhoff, B. D. Stocker, A. J. Sutton, T. Takahashi, B. Tilbrook, I. T. van der Laan-Luijkx, G. R. van der Werf, S. van Heuven, D. Vandemark, N. Viovy, A. Wiltshire, S. Zaehle, and N. Zeng. Global Carbon Budget 2015. *Earth System Science Data*, 7(2):349–396, 2015. doi: 10.5194/essd-7-349-2015. URL `https://www.earth-syst-sci-data.net/7/349/2015/`.

G. Matthews. Celestial body irradiance determination from an underfilled satellite radiometer: application to albedo and thermal emission measurements of the Moon using CERES. *Appl. Opt.*, 47(27):4981–4993, Sep 2008. doi: 10.1364/AO.47.004981. URL `http://ao.osa.org/abstract.cfm?URI=ao-47-27-4981`.

M. Maturilli, A. Herber, and G. König-Langlo. Surface radiation climatology for Ny-Ålesund, Svalbard (78.9° N), basic observations for trend detection. *Theoretical and Applied Climatology*, 120(1):331–339, 2015. ISSN 1434-4483. doi: 10.1007/s00704-014-1173-4. URL `http://dx.doi.org/10.1007/s00704-014-1173-4`.

A. David McGuire, Leif G. Anderson, Torben R. Christensen, Scott Dallimore, Laodong Guo, Daniel J. Hayes, Martin Heimann, Thomas D. Lorenson, Robie W. Macdonald, and Nigel Roulet. Sensitivity of the carbon cycle in the Arctic to climate change. *Ecological Monographs*, 79(4):523–555, 2009. ISSN 1557-7015. doi: 10.1890/08-2025.1. URL `http://dx.doi.org/10.1890/08-2025.1`.

H. Meggers, M. Buschmann, K. Grosfeld, and S. Klebe. The Educational Program of the Earth System Science Research School (ESSReS). In G. Lohmann, H. Meggers, V. Unnithan, D. Wolf-Gladrow, J. Notholt, and A. Bracher, editors, *Towards an Interdisciplinary Approach in Earth System Science*, Springer Earth System Sciences, pages 9–17. Springer International Publishing, 2015. ISBN 978-3-319-13864-0. doi: 10.1007/978-3-319-13865-7_2. URL `http://dx.doi.org/10.1007/978-3-319-13865-7_2`.

J. Mendonca, K. Strong, G.C. Toon, D. Wunch, K. Sung, N.M. Deutscher, D.W.T. Griffith, and J.E. Franklin. Improving atmospheric CO2 retrievals using line mixing

and speed-dependence when fitting high-resolution ground-based solar spectra. *Journal of Molecular Spectroscopy*, 323:15 – 27, 2016. ISSN 0022-2852. doi: http://dx.doi.org/10.1016/j.jms.2016.01.007. URL http://www.sciencedirect.com/science/article/pii/S002228521630008X. Atmospheric Spectroscopy.

J. Messerschmidt, M. C. Geibel, T. Blumenstock, H. Chen, N. M. Deutscher, A. Engel, D. G. Feist, C. Gerbig, M. Gisi, F. Hase, K. Katrynski, O. Kolle, J. V. Lavrič, J. Notholt, M. Palm, M. Ramonet, M. Rettinger, M. Schmidt, R. Sussmann, G. C. Toon, F. Truong, T. Warneke, P. O. Wennberg, D. Wunch, and I. Xueref-Remy. Calibration of TCCON column-averaged CO_2: the first aircraft campaign over European TCCON sites. *Atmospheric Chemistry and Physics*, 11(21):10765–10777, 2011. doi: 10.5194/acp-11-10765-2011. URL http://www.atmos-chem-phys.net/11/10765/2011/.

Norwegian Polar Institute. Map Data and Services. https://geodata.npolar.no/. (CC BY 4.0), Last Access: 2016-03-11.

J. Notholt and R. Lehmann. The moon as light source for atmospheric trace gas observations: measurement technique and analysis method. *Journal of Quantitative Spectroscopy and Radiative Transfer*, 76(3–4):435 – 445, 2003. ISSN 0022-4073. doi: http://dx.doi.org/10.1016/S0022-4073(02)00069-9. URL http://www.sciencedirect.com/science/article/pii/S0022407302000699.

J. Notholt and O. Schrems. Ground-based FTIR measurements of vertical column densities of several trace gases above Spitsbergen. *Geophysical Research Letters*, 21(13):1355–1358, 1994. ISSN 1944-8007. doi: 10.1029/93GL01786. URL http://dx.doi.org/10.1029/93GL01786.

J. Notholt, R. Neuber, O. Schrems, and T. V. Clarmann. Stratospheric trace gas concentrations in the Arctic polar night derived by FTIR-spectroscopy with the Moon as IR light source. *Geophysical Research Letters*, 20(19):2059–2062, 1993. ISSN 1944-8007. doi: 10.1029/93GL01971. URL http://dx.doi.org/10.1029/93GL01971.

J. Notholt, P. von der Gathen, and S. Peil. Heterogeneous conversion of HCl and ClONO2 during the Arctic winter 1992/1993 initiating ozone depletion. *Journal of Geophysical Research: Atmospheres*, 100(D6):11269–11274, 1995. ISSN 2156-2202. doi: 10.1029/95JD00850. URL http://dx.doi.org/10.1029/95JD00850.

J. Notholt, G. Toon, F. Stordal, S. Solberg, N. Schmidbauer, E. Becker, A. Meier, and B. Sen. Seasonal variations of atmospheric trace gases in the high Arctic at 79°N. *Journal of Geophysical Research: Atmospheres*, 102(D11):12855–12861, 1997. ISSN 2156-2202. doi: 10.1029/97JD00337. URL http://dx.doi.org/10.1029/97JD00337.

J. Notholt, C. Petri, T. Warneke, N. Deutscher, M. Buschmann, C. Weinzierl, R. Macatangay, and P. Grupe. TCCON data from Bremen, Germany, Release GGG2014R0, 2017a. URL https://doi.org/10.14291/tccon.ggg2014.bremen01.R0/1149275.

J. Notholt, O. Schrems, T. Warneke, N. Deutscher, C. Weinzierl, M. Palm, M. Buschmann, and AWIPEV Station Engineers. TCCON data from Ny-Ålesund, Spitzbergen, Norway, Release GGG2014R0, 2017b. URL `https://doi.org/10.14291/tccon.ggg2014.nyalesund01.R0/1149278`.

A. Ostler, R. Sussmann, P. K. Patra, S. Houweling, M. De Bruine, G. P. Stiller, F. J. Haenel, J. Plieninger, P. Bousquet, Y. Yin, M. Saunois, K. A. Walker, N. M. Deutscher, D. W. T. Griffith, T. Blumenstock, F. Hase, T. Warneke, Z. Wang, R. Kivi, and J. Robinson. Evaluation of column-averaged methane in models and TCCON with a focus on the stratosphere. *Atmospheric Measurement Techniques*, 9(9):4843–4859, 2016. doi: 10.5194/amt-9-4843-2016. URL `http://www.atmos-meas-tech.net/9/4843/2016/`.

W. Peters, A.R. Jacobson, C. Sweeney, A.E. Andrews, T.J. Conway, K. Masarie, J.B. Miller, L.M.P. Bruhwiler, G. Pétron, A.I. Hirsch, D.E.J. Worthy, G.R. van der Werf, J.T. Randerson, P.O. Wennberg, M.C. Krol, and P.P. Tans. An atmospheric perspective on North American carbon dioxide exchange: CarbonTracker. *Proceedings of the National Academy of Sciences*, 104(48):18925–18930, 2007. doi: 10.1073/pnas.0708986104. URL `http://www.pnas.org/content/104/48/18925.abstract`.

C. Petri, T. Warneke, N. Jones, T. Ridder, J. Messerschmidt, T. Weinzierl, M. Geibel, and J. Notholt. Remote sensing of CO_2 and CH_4 using solar absorption spectrometry with a low resolution spectrometer. *Atmospheric Measurement Techniques*, 5(7):1627–1635, 2012. doi: 10.5194/amt-5-1627-2012. URL `http://www.atmos-meas-tech.net/5/1627/2012/`.

PyEphem. obtainable from `http://rhodesmill.org/pyephem/`, 2015. GNU Library or Lesser General Public License (LGPL).

C.D. Rodgers. *Inverse methods for atmospheric sounding: theory and practice*, volume 2. World scientific, 2000.

C.D. Rodgers and B.J. Connor. Intercomparison of remote sounding instruments. *Journal of Geophysical Research: Atmospheres*, 108(D3):n/a–n/a, 2003. ISSN 2156-2202. doi: 10.1029/2002JD002299. URL `http://dx.doi.org/10.1029/2002JD002299`.

W Roedel and T Wagner. *Physik unserer Umwelt: Die Atmosphäre*. Springer Berlin Heidelberg, Berlin, Heidelberg, 2011.

L.S. Rothman and L.D.G. Young. Infrared energy levels and intensities of carbon dioxide—II. *Journal of Quantitative Spectroscopy and Radiative Transfer*, 25(6):505 – 524, 1981. ISSN 0022-4073. doi: http://dx.doi.org/10.1016/0022-4073(81)90026-1. URL `http://www.sciencedirect.com/science/article/pii/0022407381900261`.

L.S. Rothman, D. Jacquemart, A. Barbe, D.C. Benner, M. Birk, L.R. Brown, M.R. Carleer, C. Chackerian Jr, K. Chance, L.H. Coudert, et al. The HITRAN 2004 molecular

spectroscopic database. *Journal of Quantitative Spectroscopy and Radiative Transfer*, 96(2):139–204, 2005.

L.S. Rothman, I.E. Gordon, A. Barbe, D.C. Benner, P.F. Bernath, M. Birk, V. Boudon, L.R. Brown, A. Campargue, J.-P. Champion, et al. The HITRAN 2008 molecular spectroscopic database. *Journal of Quantitative Spectroscopy and Radiative Transfer*, 110(9):533–572, 2009.

C. Rödenbeck. Estimating CO2 sources and sinks from atmospheric mixing ratio measurements using a global inversion of atmospheric transport, 2005.

H. Sahling, M. Römer, T. Pape, B. Bergès, C. dos Santos Fereirra, J. Boelmann, P. Geprägs, M. Tomczyk, N. Nowald, W. Dimmler, L. Schroedter, M. Glockzin, and G. Bohrmann. Gas emissions at the continental margin west of Svalbard: mapping, sampling, and quantification. *Biogeosciences*, 11(21):6029–6046, 2014. doi: 10.5194/bg-11-6029-2014. URL `http://www.biogeosciences.net/11/6029/2014/`.

M. Saunois, P. Bousquet, B. Poulter, A. Peregon, P. Ciais, J. G. Canadell, E. J. Dlugokencky, G. Etiope, D. Bastviken, S. Houweling, G. Janssens-Maenhout, F. N. Tubiello, S. Castaldi, R. B. Jackson, M. Alexe, V. K. Arora, D. J. Beerling, P. Bergamaschi, D. R. Blake, G. Brailsford, V. Brovkin, L. Bruhwiler, C. Crevoisier, P. Crill, K. Covey, C. Curry, C. Frankenberg, N. Gedney, L. Höglund-Isaksson, M. Ishizawa, A. Ito, F. Joos, H.-S. Kim, T. Kleinen, P. Krummel, J.-F. Lamarque, R. Langenfelds, R. Locatelli, T. Machida, S. Maksyutov, K. C. McDonald, J. Marshall, J. R. Melton, I. Morino, V. Naik, S. O'Doherty, F.-J. W. Parmentier, P. K. Patra, C. Peng, S. Peng, G. P. Peters, I. Pison, C. Prigent, R. Prinn, M. Ramonet, W. J. Riley, M. Saito, M. Santini, R. Schroeder, I. J. Simpson, R. Spahni, P. Steele, A. Takizawa, B. F. Thornton, H. Tian, Y. Tohjima, N. Viovy, A. Voulgarakis, M. van Weele, G. R. van der Werf, R. Weiss, C. Wiedinmyer, D. J. Wilton, A. Wiltshire, D. Worthy, D. Wunch, X. Xu, Y. Yoshida, B. Zhang, Z. Zhang, and Q. Zhu. The global methane budget 2000–2012. *Earth System Science Data*, 8(2):697–751, 2016. doi: 10.5194/essd-8-697-2016. URL `https://www.earth-syst-sci-data.net/8/697/2016/`.

M. Saunois, P. Bousquet, B. Poulter, A. Peregon, P. Ciais, J. G. Canadell, E. J. Dlugokencky, G. Etiope, D. Bastviken, S. Houweling, G. Janssens-Maenhout, F. N. Tubiello, S. Castaldi, R. B. Jackson, M. Alexe, V. K. Arora, D. J. Beerling, P. Bergamaschi, D. R. Blake, G. Brailsford, L. Bruhwiler, C. Crevoisier, P. Crill, K. Covey, C. Frankenberg, N. Gedney, L. Höglund-Isaksson, M. Ishizawa, A. Ito, F. Joos, H.-S. Kim, T. Kleinen, P. Krummel, J.-F. Lamarque, R. Langenfelds, R. Locatelli, T. Machida, S. Maksyutov, J. R. Melton, I. Morino, V. Naik, S. O'Doherty, F.-J. W. Parmentier, P. K. Patra, C. Peng, S. Peng, G. P. Peters, I. Pison, R. Prinn, M. Ramonet, W. J. Riley, M. Saito, M. Santini, R. Schroeder, I. J. Simpson, R. Spahni, A. Takizawa, B. F. Thornton, H. Tian, Y. Tohjima, N. Viovy, A. Voulgarakis, R. Weiss, D. J. Wilton, A. Wiltshire, D. Worthy, D. Wunch, X. Xu, Y. Yoshida, B. Zhang, Z. Zhang, and Q. Zhu.

Variability and quasi-decadal changes in the methane budget over the period 2000–2012. *Atmospheric Chemistry and Physics*, 17(18):11135–11161, 2017. doi: 10.5194/acp-17-11135-2017. URL `https://www.atmos-chem-phys.net/17/11135/2017/`.

Version 0.13.3 Stellarium. Virtual Planetarium. obtainable from `http://stellarium.org`, 2015. GNU GPL version 2 or later.

R. Sussmann, A. Ostler, F. Forster, M. Rettinger, N. M. Deutscher, D. W. T. Griffith, J. W. Hannigan, N. Jones, and P. K. Patra. First intercalibration of column-averaged methane from the Total Carbon Column Observing Network and the Network for the Detection of Atmospheric Composition Change. *Atmospheric Measurement Techniques*, 6(2):397–418, 2013. doi: 10.5194/amt-6-397-2013. URL `http://www.atmos-meas-tech.net/6/397/2013/`.

Teledyne Judson Datasheet. Indium gallium arsenide detectors - datasheet. http://www.teledynejudson.com/prods/Documents/InGaAs_shortform_Sept2003.pdf, 2003. Accessed on 2017-03-23.

P. W. Thorne, F. Madonna, J. Schulz, T. Oakley, B. Ingleby, M. Rosoldi, E. Tramutola, A. Arola, M. Buschmann, A. C. Mikalsen, R. Davy, C. Voces, K. Kreher, M. De Maziere, and G. Pappalardo. Making better sense of the mosaic of environmental measurement networks: a system-of-systems approach and quantitative assessment. *Geoscientific Instrumentation, Methods and Data Systems*, 6(2):453–472, 2017. doi: 10.5194/gi-6-453-2017. URL `https://www.geosci-instrum-method-data-syst.net/6/453/2017/`.

CT2015. CARBONTRACKER 2015 results provided by NOAA ESRL, Boulder, Colorado, USA. http://carbontracker.noaa.gov, 2016.

MACCCH4. MACC CH4 v10 reanalysis provided by the Copernicus monitoring system. http://www.gmes-atmosphere.eu/, 2016.

MACCCO2. MACC CO2 v14r2 reanalysis provided by the Copernicus monitoring system. http://www.gmes-atmosphere.eu/, 2016.

NCEPNCAR. NCEP/NCAR reanalysis data provided by the NOAA/OAR/ESRL PSD, Boulder, Colorado, USA. http://www.esrl.noaa.gov/psd/, 2016.

L. Wallace and W. Livingston. Spectroscopic observations of atmospheric trace gases over Kitt Peak: 1. Carbon dioxide and methane from 1979 to 1985. *Journal of Geophysical Research: Atmospheres*, 95(D7):9823–9827, 1990. ISSN 2156-2202. doi: 10.1029/JD095iD07p09823. URL `http://dx.doi.org/10.1029/JD095iD07p09823`.

T. Warneke, Z. Yang, S. Olsen, S. Körner, J. Notholt, G. C. Toon, V. Velazco, A. Schulz, and O. Schrems. Seasonal and latitudinal variations of column averaged volume-mixing ratios of atmospheric CO2. *Geophysical Research Letters*, 32(3), 2005.

ISSN 1944-8007. doi: 10.1029/2004GL021597. URL http://dx.doi.org/10.1029/2004GL021597. L03808.

R. A. Washenfelder, G. C. Toon, J.-F. Blavier, Z. Yang, N. T. Allen, P. O. Wennberg, S. A. Vay, D. M. Matross, and B. C. Daube. Carbon dioxide column abundances at the Wisconsin Tall Tower site. *Journal of Geophysical Research: Atmospheres*, 111(D22), 2006. ISSN 2156-2202. doi: 10.1029/2006JD007154. URL http://dx.doi.org/10.1029/2006JD007154. D22305.

K. W. Wong, D. Fu, T. J. Pongetti, S. Newman, E. A. Kort, R. Duren, Y.-K. Hsu, C. E. Miller, Y. L. Yung, and S. P. Sander. Mapping CH_4 : CO_2 ratios in Los Angeles with CLARS-FTS from Mount Wilson, California. *Atmospheric Chemistry and Physics*, 15(1):241–252, 2015. doi: 10.5194/acp-15-241-2015. URL http://www.atmos-chem-phys.net/15/241/2015/.

S. W. Wood, R. L. Batchelor, A. Goldman, C. P. Rinsland, B. J. Connor, F. J. Murcray, T. M. Stephen, and D. N. Heuff. Ground-based nitric acid measurements at Arrival Heights, Antarctica, using solar and lunar Fourier transform infrared observations. *Journal of Geophysical Research: Atmospheres*, 109(D18), 2004. ISSN 2156-2202. doi: 10.1029/2004JD004665. URL http://dx.doi.org/10.1029/2004JD004665. D18307.

D. Wunch, G. C. Toon, P. O. Wennberg, S. C. Wofsy, B. B. Stephens, M. L. Fischer, O. Uchino, J. B. Abshire, P. Bernath, S. C. Biraud, J.-F. L. Blavier, C. Boone, K. P. Bowman, E. V. Browell, T. Campos, B. J. Connor, B. C. Daube, N. M. Deutscher, M. Diao, J. W. Elkins, C. Gerbig, E. Gottlieb, D. W. T. Griffith, D. F. Hurst, R. Jiménez, G. Keppel-Aleks, E. A. Kort, R. Macatangay, T. Machida, H. Matsueda, F. Moore, I. Morino, S. Park, J. Robinson, C. M. Roehl, Y. Sawa, V. Sherlock, C. Sweeney, T. Tanaka, and M. A. Zondlo. Calibration of the Total Carbon Column Observing Network using aircraft profile data. *Atmospheric Measurement Techniques*, 3(5):1351–1362, 2010. doi: 10.5194/amt-3-1351-2010. URL http://www.atmos-meas-tech.net/3/1351/2010/.

D. Wunch, G.C. Toon, J.-F.L. Blavier, R.A. Washenfelder, J. Notholt, B.J. Connor, D.W.T. Griffith, V. Sherlock, and P.O. Wennberg. The Total Carbon Column Observing Network. *Philosophical Transactions of the Royal Society A: Mathematical, Physical and Engineering Sciences*, 369(1943):2087–2112, 2011a. doi: 10.1098/rsta.2010.0240. URL http://rsta.royalsocietypublishing.org/content/369/1943/2087.abstract.

D. Wunch, P. O. Wennberg, G. C. Toon, B. J. Connor, B. Fisher, G. B. Osterman, C. Frankenberg, L. Mandrake, C. O'Dell, P. Ahonen, S. C. Biraud, R. Castano, N. Cressie, D. Crisp, N. M. Deutscher, A. Eldering, M. L. Fisher, D. W. T. Griffith, M. Gunson, P. Heikkinen, G. Keppel-Aleks, E. Kyrö, R. Lindenmaier, R. Macatangay, J. Mendonca, J. Messerschmidt, C. E. Miller, I. Morino, J. Notholt, F. A. Oyafuso, M. Rettinger, J. Robinson, C. M. Roehl, R. J. Salawitch, V. Sherlock, K. Strong,

R. Sussmann, T. Tanaka, D. R. Thompson, O. Uchino, T. Warneke, and S. C. Wofsy. A method for evaluating bias in global measurements of CO_2 total columns from space. *Atmospheric Chemistry and Physics*, 11(23):12317–12337, 2011b. doi: 10.5194/acp-11-12317-2011. URL `http://www.atmos-chem-phys.net/11/12317/2011/`.

D. Wunch, G.C. Toon, V. Sherlock, N.M. Deutscher, C. Liu, D.G. Feist, and P.O. Wennberg. The Total Carbon Column Observing Network's GGG2014 Data Version. `http://tccon.ornl.gov/`, 2015. Last Access: 2017-06-01.

D. Wunch, G.C. Toon, V. Sherlock, N.M. Deutscher, C. Liu, D.G. Feist, and P.O. Wennberg. TCCON GGG2014 documentation. `http://tccon.ornl.gov/`, 2017a. Last Access: 2017-06-01.

D. Wunch, P. O. Wennberg, G. Osterman, B. Fisher, B. Naylor, C. M. Roehl, C. O'Dell, L. Mandrake, C. Viatte, M. Kiel, D. W. T. Griffith, N. M. Deutscher, V. A. Velazco, J. Notholt, T. Warneke, C. Petri, M. De Maziere, M. K. Sha, R. Sussmann, M. Rettinger, D. Pollard, J. Robinson, I. Morino, O. Uchino, F. Hase, T. Blumenstock, D. G. Feist, S. G. Arnold, K. Strong, J. Mendonca, R. Kivi, P. Heikkinen, L. Iraci, J. Podolske, P. W. Hillyard, S. Kawakami, M. K. Dubey, H. A. Parker, E. Sepulveda, O. E. García, Y. Te, P. Jeseck, M. R. Gunson, D. Crisp, and A. Eldering. Comparisons of the Orbiting Carbon Observatory-2 (OCO-2) X_{CO_2} measurements with TCCON. *Atmospheric Measurement Techniques*, 10(6):2209–2238, 2017b. doi: 10.5194/amt-10-2209-2017. URL `https://www.atmos-meas-tech.net/10/2209/2017/`.

Z. Yang, G.C. Toon, J.S. Margolis, and P.O. Wennberg. Atmospheric CO2 retrieved from ground-based near IR solar spectra. *Geophysical Research Letters*, 29(9):53–1–53–4, 2002. ISSN 1944-8007. doi: 10.1029/2001GL014537. URL `http://dx.doi.org/10.1029/2001GL014537`.

Y. Yoshida, N. Kikuchi, I. Morino, O. Uchino, S. Oshchepkov, A. Bril, T. Saeki, N. Schutgens, G. C. Toon, D. Wunch, C. M. Roehl, P. O. Wennberg, D. W. T. Griffith, N. M. Deutscher, T. Warneke, J. Notholt, J. Robinson, V. Sherlock, B. Connor, M. Rettinger, R. Sussmann, P. Ahonen, P. Heikkinen, E. Kyrö, J. Mendonca, K. Strong, F. Hase, S. Dohe, and T. Yokota. Improvement of the retrieval algorithm for GOSAT SWIR XCO_2 and XCH_4 and their validation using TCCON data. *Atmospheric Measurement Techniques*, 6(6):1533–1547, 2013. doi: 10.5194/amt-6-1533-2013. URL `https://www.atmos-meas-tech.net/6/1533/2013/`.

Glossary

AK	Averaging Kernel.
AWI	Alfred Wegener Institute, Helmholtz Centre for Polar and Marine Research.
AWIPEV	French-German Arctic Research Base AWI and IPEV.
BSRN	Baseline Surface Radiation Network.
DEM	Digital Elevation Model.
DMF	Dry-air Mole Fraction.
ESA	European Space Agency.
ESSReS	Earth System Science Research School.
FTS	Fourier-Transform Spectrometer.
GOSat	Greenhouse Gases Observing Satellite.
HITRAN	High-Resolution TRANsmission molecular absorption database.
ILS	Instrumental Line Shape.
IPCC	Intergovernmental Panel on Climate Change.
IPEV	Institut polaire français Paul-Émile Victor.
JAXA	Japan Aerospace Exploration Agency.
JPL	Jet Propulsion Laboratory.
MACC	Monitoring Atmospheric Composition and Climate of the European Copernicus Atmosphere Service.
MIR	Middle infrared.
NASA	National Aeronautics and Space Administration.
NCEP/NCAR	National Centers for Environmental Prediction / National Center for Atmospheric Research.
NDACC	Network for the Detection of Atmospheric Composition Change.
NDACC-IRWG	NDACC-InfraRed Working Group.
NEP	Noise-Equivalent Power.
NIR	Near infrared.
OCO-2	Orbiting Carbon Observatory-2.
OPD	Optical Path Difference.

S/N	Signal-to-Noise ratio.
SCIAMACHY	SCanning Imaging Absorption spectroMeter for Atmospheric CHartographY.
TCCON	Total Carbon Column Observing Network.
TE	Thermo-Electric.
TOA	Top Of Atmosphere.
WMO	World Meteorological Organisation.
ZPD	Zero Path Difference.